Title
Force Generation by Cytoplasmic Dynein and Development of PhotoGate Microscopy

Permalink
https://escholarship.org/uc/item/7pp0q58k

Author
Belyy, Vladislav

Publication Date
2016

Peer reviewed|Thesis/dissertation

FORCE GENERATION BY CYTOPLASMIC DYNEIN AND

DEVELOPMENT OF PHOTOGATE MICROSCOPY

By

Vladislav Belyy

A dissertation submitted in partial satisfaction of the

requirements for the degree of

Doctor of Philosophy

in

Biophysics

in the

Graduate Division

of the

University of California, Berkeley

Committee in charge:

Professor Ahmet Yildiz, Chair
Professor Carlos Bustamante
Professor Jeremy Thorner
Professor Andreas Martin

Spring 2016

ABSTRACT

Force Generation by Cytoplasmic Dynein and Development of PhotoGate Microscopy

by

Vladislav Belyy

Doctor of Philosophy in Biophysics

University of California, Berkeley

Professor Ahmet Yildiz, Chair

Cytoskeletal motors play key roles in the organization and division of eukaryotic cells. Although detailed mechanistic understanding has been achieved for motors in the myosin and kinesin families, the mechanochemical cycle of cytoplasmic dynein remained a subject of debate. Understanding the mechanism of dynein motility has been difficult due to its large size, unusual architecture, irregular stepping pattern, and complex regulation by a number of auxiliary proteins. In my doctoral work, I showed that the two heads of dynein utilize a load-sharing mechanism that allows them to work against hindering forces larger than the maximal force produced by a single head. Next, I demonstrated that the regulatory proteins dynactin and Bicaudal-D homolog 1 (BICD) dramatically increase the force production of human dynein and allow it to defeat a human kinesin-1 motor in a tug-of-war competition.

In addition, I developed the PhotoGate method for imaging single fluorescent molecules in the crowded environment of a living cell. This method eliminates the need for fluorophore photoactivation, enabling longer single-particle tracking times and direct measurement of stoichiometry of macromolecular complexes. This technique was used to measure ligand-induced dimerization of epidermal growth factor (EGF) receptors on the cell membrane at densities of >50 molecules per μm^2. It was also applied to monitor the arrivals and departures of single Adaptor Protein Phosphotyrosine Interaction PH domain and Leucine Zipper-containing-1 (APPL1) molecules at early endosomes. PhotoGate will be broadly applicable to the study of macromolecular complex formation in the densely packed conditions of the cytoplasm.

This dissertation is dedicated to Carolyn Berger-Ott, who will remain in the memories of her students from Walter Johnson High School as the incurably optimistic teacher of physics and mathematics with a true talent to inspire others. With her gentle humor, confident intelligence, a formidable ability to explain, and a kind heart, Mrs. Ott was as much a friend as she was a teacher.

ACKNOWLEDGEMENTS

My true introduction to science took place in the laboratory of Prof. Sergei Sukharev at the University of Maryland. He courageously allowed a freshman undergraduate student who knew very little biology or physics join his lab, then entrusted the student with a fragile and expensive electrophysiology rig and gave him the freedom to pursue ambitious ideas. The four years I spent in the Sukharev lab gave me the confidence and curiosity to pursue an academic career in biophysics. Joining the laboratory of Prof. Ahmet Yildiz at UC Berkeley provided a complementary experience. The lab was brand new and everything was exciting; instruments and protocols were not yet established, and every lab member was essentially pioneering a new research direction. With Ahmet's unwavering guidance and encouragement, I learned more diverse skills than I would have thought possible, carried three exciting projects to completion, and strengthened my resolve to pursue academic research.

I am grateful to my fantastic colleagues in the Yildiz Lab, both for thoughtful scientific discussions and for relaxing after-hours banter: Jigar Bandaria, Sinan Can, John Canty, Alex Chien, Yavuz Dagdas, Luke Ferro, Nathan Hendel, Peiwu Qin, Maya Segal, Sara Wichner, Mark Dewitt, Frank Cleary, Sheng-Min Shih, and Tunc Yilmaz. Finally, I thank the members of my Annual Thesis Guidance Committee, Profs. Carlos Bustamante, Andreas Martin and Jeremy Thorner for their time, guidance and constructive criticism.

Among the most exciting aspects of living in Berkeley was making great new friends: Mike Souza, Tim Wendorff, Kris Nyquist, Sara Wahlin, Cory Antonakos, Keenan Thomas, and many more. Whether it be skiing around Lake Tahoe, trying to tune the dual carburetors of an ancient British car, or hiking in Desolation Wilderness, friends were always there to remind me that science is not the only thing that matters.

My deepest thanks go out to my closest friend and loving wife, Alina Kelman. Her contagious optimism, love of adventure, and compassion for all living things continue to inspire me in all my pursuits. I also thank my parents, Evgueni Belyi and Inna Belaia, for stimulating and encouraging my curiosity from the youngest age, and my sister Vera Belaia for being the best sibling in the world – smart, funny, and always reminding me not to take myself too seriously. Finally, I would like to thank my cat Albie, who repeatedly attempted to introduce extra entropy into my manuscripts by waslking across the keyboard while I was typing.

TABLE OF CONTENTS

INTRODUCTION

A portion of the material presented in this chapter was published in the following review paper: Belyy, V. & Yildiz, A. Processive cytoskeletal motors studied with single-molecule fluorescence techniques. *FEBS Lett.* 1–6 (2014).

Cytoskeletal motors

The single-molecule approach

A eukaryotic cell depends on cytoskeletal molecular motors to actively maintain the spatial organization and material flux required for the cell's survival. These remarkable protein machines convert chemical energy into mechanical work as they walk along actin filaments and microtubules. Cytoskeletal motors are divided into three protein superfamilies: myosins, kinesins, and dyneins (**Figure 1**). The study of motors through traditional biochemical methods is complicated by the fact that many of the fundamental properties of their motility cannot be readily measured in bulk assays. One such property is the motor's velocity, which determines how rapidly it can deliver cargo to its destination. Other key properties are processivity, a measurement of how many successive steps a motor can take before dissociating from its track, and maximal force production, both of which are critically important for understanding how teams of motors work together to power long-distance transport while avoiding gridlock and overcrowding. For a more detailed understanding of the motor's mechanism, it is invaluable to know its stepping pattern - the manner in which the heads move with respect to one another as the motor walks down its track. These properties are all amenable to study with single-molecule fluorescence and optical trapping techniques.

Motors that function in muscle contraction (myosin II) and ciliary beating (inner and outer arm dyneins) work in large groups to generate force on macroscopic scales. While these motors can be studied collectively with filament gliding assays[1], individual motors need not be processive and their motility may not be immediately apparent on a single-molecule level. However, it was found that many other cytoskeletal motors transport cargos in small teams or alone[2,3], a function requiring the molecules to be able to take many successive steps without diffusing away from the track. In order to achieve processive motion, a molecular motor must remain tethered to the track throughout its entire mechanochemical cycle, a requirement that potentially explains why the majority of processive motors discovered to date possess two or more track binding sites.
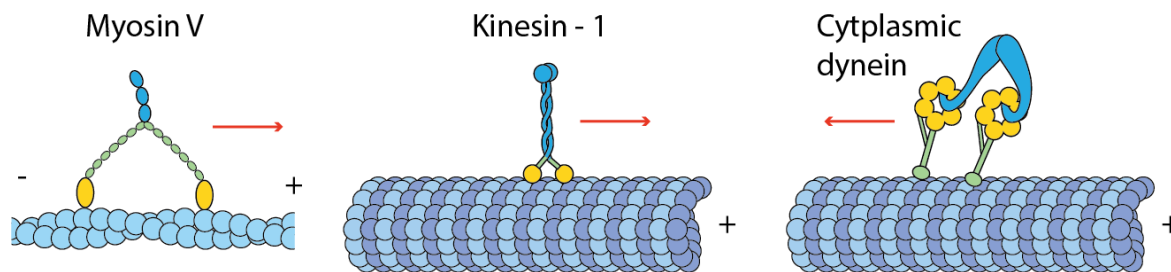
Figure 1. The three families of processive cytoskeletal motors. Myosin V (left) walks towards the plus end of actin filaments, kinesin-1 (center) walks towards the plus end of microtubules, and cytoplasmic dynein (right), walks towards the minus end of microtubules. Motor domains are shown in yellow, and cargo binding tail domains are shown in blue.

Motor stepping patterns

Single-molecule tracking methods provided sufficient spatiotemporal accuracy to detect individual steps taken by cytoskeletal motors. Using optical traps, it had previously been shown that myosin V's cargo binding domain moves on average in 37 nm steps[4,5], equivalent to the half helical pitch of the actin. To determine whether these steps resulted from an inchworm or hand-over-hand (HoH) mechanism, myosin V motors were fluorescently labeled on one head and tracked with 1 nm precision as they walked on surface-immobilized actin filaments[6]. Had myosin been an inchworm motor, one would expect to see the heads step in 37 nm increments just like the cargo-binding domain. However, in practice each molecule exhibited a distinctly bimodal step size distribution, moving in 74nm steps alternating with invisible "0 nm" steps[6]. The presence of the "0 nm" steps is revealed by the characteristic shape of the dwell time histogram, which changes from a single exponential decay into a convolution of two exponentials as the step of a single head consists of two consecutive events. Later, kinesin-1 and myosin VI were demonstrated to be HoH steppers in a similar manner[7–9], while more recent work suggested that the two modes of stepping are not necessarily mutually exclusive as myosin VI motors are able to switch between HoH and inchworm-like steps[10].

The finding that a motor such as kinesin walks in strictly alternating steps necessitates some form of "gating" mechanism between the two heads that would prevent the leading head to release from the track until the trailing head completes its step. Several theories have been proposed for motor protein gating. The tubulin binding gate model postulates that the stepping head cannot bind to the next site on the track until its partner head binds a new ATP molecule[11]. Tension gating proposes that mechanical

strain generated between the two heads plays a role in keeping the two heads out of phase. In this model, rear-head gated scenario suggests that the trailing head is mechanically pulled off the track by strain produced in the front head. The front head-gated scenario suggests that ATP binding to the front head is suppressed by rearward strain from the trailing head[12]. The importance of mechanical strain between the two heads was demonstrated by inserting flexible linkers of varying length between the heads and the dimerization domain. When examined in single-molecule fluorescence, these extended constructs exhibited reduced velocity and a highly variable stepping pattern, suggesting that the loss of intramolecular strain led to a substantial decrease in gating efficiency[13]. A later optical trapping study established that kinesin spends the majority of its time in a one head-bound state and the intramolecular strain makes the off-pathway two-head bound states more unfavorable, rather than triggering release in a two head-bound state[14]. Finally, it was recently demonstrated that it is the backward orientation of the neck linker, rather than the absolute magnitude of tension between the heads, that mediates the gating of the front head[15,16].

The stepping pattern of cytoplasmic dynein labeled with a single fluorophore was somewhat inconclusive about the way dynein walks along microtubules. Unlike kinesin, which takes regular 8 nm steps in a HoH fashion, dynein displays a large variability in step size, as well as frequent movement in sideways and backward directions[17]. To visualize how dynein's heads move with respect to one another, two groups simultaneously pursued the goal of labeling dynein's two heads with fluorophores of different color and obtaining simultaneous stepping traces for them. An important challenge in dual-color super-resolution tracking is overlaying the images from both channels with sub-pixel accuracy. This can be achieved, for example, by scanning a fiducial marker (such as a broad-spectrum fluorescent bead) in small increments across the field of view, localizing it with a 2D Gaussian fit in each channel, and using the resulting position pairs to generate a map between the two channels[18]. Provided that the fiducial markers fluoresce at the same wavelengths as the actual fluorophores used in the experiment, mapping can correct for optical aberrations, CCD pixel-to-pixel variation, and physical differences between the two imaging paths, resulting in an overall mapping accuracy of up to 1 nm[18–20]. In the two-color dynein experiments, while Qiu *et al.* used organic dyes and DeWitt *et al.* opted for the larger but more photostable quantum dots, both reached the same conclusion that cytoplasmic dynein displays a large variability in stepping pattern compared to myosin and kinesin[19,21]. Both the size and timing of a dynein head's step are only weakly affected by the position of the partner head. Dynein's case clearly illustrates that gating is not necessary for processive

motility and that long-range movement can be achieved by two mechanically linked heads, provided each spends the majority of its time bound to the track and only releases briefly to take the next step.

Regulation of motor activity

A cell employs regulatory mechanisms to control the attachment of motors to cargos, to modulate their velocity or force production depending on the specific task they're performing, or to prevent them from undergoing futile cycles of ATP hydrolysis when not engaged with the track[22]. Such mechanisms can be grouped into two general categories: autoinhibition and inhibition by regulatory proteins. Motility experiments on kinesin-1 mutants with the tail domain either truncated or made less flexible at a prominent hinge showed that both mutants moved 2-3 fold faster than wild-type kinesin and exhibited greatly enhanced processivity. This points towards an autoinhibition mechanism wherein kinesin's tail acts as a repressor of the motor domain in the absence of bound cargo[23]. Crystallographic work later showed that this inhibition occurs via a tail-mediated crosslinking of the two motor domains, preventing the separation of the two heads required for neck linker undocking[24]. Similar autoinhibitory mechanisms appear to be present in kinesin-2[25], kinesin-3[26], and myosin V[27–29] motors.

For cytoplasmic dynein, several distinct regulatory proteins were identified. Lis1 impacts dynein motility on a single-molecule level[30], effectively anchoring dynein to its track. Interestingly, this mechanism does not prevent futile cycles of ATP hydrolysis, suggesting that dynein may also have an autoinhibitory mechanism yet to be discovered. Lis1-based anchoring potentially configures dynein for low-speed, high-force cellular tasks such as anchoring spindle microtubules during mitosis. Another dynein regulator, She1 diffuses along microtubules until it encounters a walking dynein. She1 binds and pauses the motor, prolonging its attachment to the microtubule[31]. More recently, dynactin and a cargo adapter protein BICD were shown to dramatically activate the processive motility of human dynein[32,33].

In addition to cellular regulators, an increasing pool of specific small-molecule inhibitors is being develop to dissect the contributions of individual motor proteins to intracellular transport. For instance monastrol was used to target homotetrameric kinesin Eg5, which slides apart microtubules and contributes to the assembly of the mitotic spindle[34]. The effect of monastrol in Eg5 motility was tested using single molecule fluorescence assays. Eg5 is a processive plus end-directed motor that occasionally switches into diffusive mode. The addition of the drug monastrol significantly enriches the diffusive state while

effectively abolishing directional motion[35]. Similarly, ciliobrevin D specifically inhibits dynein motors *in vivo*[36]. Targeting specific motors may serve as alternatives to tubulin-targeting antimitotic agents used in cancer therapy, with potentially fewer side effects due to their highly specialized roles in mitosis[37].

Cargo transport by teams of motors

Intracellular cargoes such as lipid droplets, organelles, and endoplasmic reticulum vesicles are commonly transported by small teams of motors rather than individual proteins. Time-lapse observation of mitochondrial transport in axons and dendrites of cultured neurons exhibited diverse motility, ranging from slow unidirectional movement to rapid switching between bursts of fast retrograde and anterograde runs[38]. Similar bidirectional behavior was observed using a variety of techniques for phagosomes[39], endosomes[40], lipid droplets[41], neurofilaments[42], intraflagellar transport (IFT) trains[43], and other cargos. The cell may control the overall distribution of cargos in the cytoplasm by affecting either motor recruitment to cargos or the engagement of cargo-bound motors with the track[44]. Two commonly proposed and not mutually exclusive models for how bidirectional transport may be achieved and regulated are stochastic tug-of-war between competing teams of opposite-polarity motors bound to the same cargo[45] and regulated directional switching[41]. Such switching can be carried out through different pathways, such as inactivation/unbinding of motors of one polarity or specific inhibition of a particular class of motors.

An important challenge for understanding the mechanism of cargo transport is the difficulty of measuring the number of motors of each polarity that are attached to the cargo and engaged with the track at any given point in time. The total number of motors attached to a cargo can be measured by several methods, such as fluorescence bleaching counting assays or quantitative blotting[45]. However, not all of the cargo-bound motors may be active at a time. The number of actively engaged motors pulling the cargo was estimated to be relatively low (1-5 motors of each polarity) by in vivo and in vitro optical trapping assays, with an important underlying assumption that motor stall forces are additive at low copy numbers[40,45–48]. High-resolution imaging of reconstituted neuronal transport vesicles revealed that even at such small motor numbers vesicles moved bidirectionally and exhibited rapid direction switching similarly to their *in vivo* counterparts, just as predicted by the mechanical tug-of-war model[45]. On the other hand, IFT trains in *Chlamydomonas reinhardtii* were found to move in a clearly coordinated manner, with motors of only one polarity active at a time[49], illustrating that regulation of transport *in vivo* is not limited to tug-of-war. An artificial DNA

origami scaffold helps overcome the limitation of the motor number per cargo variability, by assembling well-defined groups of motors *in vitro*[50]. The presence of mechanical tug-of-war between multiple dyneins and kinesins were demonstrated by changing the relative numbers of the opposing motors on a scaffold. Cargoes with 2.5 times more kinesins than dyneins still moved in the retrograde direction despite dynein's lower stall force, suggesting that parameters other than stall force (such as tenacity of microtubule attachment) may be more relevant for a motor's tug-of-war performance.

Single-molecule fluorescence

The first direct confirmation of motor processivity was achieved by imaging individual kinesin molecules walking along microtubules[51], and was soon followed by similar observations on myosin[3] and dynein[17]. Single-motor motility assays are performed under total internal reflection fluorescence (TIRF)[52] illumination, in which the evanescent field of a laser beam reflected off the water/glass interface excites fluorescently tagged motors moving along surface-immobilized tracks. The intensity of the evanescent field falls off exponentially with distance from the coverslip, limiting the depth of the excitation region to a few hundred nanometers and greatly reducing background fluorescence from the bulk solution. Observing the motors directly in real time allows for measurement of a number of fundamental properties. Kinesin-1 was shown to travel on average 600 nm before dissociating from the track[51], demonstrating that a typical run consisted of ~100 successive 8nm steps[53]. Repeating the experiment with kinesin constructs lacking their dimerization domain showed that kinesin-1 requires both heads to remain processive. It has furthermore been shown that Unc104[54] and myosin VI[55] motors transition from diffusional to directional processive motion upon dimerization at high concentrations. The requirement for dimerization for processive motility was also demonstrated in yeast cytoplasmic dynein by designing monomers with chemically inducible dimerization domains [17].

Sub-diffraction imaging

Processive motors were found to generally require two head domains to remain motile, which led to the question of how they coordinate their motions to generate successive steps without simultaneously releasing from the track. One may picture the motor walking much like a human would, taking regular alternating steps of equal sizes with its two "feet". This mechanism, which is referred to as "hand over hand" (HoH), requires a large degree of coordination between the two heads, as each head takes a step

in the trailing position and remains firmly attached in the lead[56]. Another proposed possibility is that the "inchworm" model, wherein the full cycle consists of two nearly simultaneous steps by the heads and results in a translation of the motor without changing the relative orientation of the two heads[57]. Such a mechanism requires stricter coordination than HoH due to the added timing constraint between the steps of the trailing and leading head. The stochastic stepping model abolishes coordination altogether and allows the heads to move forward independently of their partner. In this case, spontaneous release from the track is prevented by the low probability of simultaneously finding both heads in the unbound state.

The spatiotemporal resolution required to distinguish between these possibilities and investigate the kinetics of stepping resulted in early adoption of sub-diffraction imaging techniques. The diffraction-limited image of a single fluorescent molecule (termed point spread function, or PSF) has a width of approximately $\lambda/(2 \text{ N.A.})$, where λ is the wavelength of light and N.A. is the numerical aperture of the objective lens. Using the highest N.A. (1.49 to 1.65) objectives available, the image of a point-like object emitting visible photons has a width of ~250 nm. This width is an order of magnitude larger than the step size of the motors (8-37 nm). Resolving the stepping pattern requires a significant improvement in resolution, which prompted the use of sub-diffraction fluorophore localization. While the width of a single fluorophore's image cannot be readily decreased beyond the fundamental limit, its peak position can be determined with high precision by collecting a sufficient number of photons (on the order of 20,000 photons for 1 nm localization accuracy)[58]. With the important limitation that individual molecules must be well-separated on the camera's detector, a 2-dimensional Gaussian fit can localize their positions to ~1 nm at sub-second frame rates using organic dyes[6,59].

Because the precision with which a fluorophore can be localized within a frame generally scales as the square root of the number of collected photons[59], the photostability of the probe is of paramount importance for the acquisition of high-resolution videos of walking molecules. The most critical parameter is the average total number of photons emitted by the fluorophore before it undergoes photobleaching. Photobleaching generally occurs when a fluorophore in an excited state chemically reacts with a singlet oxygen. This effect can be greatly reduced by removing oxygen from the system, using oxygen scavenging enzymes. Since oxygen enhances fluorescence by acting as an effective triplet state quencher, imaging buffers typically include a separate triplet state quencher to compensate for the absence of oxygen and prevent dye blinking[60]. As a result, efforts to increase fluorophore lifetimes have centered on triplet state quenchers and enzymatic systems for removal of free oxygen. Recent work showed that while thiol-containing

compounds such as β-mercaptoethanol and L-glutathione are efficient triplet state quenchers, they can cause slow blinking of cyanine dyes, a problem that can be overcome by using Trolox as a quencher instead[61]. To remove free oxygen, one commonly used system is the glucose oxidase/catalase enzyme pair[62]. More recently, an enzymatic system based on protocatechuate dioxygenase gained popularity because the byproduct of its reaction does not alter the pH of the buffer[63]. However, despite these improvements, photostability varies greatly between fluorophores[64] and the majority of fluorophores are not sufficiently stable for high-resolution tracking. Multi-frame localization with nanometer-scale precision has only been achieved to date using the best small organic probes (such as Cy3, Cy5, and TMR)[6,7,21] and quantum dots[10,17,65].

Optical trapping

A large portion of the data presented in this dissertation was collected on a state of the art optical trap microscope. Optical trapping has been invaluable in the study of biological polymers and molecular motors, enabling the first measurements of steps and forces produced by individual motor proteins. Several excellent reviews and guides have already been published on the subject[66–68]. To complement rather than paraphrase them, I will describe some of the practical thoughts and insights I developed after troubleshooting, designing, and building optical traps in the Yildiz lab.

Since trap designs vary significantly from lab to lab, it is important to briefly describe the layout of the two Yildiz Lab traps that my experience is derived from. Both use 1064 nm CW lasers as the source of the trapping beam, rely on a pair of acousto-optical deflectors (AODs) for precise beam steering, and utilize back-focal plane interferometry for position detection by imaging the trapping laser's beam onto a 200 kHz position sensitive detector. The trap in Birge Hall is used for surface-coupled assays and focuses a single trapping beam onto the image plane with a 1.49 N.A. oil-immersion objective. Fluorescence laser lines are available for TIRF imaging, and a separate 845 nm solid-state laser is reflected off the coverslip and projected onto a separate PSD for long-term focus stabilization. The Stanley Hall trap is reserved for dual-beam trapping experiments and creates both trapping beams via AOD time-sharing. The trapping beam is focused onto the image plane using a high-N.A. water-immersion objective and collected for detection with a second, identical objective. Time-sharing code runs on a field-programmable gate array (FPGA) to guarantee the precise timing required for artifact-free synchronization of the AODs and the PSD. Power control is achieved in

both traps by discarding the required percentage of the laser's output into a beam dump, set by a half-wave plate mounted on a motorized rotary mount.

The optical trap is typically viewed as one of the most advanced and sophisticated instruments in a single-molecule biophysics lab. This biased perception stems from the fact that each microscope effectively needs to be designed, built, and programmed in-house by an individual scientist, unless one of the few commercially available "off the shelf" solutions happens to precisely fit the particular requirements. The optical path of a typical trap is neither complicated nor particularly difficult to align using high-quality kinematic mounts. The only steps likely to pose a challenge are fiber-coupling the trapping laser and aligning the AODs. The former step can be avoided by using a fiber-coupled laser from the start, while the latter can be shortened by methodically scanning the beam across the deflectors in small increments rather than trying to find the optimal angle right away. The true difficulties of building a functional trap can be separated into two broad categories: noise elimination and software design.

Noise elimination

Precise measurement of nanometer-scale distances is often an absolute requirement for an optical trap. Therefore, identifying the smallest sources of noise and eliminating ones not inherent to the experiment becomes a key task for any researcher designing or troubleshooting the instrument. Before embarking on the noise hunt, it is critical to understand the properties and fundamental limitations of thermal (or Brownian) noise, which sets fixed bounds on the spatial and temporal resolution achievable in a trapping experiment[69–71]. Other, non-Brownian, sources of noise can generally be identified and either removed, minimized, or corrected for.

Generally, the easiest sources of noise to identify are those with a well-defined characteristic frequency. By immobilizing beads on the surface of a coverslip, focusing the trap on one of the beads, recording a position trace over several seconds, and taking the trace's Fourier transform, one can easily obtain a compound power spectrum of all the contributing non-Brownian noise sources. Single-frequency noise will appear as a sharp, distinct spike in this power spectrum. One real example of such noise in our trap came from a cooling fan built into a camera connected to the microscope body. Every time the fan turned on, we observed a clear spike at the fan's rotational frequency; the solution was to disable the fan and cool the camera with water. Another common source of single-frequency noise is "mains hum" or leakage of the 60 Hz AC current signal from the building's power supply into the trap's sensitive detection electronics. This leakage

can either occur directly, e.g. as a result of using a low-quality AC-to-DC converter to power the detector, or through an unexpected path (for instance, if ceiling lights are on in the room during recording, their light output will also oscillate at 60 Hz and trigger periodic currents in the detector). The two examples above can be solved by using higher-quality AC-to-DC converters and performing the experiments with room lights turned off, respectively.

Unfortunately, many sources of noise and drift exhibit complex power spectra and cannot be so easily traced to a specific source. Examples include, but are certainly not limited to, stage drift, laser pointing instabilities, laser power instabilities, vibrations in the microscope body, electrical leaks and faults in the detection electronics wiring, ground loops, temperature drift due to differences in thermal expansion coefficients of individual microscope parts, unstable mounting of the sample chamber, and small liquid currents inside the sample chamber. Troubleshooting an elusive noise source can be a frustrating experience, and in many cases, a better solution to eliminate the contribution of all of these noise sources is to separately measure the position of a fiducial marker and subtract it from the original trace[72].

In dual-beam trapping experiments, which are already decoupled from the surface, most noise can be eliminated by creating both traps with the same laser using a pair of AOD's. Commanding the AOD's to rapidly move the laser beam between the target positions, one can create time-shared traps that use the same optical path and the same detector[73]. When the position of the first trapped bead is subtracted from the position of the second, any external noise sources present in both signals nearly disappear. The concept is fully applicable to surface-coupled experiments, though it necessitates an additional step of immobilizing fiducial markers on the surface of the coverslip. I did not perform experiments with surface fiducials in our lab's main optical trap and the potential resolution gain from such real-time noise correction was not deemed necessary for my dynein experiments, but should higher-resolution surface-coupled experiments be required in the future I strongly recommend implementing fiducial-based noise correction instead of hunting for ever smaller sources of noise in the instrument.

Software design

Good software development practices are key to building a robust and reliable scientific instrument such as an optical trap. While a sloppy, "just get it done" approach to writing code may suffice for simple data analysis scripts or automating file manipulation tasks, it quickly results in ballooning development and troubleshooting times as the

project increases in complexity. It does not help that the *de facto* standard tool for scientific hardware control is LabVIEW, a graphical data flow language that gives new meaning to the old expression "spaghetti code". While LabVIEW code can be written in a clear and concise manner, the design of the language makes it easier for an inexperienced programmer to turn the simplest program into an unreadable tangled mess of wires. A large instrument control suite written in this style not only becomes impossible to debug, but also carries a very real risk of undetected persistent errors making their way into the acquired data files and compromising the validity of the experimental results.

There are only a few important practices which, if implemented from the very beginning, will help keep development times reasonable and ensure that the code remains readable and amenable to debugging as it grows. First, all code should be subdivided into logical sub-functions (termed subVIs in LabVIEW), each of which should ideally fit on a single monitor screen. Rather than serving as a container for some generally useful code, each subVI should carry out one specific task on a small number of inputs. If the programmer cannot describe in one or two sentences exactly what a given subVI does, its code is probably not logically partitioned. Proper subdivision also helps greatly with debugging if a subVI's expected behavior can be succinctly explained, it becomes easy to test whether it performs as expected by feeding a sample input into it and checking whether the output exactly matches the programmer's expectation.

Second, because LabVIEW's data structures (wires) represent data *flow* rather than data *storage*, the code quickly snowballs into a jumbled mess if care is not taken from the start to organize and bundle data flow. Perhaps the most useful, and underutilized, organizational feature of LabVIEW is wire clustering. If several pieces of information are used to describe the state of some logical entity (e.g. a photosensitive detector might simultaneously output four channels of data), there is no reason to have four separate wires run across the screen from one subVI that processes detector data to the next. Bundling related data makes the program easier to follow, troubleshoot, test, and update.

Finally, LabVIEW's clunky code annotation system and lack of variable names *per se* puts an extra burden on the programmer to document the program in a way that's easy for others to follow. The best way to ensure readability is to sub-divide the program into manageable logical chunks and connect the chunks using a few well-placed clustered wires. The last step towards readability is to assign meaningful names to all input and

output terminals of the individual subVIs. Note that every LabVIEW wire inherits the name of its source terminal, meaning that properly labeling the outputs of subVIs will automatically result in naming all wires running across the block diagrams. The end result is a top-level block diagram that fits on a single monitor screen and whose general logic flow can be parsed by following the names of subVIs and the relatively few high-level cluster wires connecting them.

FORCE GENERATION MECHANISM OF YEAST DYNEIN

The work presented in this chapter was published in the following paper: Belyy, V., Hendel, N. L., Chien, A. & Yildiz, A. Cytoplasmic dynein transports cargos via load-sharing between the heads. *Nat. Commun.* 5, 5544 (2014).

Introduction

Cytoplasmic dynein motors walk processively towards the MT minus end and generate forces of several pN[74,75]. The mechanical work produced by dynein motors has a broad range of cellular functions, including cargo transport, mitotic spindle positioning, and organization of the MT network[76]. Despite its central roles in neurobiology and development, the mechanism of dynein force production remained poorly understood in comparison with other molecular motors, in part due to its large size and complex structure[77].

Dynein is a homodimer of two ~500 kDa heavy chains. In contrast to kinesin and myosin, which have a single ATP binding site per motor domain, the dynein motor domain (head) contains six AAA+ ATPase subunits arranged into a hexameric ring (**Figure 2a**). Four of the AAA+ subunits bind nucleotide and the AAA1 subunit serves as the primary site of ATP hydrolysis. The AAA+ ring connects to a MT via a 15 nm coiled-coil stalk bearing a small MT binding domain (MTBD), resulting in a ~25 nm separation between the MTBD and the AAA1 site[78,79]. The two rings dimerize through an N-terminal tail domain, which also serves as the binding site for a number of light chains and adapter proteins[80]. Dynein-driven transport requires other components such as the cofactor dynactin, and regulatory proteins Lis1 and NudE[77].

The following model of dynein's mechanochemical cycle has been proposed to explain how a dynein monomer generates force. ATP binding to the AAA1 site[81] triggers the head's release from the MT and drives a priming stroke of the linker[82]. The linker, a long hinged domain at the base of the tail[83,84], undergoes large-scale conformational changes across the face of the AAA+ ring in an ATP-dependent manner[82,85,86] (**Figure 2b**). Notably, the linker exits the ring at the AAA4 site in the unprimed state and at the AAA2 site in the primed state. The priming stroke has been proposed to move the stalk and MTBD of the unbound head towards the minus end of the MT[82]. After ATP hydrolysis, the head re-binds to MT at a new location and releases inorganic phosphate[83]. The linker then undergoes a 'power stroke', generating tension in the

process and returning the monomer to its unprimed state[86]. While intramolecular tension has been proposed to play a significant role in dynein motility, the magnitude of this tension remains to be measured directly. The proposed model does not explain how much mechanical work is being produced by conformational changes of the linker and how two heads function together in a dimer to walk against a hindering load.
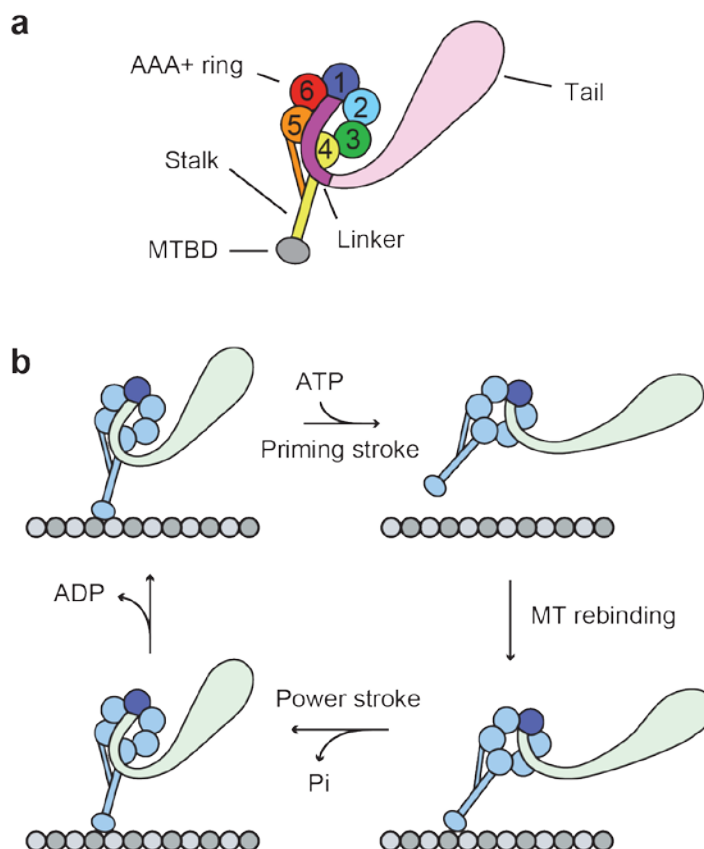

Figure 2. Domain organization and mechanochemical cycle of cytoplasmic dynein. (a) The dynein heavy chain consists of an N-terminal cargo-binding tail domain, an AAA+ ATPase ring attached to the tail via the mechanically active linker, and a microtubule binding domain (MTBD) separated from the AAA+ ring by a ~15 nm coiled-coil stalk. Individual AAA subunits are numbered 1 through 6. (b) Following the binding of ATP at the principal ATPase site (AAA1, colored dark blue), the dynein head releases from the MT and its linker undergoes a priming stroke. The primed linker exits the ring at AAA2 rather than AAA4, and a dynein monomer attains an extended conformation. After the head re-binds the MT, its linker undergoes a power stroke, returning to its initial conformation exiting the ring at AAA4. The AAA1 site then releases ADP, completing the mechanochemical cycle.

In this study, we use a head-tethered optical trapping geometry[14] to directly observe the force production and stepping of individual heads of a walking dynein dimer. We find that each head relies on diffusion to travel to the next binding site on the MT following its priming stroke. Force is then produced by the power stroke after the head rebinds to the MT. The stall forces of the two heads are approximately additive despite the absence of coordination in their stepping, leading us to propose a load sharing model for dynein-driven cargo transport. These results reveal unique properties of dynein force generation in comparison with other cytoskeletal motors.

Results

Development of head-tethered dynein geometry

Force production of cytoskeletal motors has been studied extensively by attaching an optically trapped bead to the dimerization domain. Such assays directly measure the step size and stall force of the motor's tail[75], providing detailed information about the load dependence of each head's stepping kinetics under the assumption that the heads alternately take steps and swap the leading position. However, dynein's heads can adapt a wide variety of orientations and step independently of each other[19,21]. Therefore, not much can be learned about the force production and stepping of an individual head from these assays.

In order to characterize the behavior of a dynein head under load, we linked an optically trapped bead to one of the heads at the C-terminus of GST-Dyn1$_{331kDa}$, a tail-truncated *S. cerevisiae* dynein dimerized with glutathione S-transferase (GST). This construct takes steps of the same size and duration as full-length dynein[17], stalls at approximately 70% of full-length dynein's stall force[75], and is herein referred to as WT. Dynein was covalently linked to a DNA tether at its C-terminus (**Figure 3a**). The labeling efficiency of the DNA tether to dynein was adjusted (**Figure 3b)** to be <15% to minimize the likelihood of dual labeling. The length of the tether (74bp, 25nm) was sufficiently long to minimize steric hindrance from the trapped bead on the walking molecule. To test the impact of C-terminal DNA tethers on dynein motility in unloaded conditions, we labeled the distal end of the tether with Cy3 and observed the motility of DNA-tagged motors in a single-molecule fluorescence assay (**Figure 3c)**. Labeled motors remained active and processive, walking at 98 ± 9 nm s^{-1} (mean $\pm$ s.e.m., N = 73), slightly slower than DNA-free motors tagged with GFP (117 ± 7 nm s^{-1}, N = 64). These results show that dynein's motility is not significantly hampered by the presence

of a DNA tether. Yet, the tether remains relatively rigid[87] and does not introduce excessive noise into the trap recordings. The distal ends of the DNA tethers were attached to polystyrene beads through a biotin- streptavidin linkage.

Effects of load on stepping and force production of a head

Using a similar geometry, it has been shown that a kinesin-1 head takes twice the steps size of the tail, but its stall force halves relative to that of the tail[14]. This is consistent with the energetics of a kinesin step, which harnesses the hydrolysis energy from one ATP and produces the same amount of work[88]. Because dynein lacks a regular stepping pattern[19,21] and possesses multiple ATP hydrolysis sites, a dynein head may respond differently to external load, which would in turn affect its measured force production. To test this, we compared the stall force of a DNA-tethered dynein head to the combined force production through the tail domain (**Figure 3d**). Unlike kinesin, the head-tethered motor stalls at a force of 3.0 ± 0.1 pN (mean $\pm$ s.e.m.), similar to the stall force of the tail-tethered motor (3.1 ± 0.1 pN, mean $\pm$ s.e.m.) (two-tailed t-test, p $= 0.28$) (**Figure 3e,f**). These values are in agreement with the tail-tethered force measurements using the same construct (Arne Gennerich, personal communication). Stall forces are not affected by the C-terminal fusion of the HaloTag (HT) domain, because a construct with an N-terminal HT fusion stalls at similar forces.

Next, to determine the effect of load on the stepping of a dynein head, we collected and analyzed position traces of head- and tail-tethered dynein motors under near-stall (2.5 pN) hindering loads in the presence of saturating (1 mM) ATP (**Figure 4a**). The size of steps taken by the DNA-tethered head (12.1 ± 6.7 nm backward and 11.0 ± 5.1 nm forward steps, mean $\pm$ s.d.) was indistinguishable (two-tailed t-test, p $= 0.67$) from the size of steps measured at the tail (12.7 ± 5.7 nm backward and 12.3 ± 5.6 nm forward steps) (**Figure 4b**). This is consistent with our previous observation that stall forces remain the same between the two geometries because one ATP-driven step is capable of generating a specific amount of work, which is a product of force and step size. Moreover, stepping rates remained similar between the two geometries (10.2 ± 0.5 s^{-1} head-tethered, 10.6 ± 0.5 s^{-1} tail, mean $\pm$ 95% conf. interval) **(Figure 4c)**. This is in contrast to unloaded
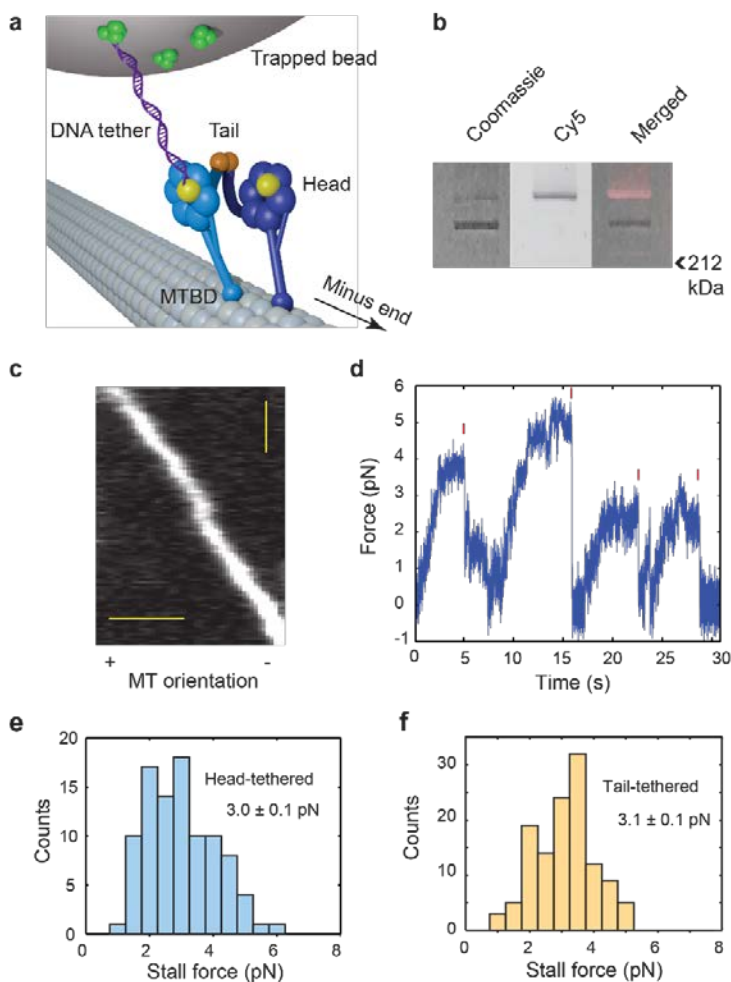
Figure 3. Measuring forces produced by a single dynein head. (a) Schematic of the head-tethered optical trapping assay for measuring forces produced by a single dynein head. One head of a GST-dimerized motor (GST shown in orange) is labeled with a DNA tether at the C-terminal HT tag (yellow), and tethered to a trapped bead through a biotin-streptavidin (green) linkage. (b) Cy5-DNA labeled dynein migrates in two distinct bands in a denaturing gel. Fluorescent image identifies the labeled fraction. Labeling efficiency was 31% in the gel shown here. (c) Kymograph shows that Cy3-DNA labeled dynein moves processively towards the MT minus end. Scale bars: 2 µm (horizontal), 10 s (vertical). (d) Measurement of the stall force of head-tethered dynein. Valid stall events are marked with red ticks. Trap stiffness (k_{trap}) is 0.037 pN nm^{-1}. (e,f) Stall force histograms of head- and tail-tethered dynein motors, respectively (mean ± s.e.m.; N = 97 and 123, respectively).

conditions, in which the head takes nearly twice the center-of-mass step size and steps less frequently[17,19]. Our findings indicate that the DNA-tethered head decreases its step size to match that of tail-tethered dynein[17] under load.
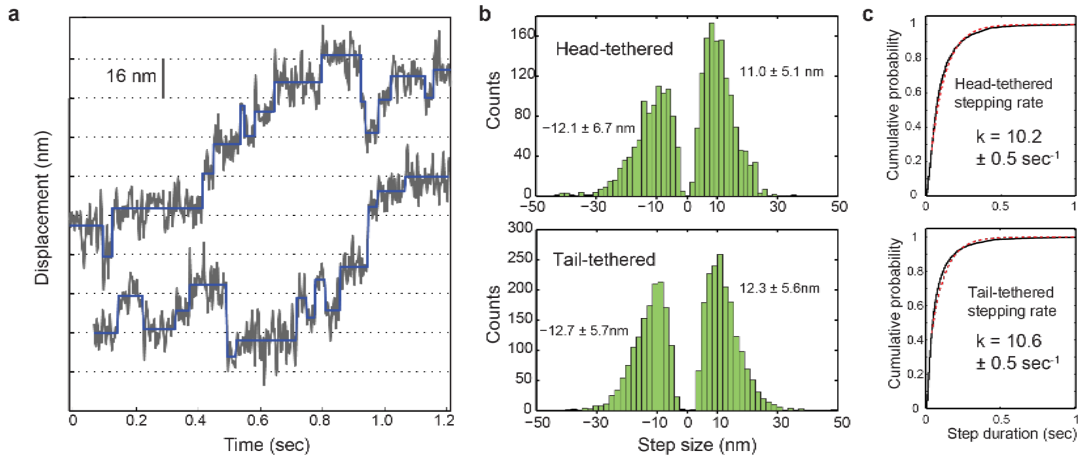
Figure 4. Observation of steps taken by a dynein head under load. (a) Stepping traces of head-tethered dynein in force-feedback mode under 2.5 pN hindering load. Position traces (gray lines) are decimated to 330 Hz. The output of the step-fitting algorithm is shown in blue (k_{trap} = 0.025 pN nm^{-1}). (b) Step size distributions of head- and tail-tethered motors under 2.5 pN hindering load (mean ± s.d.; N = 2300 and 3293, respectively). (c) Stepping rates (k) of head-tethered and tail-tethered motors under 2.5 pN hindering load, obtained by fitting cumulative probability distributions (solid black lines) to single exponentials (dashed red lines). Reported values are mean ± 95% confidence interval boundaries.

Measurement of force generated by dynein's power stroke

The linker swing mechanism is essential for force generation and motility of dynein motors[81,86]. It has been proposed that force is produced in the MT-bound state, as the linker transitions from the primed to unprimed conformation. On the other hand, the linker undergoes a priming transition as it releases from MT, and this was proposed to drive the movement of the stepping head towards the minus end[82]. It remains unclear how much work is performed by each of these conformational changes. To address this question, we measured the stall force and step size of a dynein heterodimer in which one head is rendered catalytically inactive. Force production in one head was abolished by introducing a K/A mutation in the Walker A motif of the AAA1 site, preventing ATP from binding[89]. The mutant ($AAA1_{K/A}$) head was dimerized with a WT head using an N-terminal FRB-FKBP12 tags (WT/$AAA1_{K/A}$, **Figure 5a**)[17]. Constructs dimerized via the FRB-rapamycin-FKBP12 chemistry exhibit similar processivity and stepping properties to GST-dimerized dynein[17]. The stall force of head-tethered FRB/FKBP12-dimerized WT/WT dynein is similar (3.0 ± 0.1 pN, t-test, p = 0.90, N =13) to the

GST-dimerized construct, verifying that heterodimerization tags do not hinder the motor's force production.

By attaching the DNA tether to either the WT head or the mutant head, we were able to separately investigate the energetics of the two strokes. Because the mutant ($AAA1_{K/A}$) head remains in an unprimed, tightly-bound state, and is incapable of undergoing a power stroke[85], motility is powered solely by the active (WT) head. High resolution tracking studies of this construct showed that WT head mostly remains in the lead and drags the mutant head forward[90]. The force required to pull the mutant head is likely supplied by the power stroke of the WT head and transmitted via linker tension. In contrast, when the tether is directly attached to the sole active head, this head must step forward against load without any assistance provided by its inactive partner. An active dynein head releases from the MT and moves forward as its linker is primed. It is possible that, during this motion, the MT-bound head serves as an anchor that the stepping head actively pushes away from through the priming stroke of its linker [82]. Therefore, we expect stall force measurements in the WT head-tethered geometry to test whether the priming stroke of the linker produces mechanical work during the stepping of a head.

The $WT/AAA1_{K/A}$ heterodimer walks processively at 13.6 ± 1.2 nm/s. When the DNA tether was attached to the $AAA1_{K/A}$ mutant head, the motor stalled at half the stall force of the WT/WT homodimer, 1.5 ± 0.4 pN (mean $\pm$ s.d., **Figure 5b,c**). Because the DNA-tethered head is catalytically inactive, this assay constitutes a measurement of the minimal amount of force generated by dynein's powerstroke. The step size of the mutant head at near-stall (1.5 pN) hindering load was slightly lower than that of the WT head at 2.5 pN hindering load (9.5 ± 6.2 nm for backward steps and 8.5 ± 5.5 nm for forward steps), and the stepping rate was approximately 2.5 times lower than that of a WT head at 3.6 ± 0.3 s^{-1}. The stall force of a head remained nearly constant across 20 µM to 1 mM ATP (**Figure 5d**). The lowest tested ATP concentration of 20 µM is less than half of the $K_{M\ (ATP)}$ of the $Dyn1_{331kDa}$ construct used in this study (45 µM, data not shown)[91]. This contrasts with kinesin-1 that stall force decreases at limiting ATP concentrations[92]. Our results are consistent with the observation that the stall force of the dynein center-of-mass does not depend on ATP concentration[75]. Furthermore, because a stalled dynein is effectively in equilibrium between forward and backward steps, our finding suggests that both forward and backward steps are governed by the same ATP-dependent rate and slow down proportionately when ATP is limiting.
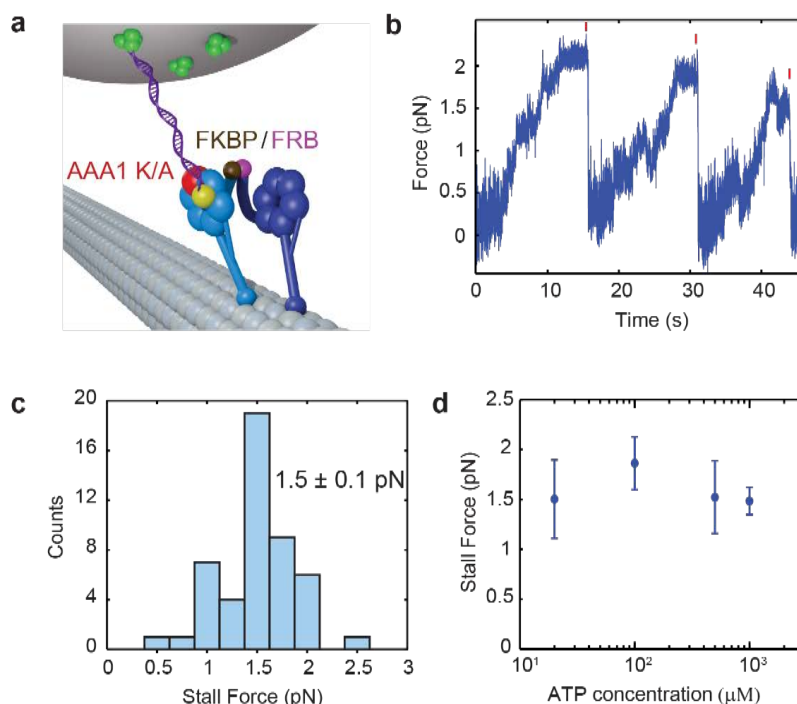
Figure 5. Behavior of a mutant head under load. (a) Schematic of the mutant head-tethered optical trapping assay. The DNA tether is attached to an $AAA1_{K/A}$ mutant head, which cannot bind ATP at the AAA1 site. The mutant head is heterodimerized with a WT head through rapamycin-induced FRB/FKBP binding. (b) Stall force measurement of a mutant-head tethered heterodimer at 1 mM ATP (k_{trap} = 0.017 pN nm^{-1}). (c) The mutant head-tethered construct stalls at half the stall force of WT (mean ± s.d.; N = 48) (d) Stall force of the mutant head-tethered construct is independent of ATP concentration. Error bars represent s.e.m. N = 48 to 88 stalls for each data point.

Priming stroke does not generate substantial work

To test whether the priming stroke of the linker produces mechanical work as the WT head searches for a new MT binding site, we attached the DNA tether to the WT head of the heterodimer (**Figure 7a**). In contrast with our previous finding that mutant head-tethered heterodimers stall at half the stall force of the WT/WT homodimer, we measured the stall force of the live head-tethered construct to be as low as 0.5 ± 0.1 pN (mean ± s.d.) (**Figure 7b,c**). This force corresponds to an energetic bias of ~1.5 k_BT at room temperature, assuming an average step size of ~12 nm[17]. Therefore, a single dynein head is only minimally biased to move forward when it is not bound to the MT and is unable to generate appreciable forces in the unbound state. To rule out the

possibility that the extremely low forces produced by the WT head-tethered construct are not caused by a loss of processivity upon DNA attachment, we verified that this construct still walks processively for hundreds of nanometers when subjected to sub-stall loads of 0.3-0.4 pN (**Figure 7d**). The differences we observe between applying force to the two different heads of the WT/AAA1$_{K/A}$ heterodimer can be rationalized by considering the fundamental difference between pulling directly on the 'active' head and pulling on its inactive partner. In the first case, the head must move against the force of the trap at all times, even during the diffusional search for a new binding site after ATP-induced release from the MT. In the second case, the 'active' head is allowed to diffuse freely in the MT unbound state while the inactive head remains bound to the track and bears the load exerted by trap. In this case, the active head needs to perform work against the trap in the MT-bound state to pull its inactive partner forward. Our findings show that force required for dynein motility is produced once the stepping head re-binds the MT and the linker returns to its unprimed conformation (**Figure 7e**). The priming stroke only generates minimal mechanical work and is insufficient to account for the force generation of a WT dynein dimer.

We next tested the possibilities that interactions between the two AAA+ rings or the remaining ATPase active sites in the mutant head could influence the stall force of WT/AAA1$_{K/A}$. We repeated both WT head-tethered and mutant head-tethered stall force measurements using a construct in which the AAA1$_{K/A}$ head is replaced with seryl tRNA synthetase (SRS) fused to a dynein MTBD[90,93] (**Figure 6a,b**). In this heterodimer, only the 'live' head has a motor domain, while the SRS chimera acts as a true mechanical tether without the possibility of ring stacking or residual motor activity. Despite having only one functional dynein head, this construct walks robustly and is threefold slower but twice as processive as WT/WT [90]. We measured the stall force of the SRS-tethered heterodimer to be 1.6 ± 0.6 pN (mean ± s.d.), and of the live head-tethered heterodimer to be 0.5 ± 0.2 pN (mean ± s.d.) (**Figure 6c-f**). The results are similar to those of the WT/AAA1$_{K/A}$ heterodimer (two-tailed t-test; SRS- tethered, $p = 0.20$; WT head-tethered, $p = 0.77$). These findings also indicate that tension experienced by the mutant head must be transmitted through the linker, and not through ring-ring interaction.
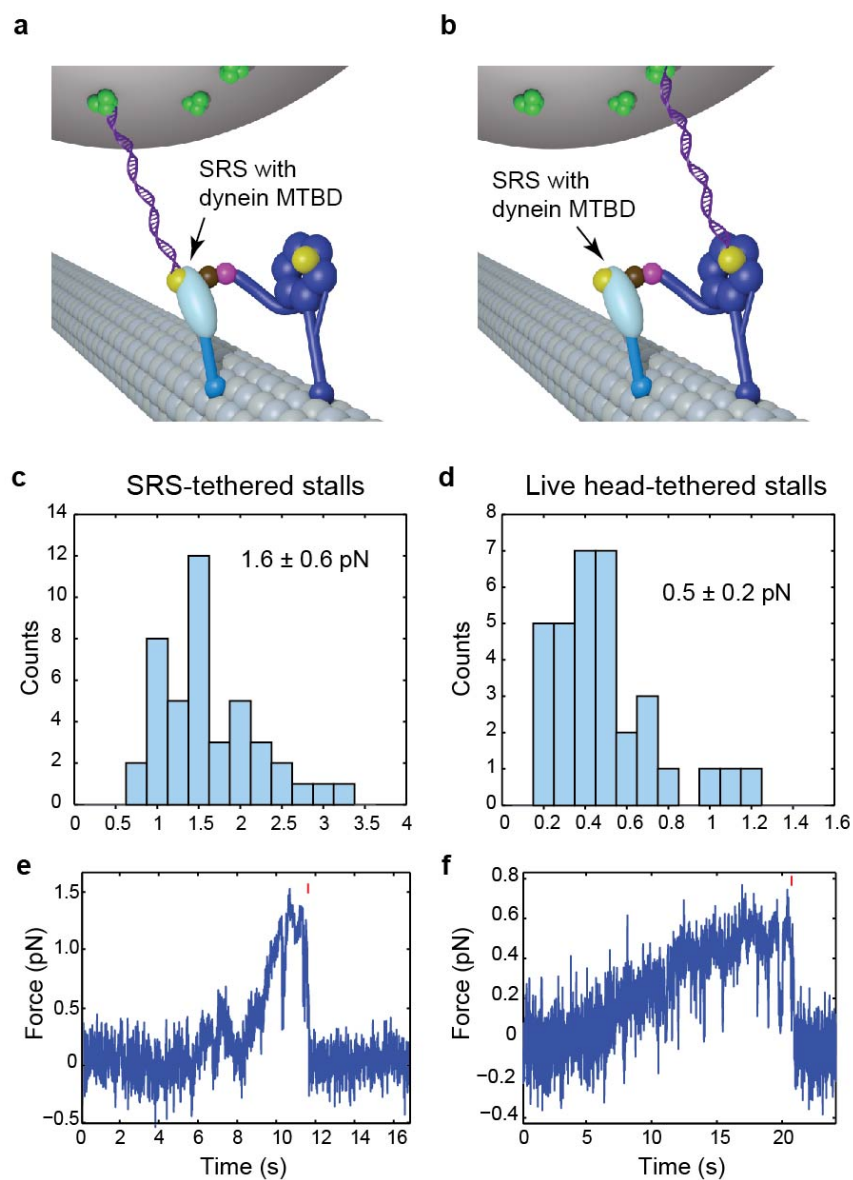
Figure 6. Confirmation of AAA1$_{K/A}$ results using an SRS fusion 'peg leg'. (**a**) Geometry for mutant head-tethered experiments. The DNA tether is attached to the SRS 'peg leg', which is heterodimerized with a WT head, which is heterodimerized with an SRS 'peg leg' through rapamycin + FRB/FKBP. (**b**) Geometry for live head-tethered SRS experiments. The DNA tether is attached to a WT head. (**c**) Stall force histogram of the SRS-tethered WT/SRS construct (mean ± s.d.) (**d**). Stall force histogram of the live-head tethered WT/SRS construct (mean ± s.d.) (**e,f**) Stall force traces of SRS-tethered and live-head tethered constructs, respectively.

Figure 7. Characterization of a WT head of a WT/AAA1$_{K/A}$ heterodimer under load. (a) Schematic of the WT head-tethered optical trapping assay. The DNA tether is attached to WT head,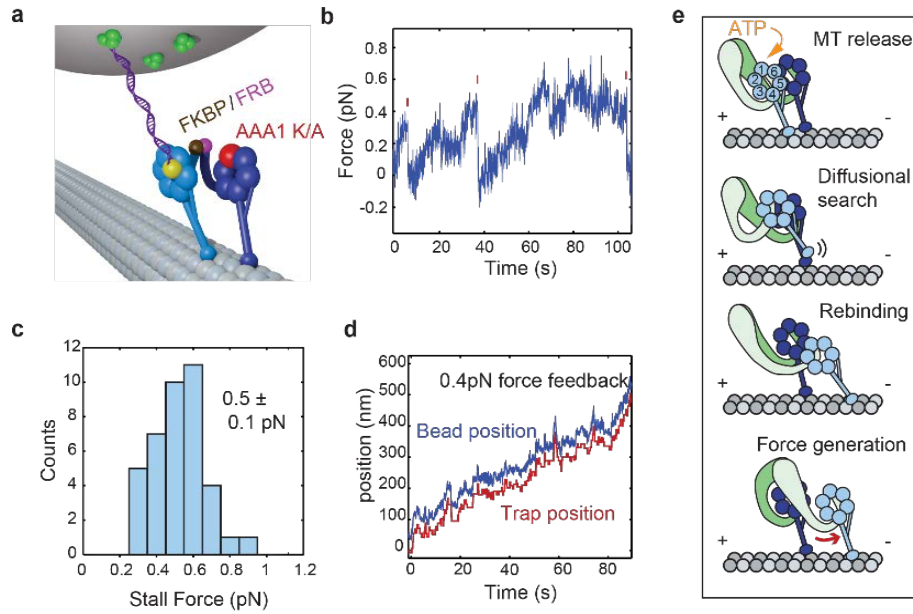 which is heterodimerized with an AAA1$_{K/A}$ mutant head. (b) Stall force measurement of the WT-head tethered heterodimer ($k_{trap} = 0.008$ pN nm^{-1}). (c) WT-head tethered heterodimers stall at lower forces (0.5 ± 0.1 pN, mean ± s.d.; N = 39) than the mutant-head tethered motors. (d) Despite having a very low stall force, the live-head tethered construct is able to move processively over long distances against sub-stall (0.4 pN) hindering loads ($k_{trap} = 0.008$ pN/nm). (e) Model illustrating dynein force-production in the MT-bound state. Upon releasing from the MT, a dynein head undergoes a priming stroke. This component of the step is highly diffusional and can be biased backwards by external load. The force-generating step occurs after the head binds to a new site on the MT lattice.

Force-velocity relationship of a dynein head

To investigate how the overall motility of a dynein dimer is affected by load when one or both heads are able to produce force, we measured the velocities of head-tethered WT/WT and mutant head-tethered WT/AAA1$_{K/A}$ under varying loads at saturating (1 mM) ATP. The shape of a motor's force-velocity (F-V) curve is determined by how forward and backward stepping rates are affected by external load[92,94]. Our findings differ from the F-V relationship previously reported for full-length dynein in center-of-mass trapping geometry[75]. The velocities we observe increase continuously as external force transitions from hindering to assisting values. There is no detectable plateau at

near-zero forces, suggesting that the principal rate-limiting transition in the step of a dynein head involves substantial movement along the MT axis.

The F-V curve fits well ($R^2 = 0.975$) to a simple one-state motor model (**Figure 8a**), wherein the movement of a motor is fully described by a single load-dependent forward stepping rate and a single load-dependent backward stepping rate (see **Methods**). Interestingly, the best fit assigns all load dependence to the forward stepping rate and keeps the backward rate constant across the entire force regime. The load-dependence of the forward and backward stepping rates can also be independently estimated from stepping data. Comparing the stepping rates of a DNA-tethered head under 2.5 pN hindering load to the stepping rate of a dynein head in unloaded conditions[19], we find that the forward rate decreases from 11.3 s^{-1} to 5.8 s^{-1}, while the backward rate increases from 2.8 s^{-1} to 4.4 s^{-1}. The decrease in forward rate is significantly larger than the increase in backward rate and is responsible for the bulk of the observed dramatic decrease in velocity under load. Meanwhile, the forward step size of the head under load (11.0 nm) remains very similar to the mean step size of an unloaded head (10.2 nm), emphasizing the importance of stepping rate rather than step size in velocity measurements. The results are consistent with the finding that dynein monomers release from MT in a force-dependent manner, with assisting (minus-end directed) forces greatly accelerating MT release, and hindering forces having little effect on release rates[90].

The asymmetric response of a dynein monomer to load could arise from force-dependent inhibition of a particular step in the ATPase cycle. Alternatively, the interaction between the MTBD and the tubulin binding site may become stronger as force is applied in a particular direction. To distinguish between these possibilities, we repeated F-V measurements using the mutant head-tethered WT/AAA1$_{K/A}$ construct (**Figure 8b**). If the force dependence of velocity of the WT head originated from one of the ATPase steps, such as nucleotide binding or hydrolysis, one would expect a different step to become rate-limiting in the AAA1$_{K/A}$ head-tethered construct since this head does not perform an ATP-dependent linker swing[85]. A novel rate-limiting step would in turn result in a different F-V relationship. We observed that the mutant head-tethered construct exhibited a concave-up F-V curve, similar to WT/WT. The ΔG parameter, which represents the effective energetic bias from ATP hydrolysis per step in our simple model, is almost exactly twice as large in WT/WT (4.8 pN·nm) as it is in the AAA1$_{K/A}$ head-tethered construct (2.5 pN·nm). This is consistent with our observation that constructs with two active heads are able to pull against twice the stall force of mutant heterodimers. Although WT/AAA1$_{K/A}$ is nearly four times slower, the characteristic

length *L*, which determines how rapidly the motor's velocity scales with force, remains nearly identical (1.6 nm) to that of WT/WT (1.8 nm). The results suggest that the different response of forward and backward stepping rates to load arise from the asymmetry of the MT binding interface. It has been shown that the dynein MTBD behaves as a catch bond under load, as hindering forces slow down its ATP-dependent release from the MT[90]. The characteristic length arising from our F-V curve may thus correspond to a distance by which the head needs to move in order to release the catch bond of the MTBD.
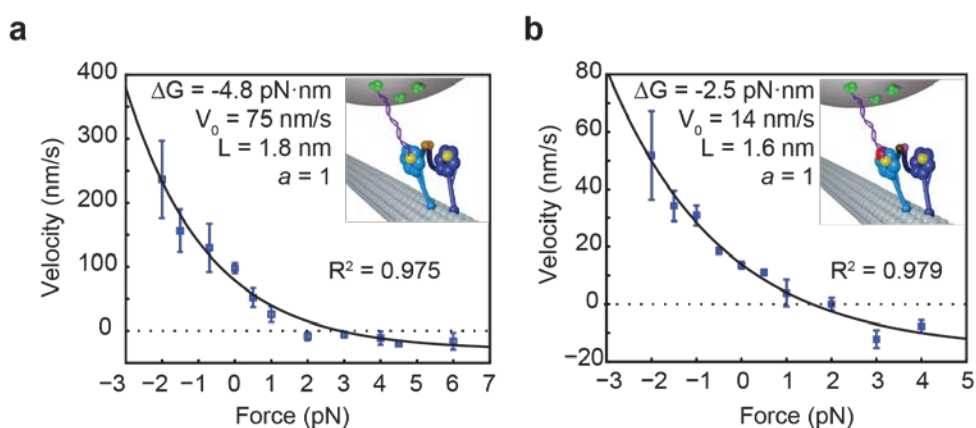

Figure 8. WT and AAA1$_{K/A}$ force-velocity relationships. Force-velocity curves for head-tethered WT/WT homodimer (a) and mutant head-tethered AAA1$_{K/A}$ heterodimer (b) at 1 mM ATP are fitted with a one state model in which the backward stepping rate is load independent (black curve). The parameters obtained from the fit are the unloaded velocity V0, the characteristic length L, and the minimum velocity V$_{min}$. Error bars represent S.E.M (N$_{beads}$ = 4-10). Velocities at "0 pN force" were obtained from single molecule fluorescence measurements (N$_{motor}$ >60).

Discussion

Characterizing the behavior of both WT and mutant heads under load allowed us to provide a mechanistic description of the force production by the two heads of a walking dimer. The force is generated mainly in the MT bound state, consistent with the powerstroke model[95]. Our force measurements set a lower bound for the force produced by a power stroke at 1.5 pN (**Figure 5**). This force also constitutes a measurement of the maximal force with which one head can pull on its partner head through linker tension. While the priming stroke of the unbound head has been proposed to push against the MT-tethered head and drive motility towards the MT minus end[82], we found

that it provides less than 1.5 k_BT of directional bias per step and thus cannot account for the mechanical work performed by dynein over one mechanochemical cycle. However, the priming stroke remains vital to dynein's mechanochemical cycle as it is likely to increase the reach of the diffusional step and prime the linker to enable an effective subsequent powerstroke.

We demonstrated that a dynein head is able to generate half the stall force of the dimer. Given dynein's flexibility and lack of strict interhead coordination, the heads in a dynein dimer can be thought of as a pair of mechanically coupled monomers as opposed to a single cyclic machine akin to myosin V or kinesin-1. We propose that each of dynein's monomers is capable of independently generating approximately half of the stall force of the dimer, and that each head's force production contributes to the total output of the dimer. We refer to this framework as 'load-sharing' between dynein heads to highlight its similarities with the additive forces observed when a cargo is driven by a low number of processive motors[96–98].

Our vision of how load sharing may be achieved in cytoplasmic dynein is illustrated in **Figure 9**. A dynein dimer spends the majority of the time with both heads bound to the MT. Unlike kinesin and myosin, the hindering load is distributed among both heads with their long flexible tails acting as springs (**Figure 9, i**). When one head releases from the MT, the entire load is transferred to the bound head (**Figure 9, ii**). The bound head functions as an anchor while the released head performs a diffusional search for a new binding site. During this diffusional search, the tail may briefly move backwards in response to external load, but we expect this motion to be too rapid to be resolvable given the ~3 ms time resolution of our assay. When the stepping head rebinds to MT (**Figure 9, iii**) and its linker undergoes a power stroke (**Figure 9, iv**), load is redistributed between the heads. The tail of the leading head becomes more stretched, as this head bears a larger fraction of the total load. Since hindering force significantly decreases the rate at which a dynein head releases from the MT[90], the leading head now serves as an anchor while the trailing head becomes more likely to take the subsequent step. Importantly, the work done by the power stroke of each head is stored in the form of linker tension and is applied to bias the subsequent step of the partner head against hindering load. As a result, each step effectively combines the force-generating capacities of the two partner heads, allowing a dynein dimer to work against hindering forces higher than the maximal force produced by each head.

A distinguishing feature of dynein's motility under load is that the step size and stepping rate of a DNA-tethered head are the same as the size and rate of steps

measured when the load is applied to the tail. This unusual finding can be explained by the large and flexible structure of the dynein dimer and tension-dependent changes in dynein's stepping pattern[90] **(Figure 10)**.
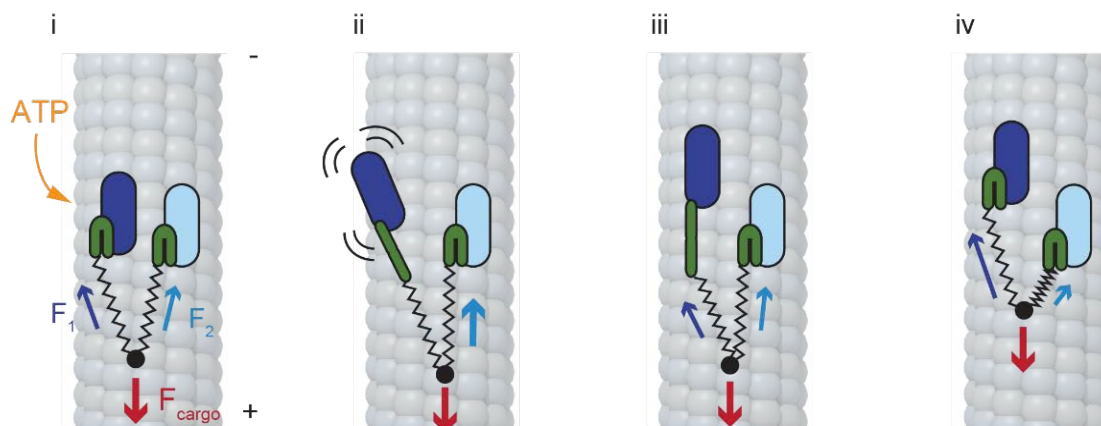

Figure 9. Load-sharing model for dynein force production. (i) When dynein is in a two-head bound state, the external load (F) is distributed between the two heads due to the elastic nature of the tail (stretched springs) and linker (bent green rods) regions. Because each panel represents an equilibrium state, the sum of the three forces (F_{cargo}, F_1, and F_2) is always equal to zero. (ii) ATP binding to the AAA1 site of one head triggers its release from the MT and priming of the linker (straight green rod). As this head diffuses to a new binding site, the external load is transferred in its entirety to the DNA-tethered head (iii) The stepping head rebinds to MT, with the linker still in the primed configuration. (iv) The linker returns to its original state via a powerstroke, the tail moves forward and the load is redistributed between the heads. Load sharing allows a dynein dimer to work against hindering forces larger than the forces that can be produced by a single head.

Our findings further distinguish dynein from other cytoskeletal motors and provide new clues for understanding how it functions *in vivo*. Unlike kinesin-1, which readily releases from the MT at near-stall loads[92], the dynein MTBD resists large backwards loads[90]. This may make dynein ideally suited for transportation of large cellular cargos or sliding of MTs under tension. The heads of a dimer produce force independently and they must be inhibited simultaneously by a regulatory protein to stall dynein movement[19,30]. A dimer with a single head inhibited would behave similarly to our WT/AAA1$_{K/A}$ heterodimer, slowing down by several fold yet still producing substantial force. Independent force generation can also enable dynein to perform work in unusual environments such as at the ends of MT's or while crosslinking two MTs and sliding

them relative to each other[99], and can potentially aid the understanding of collective force production by trimeric outer-arm dyneins[100]. Finally, it has been reported that multiple dyneins combine their efforts more effectively than do multiple kinesins[50]. The load-sharing mechanism inherent to a single dimer may explain dynein's enhanced ability to pull cargos when working in a team. In a system with multiple motors transporting the same cargo, individual motors experiencing a hindering force will tend to remain attached to the track and prevent the cargo from slipping backwards. Meanwhile, motors that are not subjected to a significant hindering force will have a much higher probability of stepping forward, resulting in self-regulating and efficient minus-end directed transport by multiple motors.
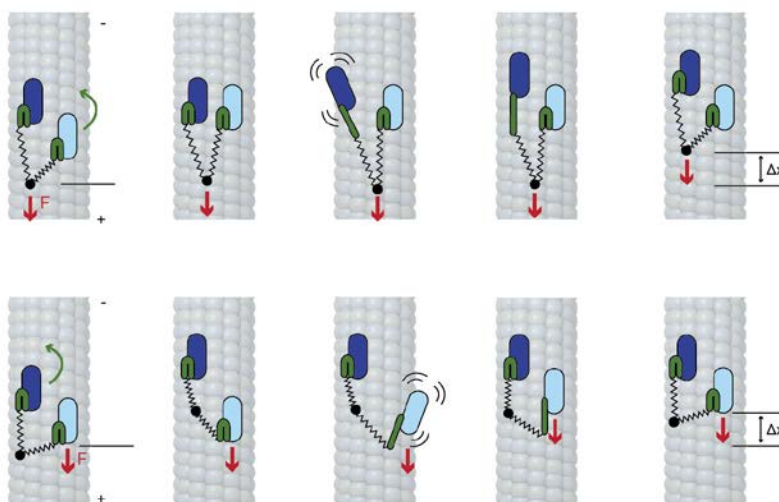

Figure 10. Putative model for step measurements of dynein motors under load. (Top row) When load is applied from the tail, the leading head bears a larger fraction of the load and is inhibited from taking an additional step. When the heads are not located side-by-side, the load is mainly resisted by the leading head's linker. A step taken by the trailing head does not significantly change the position of the tail attachment point (black dot) under tension because of the high compliance of the tail in at low and intermediate tensions. Only the steps when either of the heads advances the leading position are detectable in this geometry (detectable step represented with Δx; see Methods for a discussion of spatiotemporal constraints on step detection). (Bottom row) In a head-tethered trapping geometry, the tethered head likely remains in the trailing position and is assisted by the leading head via linker tension. Only the tethered head's steps are resolvable in this experiment. As a consequence, the trap generally detects steps of only one of the heads in both head- and tail- tethered assays, leading to the observed similarities between measured stepping rates and sizes.

Methods

Preparation of DNA tethers

Double-stranded DNA tethers labeled with HT ligand (Promega) on one end and biotin on the other were prepared as follows. A biotinylated DNA oligo (5'-/biotin/TTC GGT CAA TAC CCG GCG CAG AGC GCT CAG GCG CGA GGT CAA CAG AGG GCG GAG GGT GGG CCA GCG CGA CCC CG-3') was hybridized with an amine-modified DNA oligo (5'-/C6 amino/GTG TCG GGG TCG CGC TGG CCC ACC CTC CGC CCT CTG TTG ACC TCG CGC CTG AGC GCT CTG CGC CGG GTA TTG AC-3') in DNA buffer (20 mM NaHCO₃, 50mM KCl, 1.25 mM MgCl₂, pH = 8.4) at 90°C for two minutes, followed by incubation at 25°C for 40 minutes. An amine-reactive HT Succinimidyl Ester (O4) ligand (Promega) was then attached to the terminal amine group on the DNA by incubation for 6 hours at room temperature. The reaction was then quenched with 1mM glycine for 10 minutes to remove excess reactive ligand. The resulting tethers were sequentially de-salted into DLB buffer (30 mM HEPES, 2 mM MgCl2, 1 mM EDTA, 10% glycerol, pH 7.2) through two G-25 columns (GE Healthcare). De-salted tethers, at ~25 µM concentration in DLB, were frozen and stored at -20°C. Fluorescently labeled DNA molecules were prepared exactly as described above, except the biotinylated oligo was replaced with a 5' Cy3-modified oligo with an identical nucleotide sequence.

Protein purification

S. cerevisiae cultures expressing the dynein constructs used in the study were grown to an OD600 of 1.0-1.5. They were then harvested by centrifugation and the pellets were resuspended in ~3mL of water per liter of starting culture. The resuspended pellets were frozen by dripping into liquid nitrogen and lysed by grinding in a commercial stainless steel coffee grinder (KitchenAid; pre-cooled with liquid nitrogen) for ~30 seconds. Following lysis, the ground powder was thawed in a 37°C water bath concurrently with the addition of 0.2 volumes of 5X lysis buffer (150 mM HEPES, 250 mM KAcetate, 10 mM MgAcetate, 5 mM EGTA, 5 mM PMSF, 500µM MgATP, 50% glycerol, pH 7.4). Note that due to their long-term instability in solution, PMSF and MgATP were stored separately and were only added to the stock buffer immediately preceding dynein purification. The resuspended lysis mixture was then centrifuged at 270,000 g for 45 min. The resulting supernatant was mixed with 200 µL of IgG sepharose beads (GE Healthcare Life Sciences) and incubated with rotation at 4°C for 1 hr. The beads were

then washed twice with wash buffer (125 mM KCl, 30 mM HEPES, 50mM KAcetate, 2 mM MgAcetate, 1 mM EGTA, 1 mM PMSF, 100 µL MgATP, 10% glycerol, pH 7.4) and washed once with 10 mL of TEV buffer (150 mM KCl, 10 mM Tris-HCl, 10% glycerol, 1 mM TCEP, 1 mM PMSF, 100 µM ATP, pH 8.0). Following the wash, beads were incubated with TEV protease in 500 µL of TEV buffer for at 16°C for 1hr with rotation. The dynein-containing supernatant was then either immediately labeled with DNA tethers or aliquoted and flash-frozen if labeling was not necessary. .

Labeling

After TEV cleavage, dynein was mixed with an excess of de-salted tethers (e.g. 300 µL of 200 nM dynein and 100 µL of 25 µM tether) and nutated at 4°C for 5 hours. At the end of the labeling reaction, the microtubule bind and release (MTBR) protocol was used to remove excess DNA and enrich the population of active motors. For MTBR, freshly prepared microtubules (MT's) were suspended in dynein lysis buffer supplemented with 10 µM taxol (DLB: 30 mM HEPES, 50 mM KAcetate, 2mM MgAcetate, 1mM EGTA, 10% glycerol, pH 7.4*)* at a concentration of ~2 mg/mL, then added to 5 volumes of ~200 nM dynein and incubated for 7 min at room temperature. The dynein/MT mixture was then layered over 200 µL of sucrose cushion (DLB supplemented with 50% sucrose and 10 µM taxol) in an ultracentrifuge tube (Beckman TLA 120.2) and centrifuged at 54,000 g for 10 min at 23°C. The pellet was washed twice with 200 µL of wash buffer (DLB supplemented with 1 mM DTT and 10 µM taxol) and resuspended in ~200 µL of release buffer (DLB supplemented with 300 mM KCl, 2 mM MgATP, and 500 µM DTT). The resuspended pellet was allowed to incubate in release buffer for 10 min at room temperature and then centrifuged at 54,000 g for 10 min at 23°C. The supernatant of this second centrifugation run contained purified DNA-labeled dynein with excess tethers removed. . Fractions from MTBR purification were then analyzed on a denaturing gel. All dynein constructs used in this study were artificially dimerized with either GST or rapamycin-mediated FKBP– FRB binding. >96% of the GST-dimerized constructs were labeled with a single DNA. For tail-tethered dynein experiments, HT-GST-Dyn1$_{331kD}$ was labeled with a biotinylated HT ligand at the N-terminal HT. The FRB-FKBP pair was used whenever the experiment required heterodimerization between a mutated head and a wild-type (WT) head.

Conjugation of motors to microspheres

0.9 µm carboxyl latex beads (Life Technologies), were coated with either streptavidin or custom-made rabbit polyclonal αGFP antibodies (Covance) as follows. The beads were washed four times in activation buffer (10 mM MES, 100 mM NaCl, pH 6.0) by vortexing, spinning down at 10,000 RCF for 3 min and resuspending. 1 mg each of EDC and Sulfo-NHS crosslinkers (Pierce Biotechnology), dissolved in 100 µL of DMF, were then added to the beads. The solution was sonicated for ~5 min and vortexed at low speed until visible clumps disappeared. Afterwards, the beads were washed 3 times with coupling buffer (100 mM sodium-phosphate buffer, pH 7.4), mixed with streptavidin or antibodies (at ~1 mg of dry streptavidin or antibody per 100 µL of 4% v/w bead stock) and reacted with shaking at room temperature for 30 min. The labeled beads were then passivated by adding powdered BSA to a final concentration of 10 mg/mL and shaking for 1.5 hrs at room temperature. Passivated beads were washed three times with 1x PBS (Phosphate Buffered Saline, pH 7.4) and stored at 4°C with 0.1% sodium azide and 0.5 mg/mL BSA.

Sample preparation

In FRB/FKBP12 heterodimer experiments, dynein monomers (of which only one was previously labeled with a biotinylated dsDNA tether at the C-terminal HT) were dimerized with 200 nM rapamycin for 10min at room temperature before being diluted to the final concentration and mixed with streptavidin-coated beads. In tail-tethered GST homodimer experiments, dynein dimers were diluted to the final concentration and immediately mixed with either αGFP antibody-coated beads (when working with the GFP-GST-Dyn1$_{331kD}$-HT construct) or streptavidin-coated beads (when working with the biotinylated HT-GST-Dyn1$_{331kD}$ construct). The final concentration was determined experimentally for each prep such that no more than 35% of beads exhibited any activity when brought in contact with an axoneme, ensuring that >95% of observed events can be attributed to the actions of single motors[101]. Dynein was allowed to bind to the beads for 10 min at 4°C before proceeding with sample preparation. The sample chamber was loaded by first flowing Cy5-labeled axonemes in low-salt DLB buffer (30 mM HEPES, 2 mM MgCl2, 1 mM EDTA, 10% glycerol, pH 7.2), waiting 30 seconds for the axonemes to adsorb to the glass surface, then chasing with a solution of dynein-coated beads in motility buffer (assay DLB as specified above with the addition of 35 µg/mL PCD, 2.5 mM PCA, 10 mM DTT, and 1 mg/mL casein, and 1 mM ATP unless specified otherwise). The ends of the sample chamber were then sealed with nail polish to prevent liquid evaporation.

Optical trapping assay

All trapping experiments were performed on a fully automated optical trap, custom-built in an acoustically isolated and temperature-controlled (±0.1°C) room around the body of a Nikon Ti-E inverted microscope. Dynein-coated beads were trapped with a 2W 1064 nm laser (Coherent), tightly focused in the image plane with a 100X 1.49 N.A. apochromat oil-immerision objective (Nikon). The trap was steered with a pair of perpendicular acousto-optical deflectors (AOD's, AA Opto-Electronic), placed in a plane conjugate to the BFP of the objective. Power in the trap was controlled throughout the experiment with a half-wave plate on a motorized rotary mount (New Focus). Position of the bead relatively to the center of the trap was monitored using back-focal plane interferometry, by imaging the back-focal plane of a 1.4 N.A. oil-immersion condenser (Nikon) onto a position-sensitive detector (First Sensor, Inc.) Raw data from the detector were digitized by an NI 9215 analog input module (National Instruments), connected to an NI cRIO-9114 reconfigurable chassis (National Instruments). Signals were acquired and saved to disk at either 5 kHz or 20 kHz, and position feedback was performed at up to 200 Hz using the field-programmable gate array (FPGA) built into the cRIO-9114 chassis. Detector response was calibrated by rapidly raster-scanning the laser across a trapped bead with the AOD's and fitting the resulting curve to a cubic polynomial and trap stiffness was obtained from a Lorentzian fit to the power spectrum of a trapped bead [67].

The temporal resolution of optical trap data is fundamentally limited by the stiffness of the trap, as Brownian noise dominates the recordings at frequencies higher than the corner frequency of the Lorentzian power spectrum. The trap stiffness values used in this work resulted in corner frequencies of up to 400 Hz, corresponding to a temporal resolution of ~ 2.5 ms. Due to the compliance of the dynein motor and the motor-bead linkage, the smallest step size that could be reliably detected by our step-finding algorithm was ~2 nm. The accuracy of position and stiffness calibrations was independently verified by measuring the stall force of kinesin-1 to be 5.6 ± 0.8 pN, in good agreement with previously published values. Axoneme tracks, labeled with Cy5, were excited with a 633nm laser (Coherent), visualized with a monochrome camera (The Imaging Source), and brought to the center of the field of view with a locking XY stage (M-687, Physik Instrumente). The trapped bead was lowered to the surface of the axoneme by moving the trapping objective with a piezo flexure objective scanner (P-721 PIFOC, Physik Instrumente). Only beads that walked for at least 50 nm against the trap were subjected to force feedback and used for further analysis. To minimize noise,

the operator controlled the trap remotely throughout the experiment from an adjacent room through software custom-written in LabVIEW 2012 (National Instruments).

TIRF microscopy

Single-molecule motility assays were carried out on a custom-built objective-type TIRF setup, built around the body of a commercial Nikon Ti-E microscope[19]. Individual dyneins labeled with Cy5-tagged DNA tethers were excited with a 30 mW 633 nm laser (Coherent) and imaged with a 100X 1.49 N.A. apochromat oil-immersion objective (Nikon) onto an iXon EMCCD camera (Andor). Assay preparation was identical to the optical trap sample preparation described in a previous section, except without the addition of latex beads.

Data analysis

Position data were fit to steps using a fully automated, maximum likelihood-based step finding algorithm [102], implemented in Matlab. Because the algorithm assumes white noise with no autocorrelations, data were downsampled to approximately 50% of the corner frequency of the trap prior to fitting. Force-clamp runs that lasted shorter than 1 s, covered less than 50 nm, or included instantaneous jumps larger than 50 nm, were rejected from the analysis; otherwise the output of the step finding algorithm was accepted as is, without any further modifications. Motor velocities were determined by fitting individual runs with a straight line and calculating the slope of the line.

To generate dynein stall force histograms, position data from fixed-trap recordings were downsampled to 500 Hz for ease of visualization and stall events were manually selected. To qualify as a stall, the position trace had to reach a plateau and remain stationary (with mean deviations of less than $\pm$ 10nm) for at least half a second before terminating in a 'rip'. A 'rip', indicating that the motor fully released from the MT, had to constitute a rapid ($<$2 ms) jump of at least 50 nm, larger than the maximum step a dynein molecule can be expected to take. For, the definition of stall was the same except the minimum duration of the plateau at the top of the stall was decreased to 0.1 s, to account for kinesin's faster stepping rate and shorter near-stall dwells.

Force-velocity (F-V) curves were fit to the velocity expression for a one-state motor model[94], $V(F) = V_+ e^{-aFL/kT}\left(1 - e^{(\Delta G + FL)/kT}\right)$, where F is the external force, V_+ is the unloaded velocity due to forward stepping only, ΔG is the energetic bias provided by ATP hydrolysis, L is a characteristic distance, and *a* is a dimensionless parameter that defines the partitioning of load-dependence between the forward and backward stepping

rates. The net unloaded velocity V₀ can be expressed as $V_0 = V_+(1 - e^{\Delta G/kT})$. See Appendix for derivation.

FORCE GENERATION OF HUMAN CYTOPLASMIC DYNEIN

Introduction

In contrast to yeast dynein, which walks processively on its own and does not appear to behave differently in cells and in single-molecule experiments, previous studies on mammalian dynein revealed a striking mismatch between the motility of individual motors *in vitro* and their apparent *in vivo* functions. Despite high retrograde transport velocities observed in live cells[103–105], single purified mammalian dyneins exhibited diffusive motility or short processive runs *in vitro*[106–109] and were found to stall at forces of 0.5-1.5 pN[106,103,110,97,74,111], significantly weaker than the 6 pN force production of plus end-directed kinesin-1 motors[92]. It remained unclear how dynein motors generate the large forces required for their cellular roles, such as the transport of cargos against the pull of plus end-directed kinesins. It has been proposed that multiple (4-7) dynein motors need to be engaged in transport per kinesin-1 in order to balance forces during tug-of-war[41], and that the spatial organization of dyneins on the surface of the cargo (e.g. clustering on lipid microdomains) serves a fundamental regulatory role[112]. However, due to dynein's large size, it may not be sterically feasible for multiple dyneins motors to interact with a microtubule when transporting small cargos[113]. Furthermore, measured dynein to kinesin ratios (~1.5:1) on mouse axonal membranous vesicles [45] are inconsistent with the ~5:1 coupling predicted by force-based models.

Results

Recent studies with recombinant human dynein have begun to shed light on the mechanism of its motility. Both velocity and processivity of dynein are dramatically increased by the addition of dynactin, a multi-protein complex that associates with dynein *in vivo*, together with the N-terminus of the cargo activator Bicaudal-D2 (BICD2N), which increases the affinity of dynactin for dynein[33,32,114,115] **(Figure 11a-d)**. In single molecule motility experiments on sea urchin axonemes, we observed that free human dynein is poorly recruited to microtubules (0.19 fluorescent spots per micron length of axoneme per minute at 1 nM motor, N = 93) and only 16% of dynein spots exhibited slow (79 $\pm$ 11 nm s^{-1}, s.e.m., N = 15), processive motility in the absence of dynactin and BICD2N. The addition of dynactin and BICD2N increased the recruitment of dynein to microtubules by a factor of 3.5 (to 0.66 spots µm^{-1} min^{-1}, N = 98), with a substantially higher percentage (52%) of processively moving spots, resulting

in a tenfold increase in the number of walking molecules. The results are consistent with the enhancement of dynein recruitment and processivity in the presence of dynactin and BICD2N.

The autoinhibition of dynein may be mediated by a large-scale rearrangement of the tail domain, as is the case for some members of myosin[116] and kinesin[24] families, or by the back-to-back stacking of the motor domains. The tail-inactivation hypothesis has previously been rejected because attaching quantum dots (QDs) to human dynein's tail did not enhance its motility[106]. However, QDs are similar in size (~20 nm in diameter) to dynein itself, and it remained possible that attachment of larger cargos may have an impact on the motor's motility. To test this possibility, we attached a range of artificial cargos to dynein's tail and tested its motility *in vitro*. In agreement with Torisawa *et al.*[106], binding a QD to dynein tail did not increase dynein's velocity (**Figure 11e**). However, attachment of larger cargos to dynein's tail resulted in fast processive runs. Single dynein motors carried 200 nm diameter beads at 200 ± 23 nm/s (s.e.m., N = 21) in unloaded conditions (**Figure 11f**) and 860 nm diameter beads at 257 ± 26 nm/s (s.e.m., N = 83) under 0.4 pN constant hindering force (**Figure 11g**) [117], which was applied to allow for reliable detection of dynein unbinding from the microtubule. This ~4-fold increase in dynein's velocity indicates that release of dynein from the autoinhibited state can partially be stimulated by attachment of a large cargo to the tail domain. Importantly, the DDB complex moves ~2-fold faster than dyneins carrying a large bead (**Figure 11h**). Therefore, dynactin and BICD2 binding may lead to additional conformational changes of the heavy chains, such as alignment of the motor domains[118] and reorientation of the C-terminus[119], to further stimulate dynein motility.

We hypothesized that formation of the DDB complex may enhance the work output of the dynein motor. To test this possibility, we measured the force generation of dynein, dynein-dynactin, and the DDB complex using an optical trap. We sparsely attached recombinant human dynein motors containing an N-terminal GFP to micron-sized
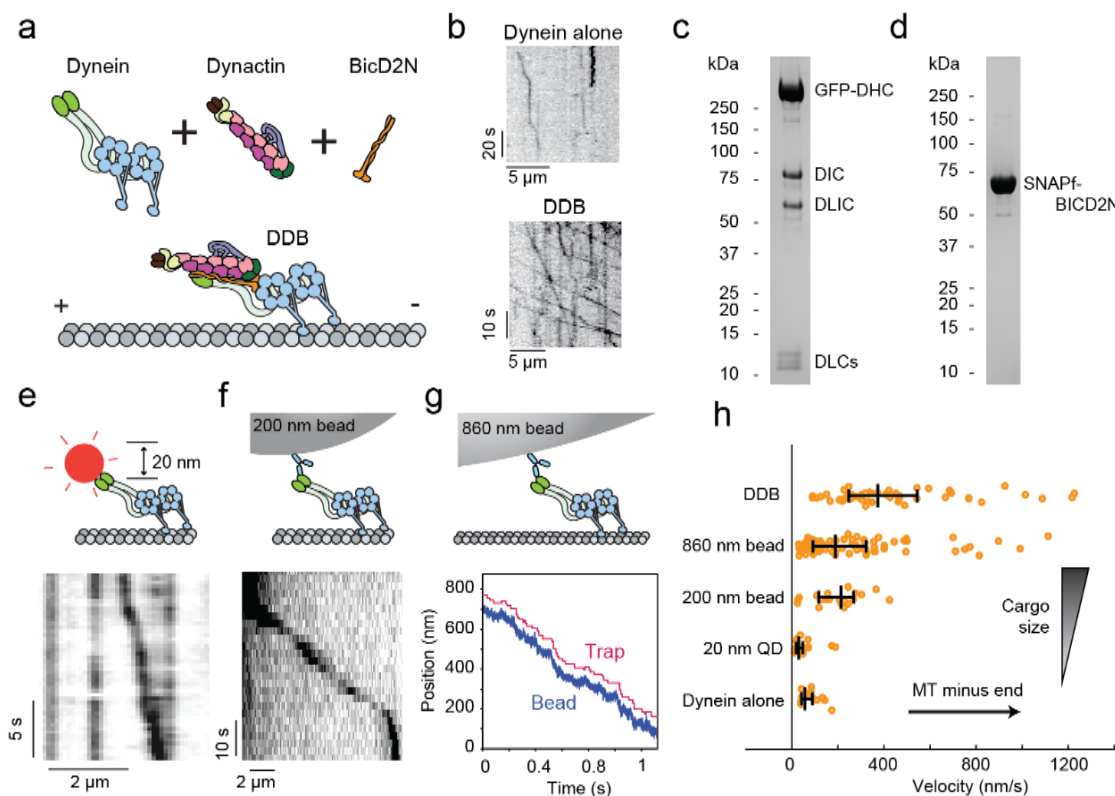
Figure 11. Activation of human dynein motility by dynactin, BICD2N, and artificial cargos. (a) Schematic depiction of the DDB complex on a microtubule. (b) Sample kymographs of dynein alone and DDB on axonemes. (c) Denaturing SDS–PAGE gel of purified dynein and (d) BicD2N fractions. Bands corresponding to all dynein subunits can be observed. (e) Illustration of dynein with a quantum dot attached to the tail (top) and sample kymograph (bottom). (f) Illustration of dynein with a 200 nm bead attached to the tail (top) and sample kymograph (bottom). (g) Illustration of dynein with an optically trapped 860 nm bead attached to the tail (top) and sample trajectory of dynein pulling the bead against a constant 0.4 pN force in force feedback mode (bottom). (h) Effect of cargo size and type on dynein velocity. N=51,83,21,19,15 in order from top to bottom.

polystyrene beads coated with αGFP antibody **(Figure 12a)**. With the trap held in a fixed position, the minus-end directed motility of beads driven by individual dynein motors stalled at 2.04 ± 0.02 pN (s.e.m.; N = 50) resistive forces. This is slightly higher than previously reported stall forces of human dynein $(0.5 - 1.5$ pN), but lower than the 3 pN stall forces of yeast cytoplasmic dynein[120]. Addition of dynactin at a five-fold molar excess caused only a modest (p = 0.0025, Welch's t-test) increase in stall force to $2.48 \pm$

0.06 pN (s.e.m.; N = 41) (**Figure 12b**), consistent with previous findings that dynactin alone has little effect on dynein motility[33,32].
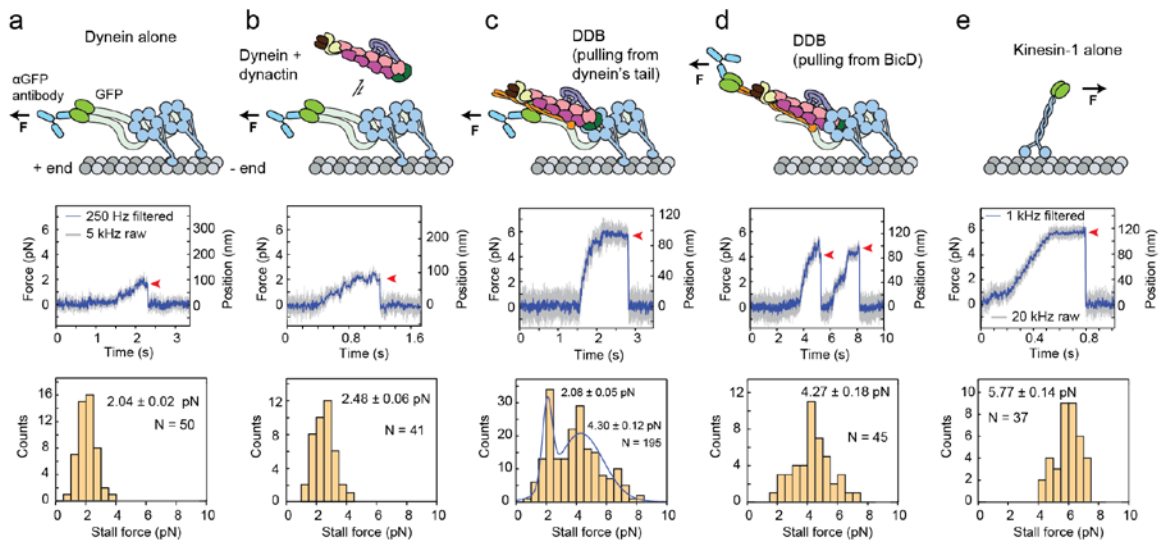

Figure 12. Effect of dynactin and BICD2N on dynein force production. (a) (Top) An optically trapped bead, represented with a force arrow, is attached to GFP on dynein's tail via an anti-GFP antibody. (Middle) Trace showing a typical stall of a dynein-driven bead in a fixed-trap assay. Red arrowhead represents the detachment of the motor from a microtubule after the stall. (Bottom) The histogram of observed stalls reveals the mean stall force (mean ± s.e.m., N = 50 stalls from 12 beads). (b) Stall force of dynein with the addition of 5x molar excess of dynactin (N = 41 stalls from 10 beads). (c) Stall force measurement of dynein with the addition of 5x molar excess of dynactin and 2x molar excess of BICD2N. Histogram of the observed stalls is fitted to two Gaussians (blue curve; N = 195 stalls from 47 beads). (d) Stall force measurement of dynein with the addition of 5x molar excess of dynactin and 2x molar excess of BICD2N, using BICD2N-GFP as the attachment point (N = 45 stalls from 14 beads). (e) Stall force measurement of kinesin-1 with a C-terminal GFP fusion as the attachment point (N = 37 stalls from 15 beads).

We next assembled the DDB complex at a 1:5:2 molar ratio of dynein:dynactin:BICD2N. Single-molecule motility assays showed robust processive motility at this ratio (**Figure 11b**). With all three components present, stall forces exhibited a bimodal distribution with a lower peak at 2.1 ± 0.3 pN, comprising 34% of all molecules, and a higher peak at 4.4 ± 0.5 pN, comprising 70% of all molecules (**Figure 12c, Figure 13**). It is likely that the lower peak at 2.1 pN corresponds to incomplete complex formation because in single-molecule motility assays, only 52% of GFP-tagged dynein motors move processively upon addition of dynactin and BICD2N

(see below). The stall forces near 4.4 pN only appear when all three components are present, suggesting that they correspond to the force output of DDB. To confirm this supposition, we measured the stall force of DDB by attaching the bead directly to BICD2N-GFP. In this assay, we used a dynein construct lacking the N-terminal GFP, ensuring that the αGFP antibody-coated beads only bind to BICD2N and that any observed motility should be driven by the DDB complex rather than dynein alone. The beads exhibited robust motility, stalling at 4.27 ± 0.18 pN (s.e.m.; N = 45) (**Figure 12d**), similar to the 4.4 pN peak observed in Figure 2c. A peak in stall events near 2.1 pN was not observed. Thus, we concluded that DDB complexes produce forces above 4 pN, higher than yeast cytoplasmic dynein (3.1 pN)[120] and close to human kinesin-1[92] (5.77 ± 0.14 pN, s.e.m.; N = 37) (**Figure 12e**).
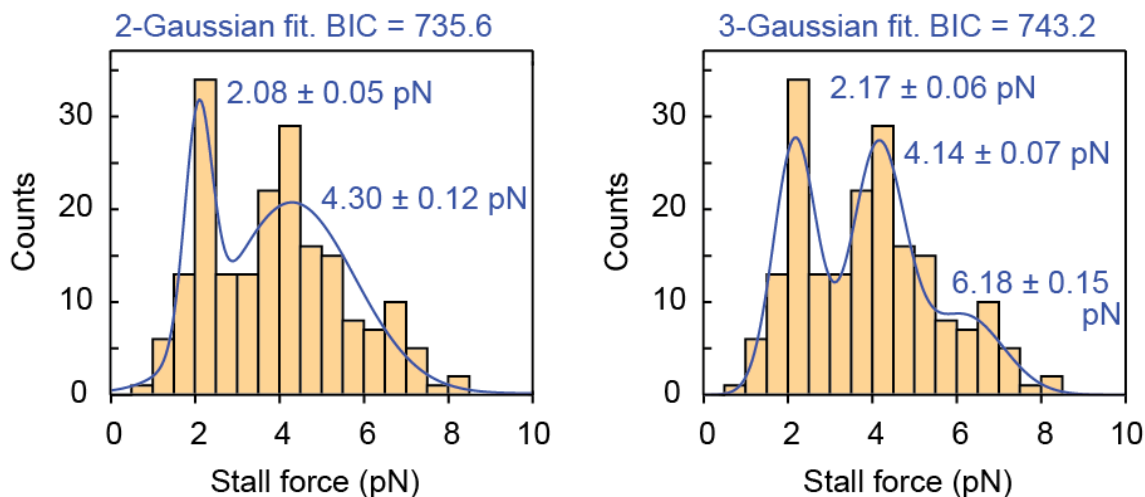

Figure 13. Comparison of 2-component and 3-component Gaussian mixture model fits to the DDB stall force distributions in Figure 12c. The fitting is carried out on the underlying distribution and is thus independent of the binning of the histogram. Blue curves are the scaled results of 2- and 3-component Gaussian fits, respectively. Numbers represent center values ± standard errors of each peak. The Bayes Information Criterion (BIC) is lower for the 2-Gaussian fit, indicating that adding a third Gaussian peak is not statistically warranted.

To rule out the possibility that multiple dynein motors aggregate in fluorescence or trapping assays, we performed a series of experiments to establish the single-molecule nature of each of our primary assays. First, we counted the number of photobleaching steps of microtubule-bound dynein dimers tagged with a single GFP on each monomer. 95% of the GFP spots bleached in either one or two steps in the presence and absence of

dynactin and BICD2N (**Figure 14a-b**), suggesting that they correspond to a single dynein dimer. In the trapping experiments, to prevent the possibility ofdynactin and BICD2N induced aggregation of dynein on the surface of beads, we pre-bound dynein sparsely to beads, removed the free motors, and then added dynactin and BICD2N (**Figure 14c**). Under these conditions, dynein still produced high stall forces, 4.0 ± 0.2 pN (s.e.m., N = 49), similar to the case in which all three components were mixed prior to bead binding (**Figure 14d**). Therefore, the measured increase in stall force of DDB is not an artifact of aggregation, but rather caused by the binding of dynactin and BICD2N to individual dynein motors. Finally, to ensure that trapped beads are driven by a single motor, we quantified the fraction of motile beads as a function of dynein concentration[101] (**Figure 14e**). All trapping experiments in this work were performed at a dynein concentrations at which > 97% of all beads were driven by single motors.

To investigate the effect of dynein activation by its adaptor proteins on the motor's ability to compete against its natural opponent, kinesin-1, we established an *in vitro* tug-of-war assay[50,121] allowing us to pit one dynein against one human kinesin-1. A dynein construct with an N-terminal SNAP tag was first labeled sub-stoichiometrically with a 74 nt long single-stranded DNA, and then with an excess of Alexa647 at its tail. This labeling strategy ensured that most dynein dimers were labeled either with one DNA molecule and one Alexa647 fluorophore, or two Alexa647 fluorophores. A similar strategy was used to label kinesin with a complementary DNA and a tetramethylrhodamine (TMR) at its tail using HaloTag (see **Methods**, **Figure 15a-c**). The labeled motors were linked to each other through DNA hybridization, and assayed for motility on microtubules polymerized from pig brain tubulin.

Simultaneous imaging of TMR-kinesin and Alexa647-dynein motors on microtubules revealed colocalization and correlated movement of dynein-kinesin complexes. By relying on sub-stoichiometric DNA labeling, we ensured that any observed colocalizers were comprised of one dynein and one kinesin motor. In the absence of dynactin and BICD2N, the velocities of colocalizers were nearly the same as those of kinesins alone (**Figure 15d,e**), revealing that dynein on its own is unable to resist kinesin's pull. However, the behavior of the colocalizers was markedly different upon the addition of dynactin and BICD2N. The median velocity of DDB-kinesin constructs (26 nm/s, N = 55) was reduced over 20-fold compared to that of dynein-kinesin (464 nm/s, N = 59) towards the microtubule plus end. Furthermore, 22% of DDB-kinesin colocalizers walked towards the microtubule minus end (N = 55; **Figure 15f,g, Figure 16**), which was not observed in the absence of dynactin and BICD2N. The velocity distribution of the colocalizers is distinct from those of both DDB alone and kinesin alone, indicating

that both motors are contributing to the overall motility rather than one being fully inactive and passively carried by the winning motor.

Next, we tested whether the dramatic slowing down and reversal of DDB motility can be explained by a purely mechanical response to kinesin's pulling force towards the plus end. Operating an optical trap in a force-feedback mode, we pulled single DDB complexes towards the plus-end with a force of 6 pN, corresponding to the reported stall force of kinesin-1 (**Figure 15h**)[92]. Under this condition, the median velocity of DDB was 10 nm/s towards the plus end, with 29% of the motors walking towards the minus end (**Figure 15f,h**; N = 35). These values are remarkably similar to the velocities of DDB-kinesin colocalizers, which is consistent with the predictions of the tug-of-war model.

Interestingly, we did not observe frequent reversals of a DDB-kinesin colocalizer's motility – the colocalizers that started walking towards the minus end continued to do so, and *vice versa*. This agrees with the absence of reversals in the artificial linking of multiple yeast dyneins to multiple human kinesins[50], and contrasts with the saltatory motility of organelles along microtubules *in vivo*. Reversals of cargo motility *in vivo* may result from the regulatory factors on the cargo that modulate motor activity, such as JIP1[122], or transient association of key regulatory proteins such as dynactin and BicD2N in cells[113]. The *in vitro* tug-of-war assay we developed will serve as a powerful platform for systematically identifying the effect of cargo adaptor proteins on motor tug-of-war.
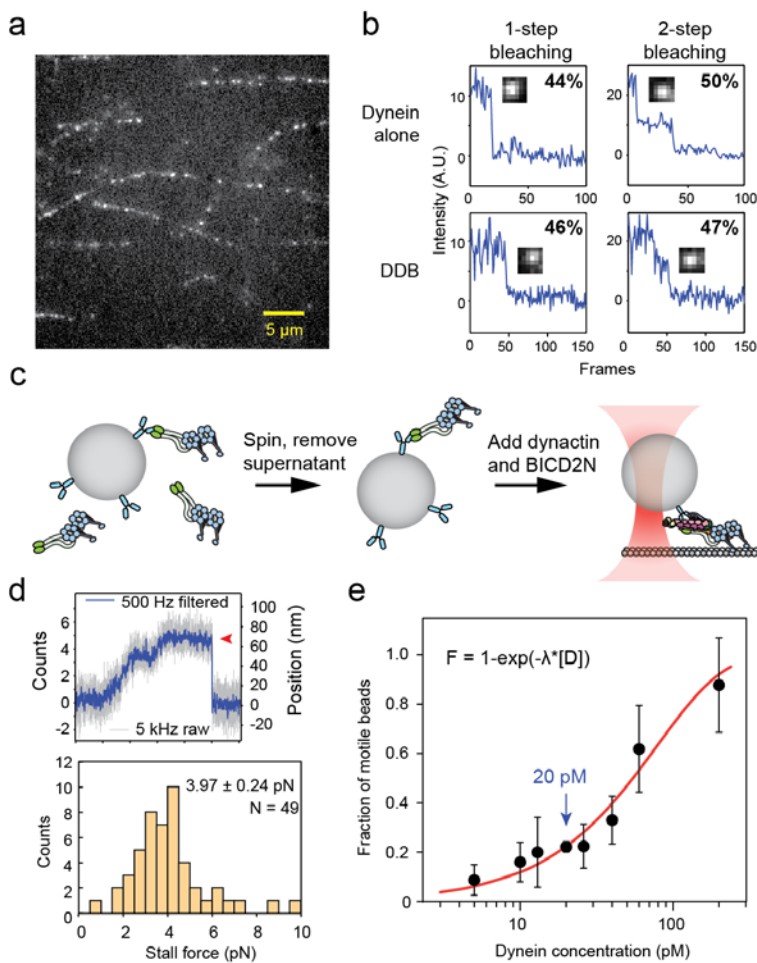
Figure 14. Processive motility of DDB complexes is driven by single dynein dimers. (a) Dynein-GFP molecules tightly bound to microtubules in the absence of ATP. (b) Intensity traces of dynein-GFP alone in the presence and absence of dynactin and BicD2 show one- and two-step photobleaching. Percent of total events is indicated for each case, with all remaining spots bleaching in three steps. N = 127 for dynein alone and N = 192 for DDB. The experiment was repeated 3 times with dynein from two independent preparations. (c) Schematic depiction of the modified sample preparation for optical trapping. Dynein is mixed with beads and excess dynein is removed by centrifugation. BICD2N and dynactin are added after the removal of free motors to rule out dynactin- and BicD2N-dependent aggregation of dynein motors on beads. (d) Representative stall trace of a DDB complex using the procedure shown in (c) and distribution of stall forces of the DDB complexes (N = 49). (e) Fraction of dynein-coated beads moving as a function of dynein concentration. Values are represented as the mean ± the square root of (F [1− F]/N), with N being the number of beads tested. For each data point, from left to right, N=23, 25, 10, 482, 28, 35, 20, 24. (e) Stall force measurement of kinesin-1 with a C-terminal GFP fusion as the attachment point (N = 37 stalls from 15 beads).
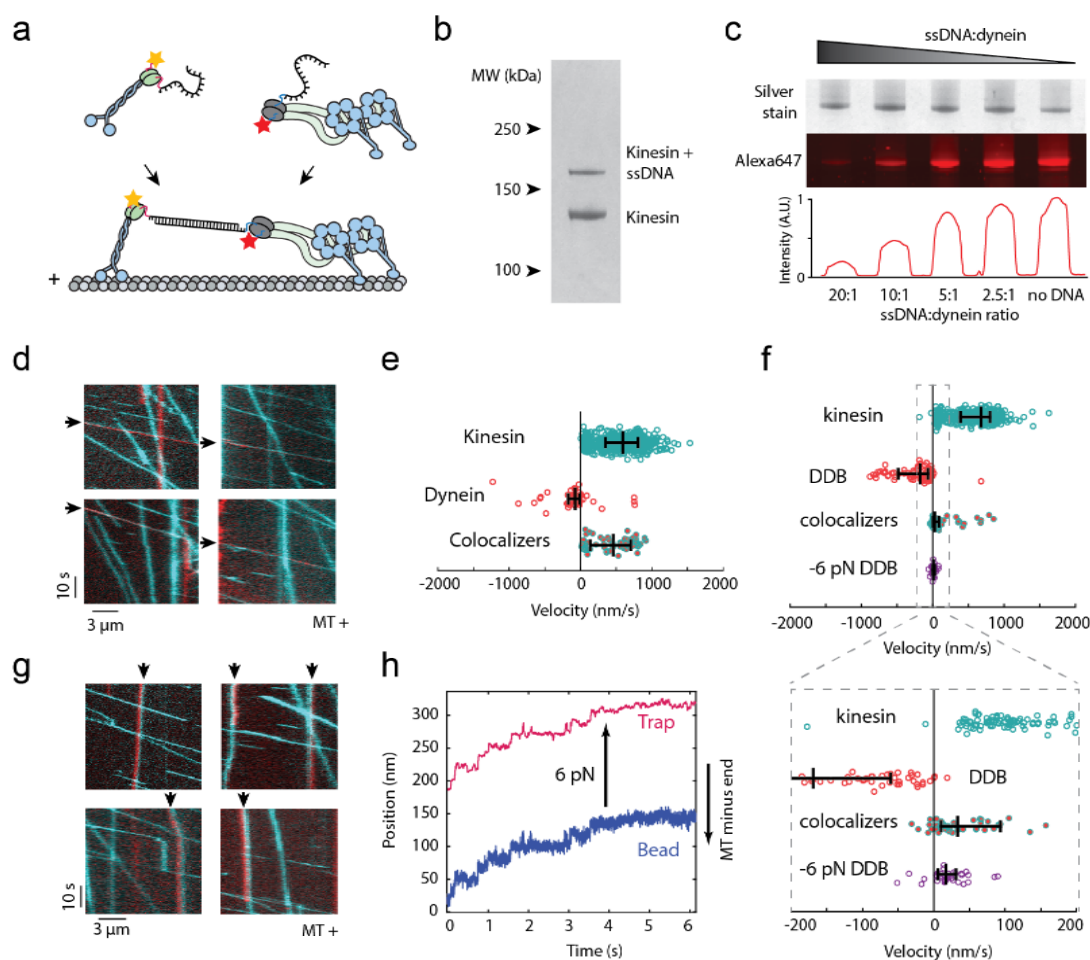
Figure 15. In vitro competition experiment between human dynein and human kinesin. (a) Kinesin-1 is labeled with a short DNA oligo and TMR, while dynein is separately labeled with a complementary oligo and Alexa647. The two motors are connected through DNA hybridization. (b) DNA labeling efficiency was estimated from the denaturing gel. (c) Dynein labeling efficiency quantified on an SDS-page gel by separately imaging total protein quantity and Alexa647 fluorescence. Higher DNA:dynein ratios resulting in lower Alexa647 fluorescence (bottom). (d) Kymographs of dynein-Alexa647 (red) and kinesin-TMR (cyan) motility in the absence of dynactin and BICD2N on microtubules. Colocalizers are identified with black arrows. (e) Velocity distribution of kinesin only, dynein only, and kinesin-dynein colocalizers. Positive values correspond to plus end-directed velocities. (f) Velocity distribution of kinesin only, DDB only, kinesin-DDB colocalizers, and DDB walking against a plus end-directed 6 pN force. (g) Kymographs of dynein and kinesin motility in the presence of dynactin and BICD2N. The black arrows indicate colocalizers. Colocalizers in the top row are walking towards the minus-end of the microtubule. (h) Representative trace of DDB slowly walking towards the plus end in response to a 6 pN pulling force exerted by the optical trap.
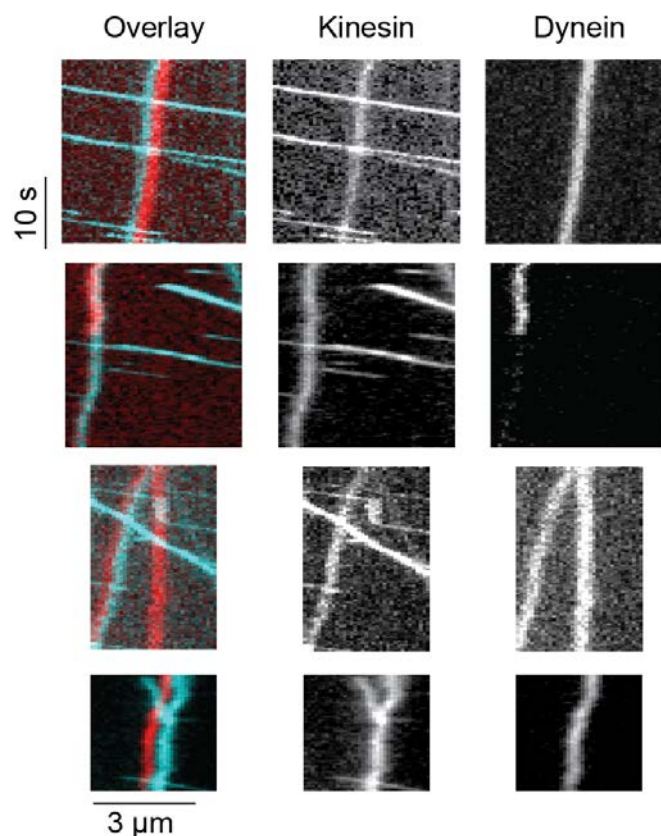
Figure 16. Examples of dynein-kinesin colocalizers in the presence of dynactin and BICD2N. Dynein is tagged with Alexa647 (red) and kinesin is tagged with TMR (cyan). Individual channels are shown in grayscale for clarity. All microtubules are arranged with the plus ends facing towards the right.

Discussion

Our results demonstrated that mammalian dynein complexes are strong motors capable of transporting cargos towards the microtubule minus-end against large resistive forces. Contrary to the earlier suggestion that 4-7 dyneins are needed to counteract the force production of a single kinesin-1[40], the activation of human dynein by dynactin and BICD2N allows it to dramatically slow down and sometimes defeat kinesin-1 in a one-to-one mechanical competition. A large force output of DDB is consistent with high minus end-directed forces exerted on lipid droplets in *Drosophila* embryos[123] and single phagosomes inside mouse macrophage cells[97]. Furthermore, formation of strong DDB complexes bypasses the previously postulated requirement for a highly ordered spatial

organization of dynein motors on the surface of cellular cargos. It remains to be seen how diverse cargo adapter proteins other than BicD2 affect the force production of the dynein/dynactin complex and regulate dynein's activity throughout the cell.

Optical trapping recordings *in vivo* have detected periodic peaks spaced at $1 - 2$ pN intervals in the force distributions of dynein-driven cargos. It has been proposed that the peak periodicity represents the force production of single[123] or a pair[97] of dynein motors, and that the larger collective forces originate from multiple (up to twelve) dyneins simultaneously engaging with the microtubule to transport the cargo. This model relies on the assumption that the measured peak forces in the retrograde direction represent the maximal force production of a single motor multiplied by the motor copy number[46]. Our results are not fully consistent with this simple mechanical model, because the stall force of single DDB complexes (4.3 pN) is significantly higher than the peak periodicity of these force distributions. We propose that the wide range of cargo stall forces measured during multiple motor transport *in vivo* can be affected by the modulation of kinesin and dynein activity by cargo adaptor proteins[77,124], premature release of the motors from microtubule before they come to a complete stall, and nonlinear mechanical coupling between multiple motors engaged with the cargo transport[125]. These possibilities remain to be rigorously tested by characterizing the force production of cargos containing predetermined numbers of motors and their regulators *in vitro*, such as the artificial cargos employed in this study.

Methods

Cloning and plasmid construction

Genes for DHC (DYNC1H1, accession number NM_001376.4), DIC (DYNC1I2, IC2C, AF134477), DLIC (DYNC1LI2, LIC2, NM_006141.2), Tctex (DYNLT1, Tctex1, NM_006519.2), LC8 (DYNLL1, LC8-1, NM_003746.2) and Robl (DYNLRB1, Robl1, NM_014183.3) were codon optimized for expression in Sf9 cells, synthesized commercially (Epoch Life Sciences) and assembled into a single plasmid as described previously[33]. Ligation independent infusion (Clontech) cloning was used to insert a GFP tag between the His-ZZ-LTLT tag[17] and the DHC gene. The mouse Bicd2 (NM_029791.4) gene was codon optimized for Sf9 expression and synthesized commercially (Epoch Life Science). The sequence coding for the N-terminal 400 amino acids was subcloned as described previously[33] and ligation independent infusion cloning

was used to insert a SNAPf tag (New England Biolabs) between the His-ZZ-LTLT tag[17] and the Bicd2 sequence.

Protein expression and purification

Dynein and BICD2N expression and purification using the baculovirus insect cell system was performed as described previously[33]. Briefly, constructs for either the full dynein complex or SNAPf-BICD2N were integrated into the EMBac or EMBacY baculovirus genome[126] and p2 baculovirus was produced. For protein expression 500 ml Sf9 cell suspension was infected with 5 ml p2 baculovirus and incubated at 27°C/124 rpm for 70-75 h. A ~2.5 g cell pellet was lysed using a tissue homogenizer (Wheaton), cleared by centrifugation and incubated with 2 to 5 ml IgG Sepharose 6 Fast Flow (GE Healthcare). The protein was removed from the beads with TEV protease and purified by size exclusion chromatography using either a G4000SW[XL] column (TOSOH Bioscience) or a Superose 6 column (GE Healthcare) on an Ettan LC system (GE Healthcare). The appropriate fractions were concentrated, snap frozen in liquid nitrogen and stored at -80°C. Dynactin was purified from pig brain using the large scale SP-Sepharose purification protocol[114]. Protein size and purity were confirmed by SDS-PAGE using Novex 4–12% Bis–Tris precast gels using either MOPS or MES buffer (Life Technologies) and stained with Instant Blue. Protein concentration was measured using the Quick Start Bradford kit (Bio-Rad).

Axonemes were extracted from live sea urchins as described previously[127]. Pig brain tubulin used for the assembly of microtubules was purified from fresh brains through two polymerization-depolymerization cycles in a high molarity buffer[128].

Functionalization of complementary DNA oligos

Two complementary amine-modified 74bp oligonucleotides (IDT) with the sequences /5AmMC12/TGGTCAATACTAGGAGCAGAGATGGCAGGAGTCAGATGAACAGA TAGTGGAGGCAGGGTCAGCGCGAGATCGTC (Strand 1) and /5AmMC12/ATGACGATCTCGCGCTGACCCTGCCTCCACTATCTGTTCATCTGA CTCCTGCCATCTCTGCTCCTAGTATTGAC (Strand 2) were designed to minimize potential secondary structures and contain a 2nt overhang on each end, followed by a 12-carbon spacer terminating with an amine group. 25 µM Strand 1 and 2 were separately labeled with 1.25 mM BG-GLA N-Hydroxysuccinimide (NHS) (New England BioLabs) and 1 mM alkyl chloride (AC) NHS, respectively, in a 50 mM HEPES pH 8.5 buffer containing 50% v/v DMSO. The reaction was allowed to proceed for 30 minutes

at room temperature, after which the DNA was de-salted and exchanged into dynein motility buffer (DMB: 30 mM HEPES, 5 mM $MgSO_4$, 1 mM EGTA, pH 7.0 with KOH) through five consecutive spins through 3,000 MWCO spin filters. DNA labeling was confirmed by gel electrophoresis using a 15% TBE-Urea gel, and the DNA concentration and purity were assessed by measuring A_{230}, A_{260}, and A_{280} absorbances.

Labeling dynein and kinesin with DNA oligos

SNAP-dynein was mixed with BG-GLA-Strand 1 and kinesin-HaloTag was mixed with AC-Strand 2 for 1h at 4°C. After the reaction, 10-fold molar excess of dye (BG-GLA-Alexa647 for dynein or AC-TMR for kinesin) was added to the reaction mixture for 15 minutes at 4°C to label remaining sites that were not labeled by DNA. The DNA labeling efficiency was highly sensitive to DNA and protein concentrations. In the case of kinesin, labeling efficiency was calculated by comparing the intensities of the labeled and unlabeled bands that were clearly separated on the 4–12% Bis–Tris SDS-PAGE gel (**Figure 15b**). For dynein, the labeled and unlabeled bands were virtually indistinguishable on the gel due to its high molecular weight. In this case, the labeling efficiency was estimated by running a band of dynein almost fully labeled with DNA that shows no Alexa647 fluorescence and a band of DNA-free dynein that is strongly fluorescent. The labeling efficiencies of the unknown dynein samples were estimated by comparing the relative Alexa647 fluorescence intensity of the band with that of ~100% labeled and 0% labeled control bands (**Figure 15c**). The DNA labeling ratio was optimized to yield a ~30% efficiency for both dynein and kinesin to minimize the likelihood of a single dimeric motor being labeled with two DNA strands to a <9%. Excess DNA and fluorophores were removed from both motors via microtubule bind and release (MTBR).

MTBR purification of human dynein

Human dynein was purified and separated from DNA and Alexa647 using a modification of the MTBR protocol previously established for yeast dynein[120]. First, ~200 nM dynein was mixed with 2 mg/mL microtubules and allowed to bind at room temperature for 10 min (typical reaction volume was ~300 µL). Then, the dynein/microtubule mixture was centrifuged through 200 µL of sucrose cushion (25% sucrose and 100 µM taxol in DMB buffer: 30 mM HEPES, 5 mM MgSO4, 1 mM EGTA, pH 7.0 with KOH) for 10 min at 22°C and 40,000 rpm in a TLA 120.1 rotor (Beckman Coulter). The pellet was washed twice with DMB supplemented with 100 µM taxol and 1 mM DTT, then resuspended in half of dynein's original volume of release buffer (DMB supplemented with 150 mM

KCl, 2 mM ATP, and 1 mM DTT) and allowed to release at room temperature for 10 min. The solution was then centrifuged for 10 min at 22°C and 40,000 rpm to remove microtubules from free dynein. The supernatant was supplemented with 20% v/w glycerol and stored at -80°C.

Coating beads and quantum dots with αGFP antibodies

860 nm and 200 nm carboxyl latex beads (Life Technologies) were coated with custom-made rabbit polyclonal αGFP antibodies (Covance) with EDC and sulfo-NHS crosslinking (Pierce). 100 µL of 4% v/w bead stock were mixed with ~1 mg of antibody in coupling buffer (100 mM sodium-phosphate buffer, pH 7.4), per) and reacted with shaking at room temperature for 30 min. The labeled beads were then passivated by adding 10 mg/mL BSA and stored in 1x PBS (Phosphate Buffered Saline, pH 7.4) supplemented with 0.1% sodium azide and 0.5 mg/mL BSA at 4°C.

Amine-coated quantum dots emitting at 585 nm (QD585; Invitrogen) were labeled with the same rabbit polyclonal αGFP antibodies (Covance) via sulfo-SMCC crosslinking (Pierce). QD585 were dissolved in 100 mM pH 8.0 borate buffer to a 200 nM final concentration and incubated with a 250 fold excess of sulfo-SMCC for 1 h. Excess crosslinker was removed by two runs through a 30,000 MWCO spin filter and QD585 were transferred into dynein motility buffer (DMB: 30 mM HEPES, 5 mM $MgSO_4$, 1 mM EGTA, pH 7.0 with KOH). Antibodies were reduced with 2 mM DTT for 30 min and residual DTT was removed by three runs through 7,000 MWCO spin de-salting columns. Activated QD585s were then incubated with a 4-fold molar excess of the reduced antibodies for 1 h. The reaction was quenched with the addition of 20 mM Tris pH 8.0 and spin-concentrated to obtain the desired final concentration.

Optical trap assay

Dynein concentration was determined for each batch of protein. The protein was diluted until less than 30% of beads exhibited any activity when brought in contact with an axoneme, ensuring that >95% of observed events can be attributed to the actions of single motors. When BICD2N and/or dynactin were added to the assay, they were mixed with dynein at 1:5:2 molar ratio (dynein:dynactin:BICD2N) and incubated at 4°C for 5 minutes prior to adding the complex to beads. Dynein with any auxiliary proteins was then allowed to bind to 860 nm diameter latex beads for 10 min at 4°C before proceeding with sample preparation. The sample chamber was loaded by first flowing Cy5-labeled axonemes in dynein motility buffer (DMB: 30 mM HEPES, 5 mM $MgSO_4$, 1

mM EGTA, pH 7.0 with KOH), followed by a solution of dynein- or DDB-coated beads in motility/imaging buffer (DMB supplemented with 35 µg/mL PCD, 2.5 mM PCA, 10 mM DTT, 1 mg/mL casein, and 2 mM ATP). All trapping experiments were performed as described in the previous chapter.

Motility and photobleaching assays

Single-molecule motility assays were carried out on a custom-built objective-type TIRF setup, built around the body of a commercial Nikon Ti-E microscope. Fluorophores were visualized with a 100X 1.49 N.A. apochromat oil-immersion objective (Nikon) and imaged onto an EMCCD camera (Andor). Assay preparation was identical to the optical trap sample preparation described in a previous section, except without the addition of latex beads. In the dynein-kinesin crosslinking motility experiments, dynein-DNA and kinesin-DNA were allowed to react with each other for 10 min at 4°C prior to being diluted to the final desired concentration. Photobleaching experiments were performed without the addition of ATP to ensure that motors remain stationary on axonemes. >95% of spots bleached completely over the course of a 200-frame movie.

For dynein-driven bead motility experiments, 200 nm latex beads coated with GFP antibodies were sparsely decorated with dynein (with or without dynactin and BICD2N) and imaged with either brightfield illumination or scattered-light fluorescence. To ensure single-molecule conditions, the concentration of dynein was reduced until >90% of beads did not visibly interact with axonemes upon contact. The trap was used to measure the velocity of individual dynein motors carrying 860 nm diameter beads, because these beads are too large to encounter microtubules with sufficient frequency by diffusion alone.

The dynein-kinesin colocalization motility experiments were performed on microtubules prepared from purified pig brain tubulin rather than sea urchin axonemes. We observed that switching from axonemes to microtubules had a modest effect on dynein recruitment to the tracks and initiation of motility, but not on its velocity or processivity following recruitment. Microtubules were used for the colocalization experiments mainly to obtain better control over the length of the tracks. For surface immobilization, 1% of biotinylated tubulin was incorporated into the microtubule and the coverslip was pre-coated with streptavidin and BSA.

Data analysis

In order to extract run velocities from fluorescence movies, kymographs were created along each individual axoneme using ImageJ. Motile dynein motors were then identified manually from the kymographs. Only molecules that traveled > 530 nm (5 pixels along x) and remained bound for more than 2.5 s (5 pixels along y) were included in the analysis. Diffusive molecules (those that exhibited >530 nm excursions in both directions along the axoneme) were excluded. For molecules that transitioned from static behavior (>30 seconds with < 100 nm displacement) to motile behavior, only the motile segments were analyzed.

To generate dynein stall force histograms, position data from trap recordings were downsampled to 250 Hz or 500 Hz for ease of visualization and stall events were manually selected. To qualify as a stall, the position trace had to reach a plateau and remain stationary (with mean deviations of less than $\pm$ 10nm) for at least 100 ms before terminating in a 'rip'. A 'rip', indicating that the motor fully released from the microtubule, had to constitute a rapid (<2 ms) jump towards the trap center of at least 50 nm, larger than the maximum step a dynein molecule can be expected to take. Histograms were fitted with either a single Gaussian peak or two Gaussian peaks of equal width. To independently confirm our ability to accurately detect stalls, we measured the stall force of kinesin-1 to be 5.6 ± 0.2 pN, in good agreement with previously published values. Image analysis was performed in ImageJ.

PHOTOGATE METHOD FOR SINGLE MOLECULE TRACKING

Introduction

Single-particle tracking (SPT) avoids ensemble averaging and allows the stochasticity and heterogeneity of molecular behavior to be observed directly in real time. Performing these experiments in live cells has been a challenging task because of the crowded nature of cellular environments, the short time scales of molecular dynamics, and the lack of appropriate microscopy tools. In conventional microscopy, molecules closer to each other than the diffraction limit (~250 nm for visible light)[6] cannot be readily resolved due to the overlap of their point spread functions. Therefore, the concentration limit for single molecule detection is ~1 nM, which corresponds to a few molecules in an entire *E. coli* cell. Molecules separated by less than the diffraction limit can be resolved using stochastic photoactivation[129,130], structured illumination[131] and stimulated emission depletion[132]. However, breaking the diffraction limit comes at the expense of lower temporal resolution either through image scanning[132] or super-positioning of multiple frames[129–131], which make these techniques unsuitable for monitoring rapid dynamic processes.

Photobleaching and photoactivation of fluorescent probes are often used to study the dynamics of molecules inside cell. Single particle tracking photoactivation light microscopy (sptPALM) overcomes the concentration limit for SPT by photoconverting a small subset of 'dark' molecules at a time[133]. While this method achieves high frame rates, it only yields very short trajectories (typically <20 frames)[134] because of the low photon budget of photoconvertible probes[135]. Photobleaching is often used to reduce the apparent concentration of fluorophores[136] and to observe the dynamics of molecules inside cells by monitoring fluorescence recovery after photobleaching (FRAP)[137]. Because the fluorescent particles arrive in a continuous stream from the unbleached region in FRAP assays, single particles can be resolved only at the very onset of the recovery process and effective SPT time is limited by fluorophore density and the fluorescence recovery rate[138]. This rapid recovery makes FRAP-based approaches ill-suited for observing dynamic interactions between individual proteins and large cellular structures, such as organelles and cytoskeleton.

In this study, we developed PhotoGate to track single particles in dense specimens for extended periods of time. The method selectively photobleaches fluorescent particles and controls the number of fluorophores that enter the region of interest (ROI). Unlike FRAP, new fluorescent particles streaming into the ROI are repeatedly photobleached at its boundary by a gate beam and the density of fluorophores in the ROI remains at a constant low level. Therefore, PhotoGate bypasses the need for photoactivation and substoichiometric labeling, and achieves SPT of conventional probes until photobleaching at concentrations two orders of magnitude higher than the diffraction limit. Using this method, we detected arrival and departure events of single APPL1 molecules on the surface of early endosomes, and the monomer-to-dimer transition of EGFR receptors in response to a signaling cue on a mammalian cell membrane.

Results

The PhotoGate Assay

PhotoGate utilizes two separate laser beams of the same excitation wavelength and orthogonal polarization **(Figure 18)**. The first laser beam, referred to as the gate beam, is focused in the image plane and swept outwards from the center in a spiral pattern to pre-bleach a circular region of interest (ROI) **(Figure 17a)**. The gate beam is then shuttered for several seconds to allow a small number of unbleached molecules to diffuse into the ROI. The second beam, referred to as an imaging beam, is used to image fluorescent molecules in the ROI at a high signal-to-noise ratio (SNR) under total internal reflection (TIR) illumination. To prevent additional fluorescent molecules from diffusing into the ROI during imaging, the gate beam is repeatedly swept along the outer perimeter of the ROI. As a result, the density of fluorescent objects in the ROI remains low and does not increase over time.

We found that sweeping a 15-µm diameter area with a focused gate beam ($10 \ \mathrm{MW/cm^2}$, 1 µm full width half-maximum (FWHM)) in 10 s was sufficient to photobleach nearly all of the fluorescent molecules in the ROI (**Figure 17**). During pre-bleaching, the background fluorescence in the ROI was greatly reduced without significantly (<20%) photobleaching the molecules outside the ROI. The diameter of the imaging beam

matches that of the pre-bleached ROI to prevent useless bleaching of the fluorescent molecules outside the ROI.
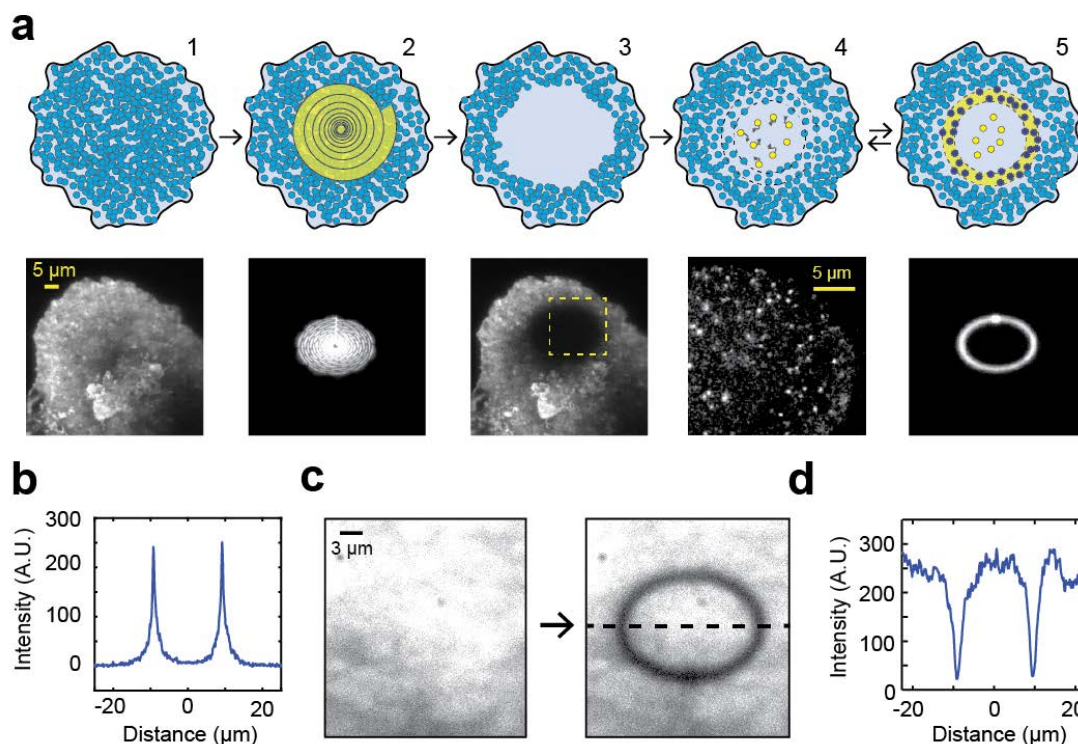

Figure 17. PhotoGate Imaging for Single Particle Tracking. (a) 2D PhotoGate schematic (top row) with corresponding representative images (bottom row). 1) A cell surface is heavily decorated with fluorescently labeled molecules (blue circles). 2-3) The focused gate beam is swept outwards from the center in a spiral pattern to pre-bleach an elliptical region. 4) The gate beam is turned off to allow diffusion of fluorescent molecules from the periphery of the ROI, which are then imaged under TIRF illumination (yellow circles). 5) The gate beam is repeatedly turned on to photobleach fluorescent particles entering the ROI (dark blue circles) while single molecules inside the ROI are imaged under TIRF illumination. Photobleached particles are not shown for clarity. (b) Linear intensity profile along a line bisecting the PhotoGate ring shown in panel 5 of (a). (c) A coverslip densely coated with GFP is bleached with a single sweep of the PhotoGate ring to demonstrate the bleaching profile (d) The bleaching profile plotted along the yellow dashed line in (c). (e) Sample intensity trace from a single diffusing mNeonGreen spot tracked using PhotoGate.
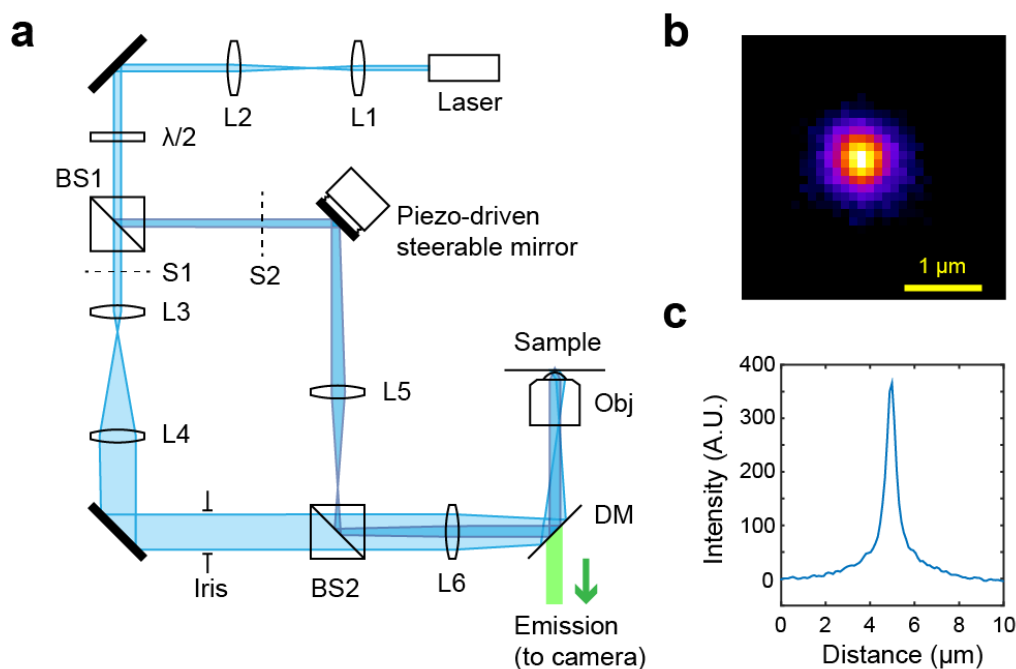
Figure 18. Two Dimensional PhotoGate Assay Achieved by Steering of a Focused Laser Beam. (a) Optical diagram of the steerable 2D photogate microscope. The beam exiting the laser is expanded to a ~3 mm diameter and collimated using a 3:1 telescope (lenses L1 and L2). The beam then passes through a half-wave plate ($\lambda/2$) mounted on a rotary stage, which allows us to control the relative amount of power going into the photogate and the TIRF beam. The polarized beam-splitter cube BS1 splits the beam into the TIRF and photogate components, which can be shuttered independently of each other by shutters S1 and S2. The TIRF beam is further expanded by a 5:1 telescope (L3 and L4) and focused onto the back-focal plane (BFP) of the objective by the TIRF lens L6. The diameter of the TIRF beam can be altered with a variable-diameter iris conjugate to the image plane. Meanwhile, the photogate beam is steered by the piezo-driven mirror and relayed onto the BFP of the objective by the 4:3 telescope made by lenses L5 and L6. Fluorescence emission from the sample passes through the dichroic mirror DM and is collected by an EMCCD camera. (b) Fluorescence image and (c) 1D intensity profile of the focused laser beam.

Measuring APPL1 residence times on early endosomes

PhotoGate is uniquely suited for observing the dynamic interactions of concentrated and rapidly diffusing molecules with relatively immobile structures such as large organelles in a cytoplasm. To demonstrate this class of applications, we used PhotoGate to measure the single-molecule residence times of APPL1, a mediator of intracellular

epidermal growth factor receptor (EGFR) signaling, on the surface of endosomes. APPL1 transiently localizes to a subset of vesicles created by clathrin-mediated endocytosis or micropinocytosis, and marks early endosomes prior to their conversion to the PI3P stage[139]. It is unclear whether APPL1 binds tightly to its target vesicles and only dissociates after receiving a specific signaling clue, or the bound and unbound populations remain in dynamic equilibrium.
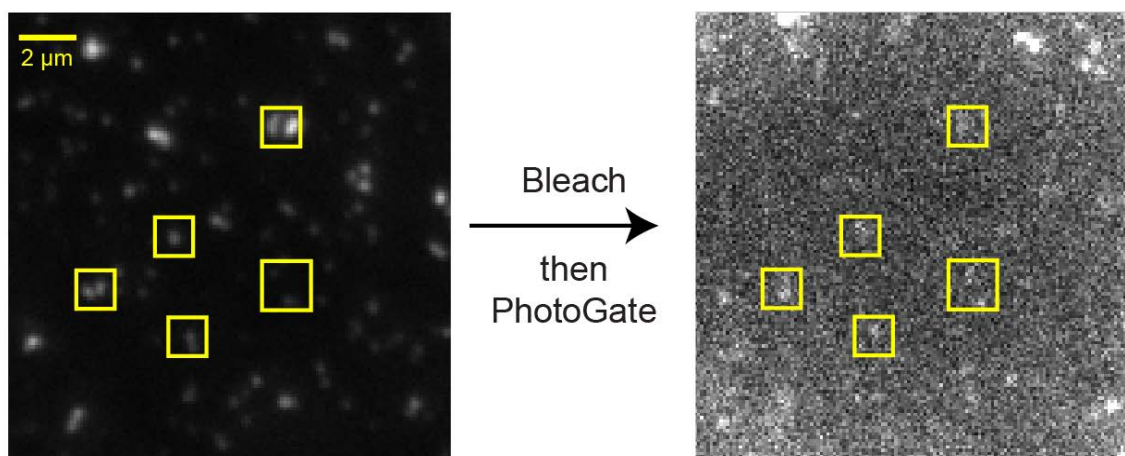

Figure 19. Correlation between known endosome positions prior to bleaching and the appearance of single-molecule APPL1 spots in PhotoGate. Because endosomes are relatively immobile in nocodazole-treated cells, observing the location of single spots in the PhotoGate experiment allows one to determine whether these spots correspond to APPL1 molecules specifically associating with endosomes or are random sticking events. Nearly every single-molecule spot appears at a previously known endosome location.

To detect the arrival and departure events of individual APPL1 molecules at early endosomes, we transiently transfected human U2OS osteosarcoma cells with a GFP fusion of APPL1. The cells appeared bright with background fluorescence, with endosomes visible as even brighter spots (**Figure 20**). Cells were pretreated with nocodazole (see **Methods**) to immobilize the endosomes and to confirm that the observed single-molecule arrival and departure events are spatially correlated with the last known endosome positions (**Figure 19**). The high concentration of APPL1 both in the cytoplasm and on the surface of endocytic vesicles makes it impossible to observe its

dynamics using conventional TIRF imaging. We first performed FRAP by fully bleaching a 17 µm diameter ROI and imaging the recovery of fluorescence until steady state was reached under TIRF illumination (**Figure 20d**). During recovery, density of APPL1 at individual endosomes almost immediately exceeded the single-molecule detection limit, making FRAP-based approaches unsuitable for SPT of APPL1. The half-time of recovery at endosomes was found to be 24.7 $\pm$ 4.5 s (s.e.m., **Figure 20e**). Interestingly, the half-time of recovery in an endosome-free region was only slightly lower than at endosomes, 21.3 $\pm$ 2.7 s (s.e.m., **Figure 20e**), suggesting that the recovery is diffusion-limited. FRAP yields little information about the reaction rates of APPL1 at endosomes, because it cannot independently measure the diffusion and reaction components[140].

PhotoGate bypasses this issue by directly measuring the dissociation of single APPL1 molecules from endosomes and eliminating the signal of rapidly diffusing molecules in cytoplasm. We bleached a 15 µM diameter ROI in the same way as in the FRAP experiment, followed by periodic sweeping the gate beam around the perimeter of the ROI every 2 seconds. The gate beam bleached the majority of fluorescent APPL1 molecules entering the ROI (**Figure 20**), because fluorescence levels remained constantly low while the gate was on and fully recovered within tens of seconds when the gate was turned off. The ROI was imaged under TIR illumination at 2 frames per second (a time-lapse imaging protocol consisting of 50 ms exposure followed by 450 ms dark time). We detected single fluorescent spots appear at and dissociate from the pre-bleached endosomes (**Figure 20a**). The residence time distribution of individual molecules (**Figure 20f**) revealed that the mean APPL1 off-rate is 0.12 s^{-1} (0.09 to 0.14 s^{-1}, 95% conf. int.). Interestingly, this is several fold faster than the FRAP recovery rate, further illustrating that FRAP data is often a convolution of multiple distinct processes that cannot be easily untangled.
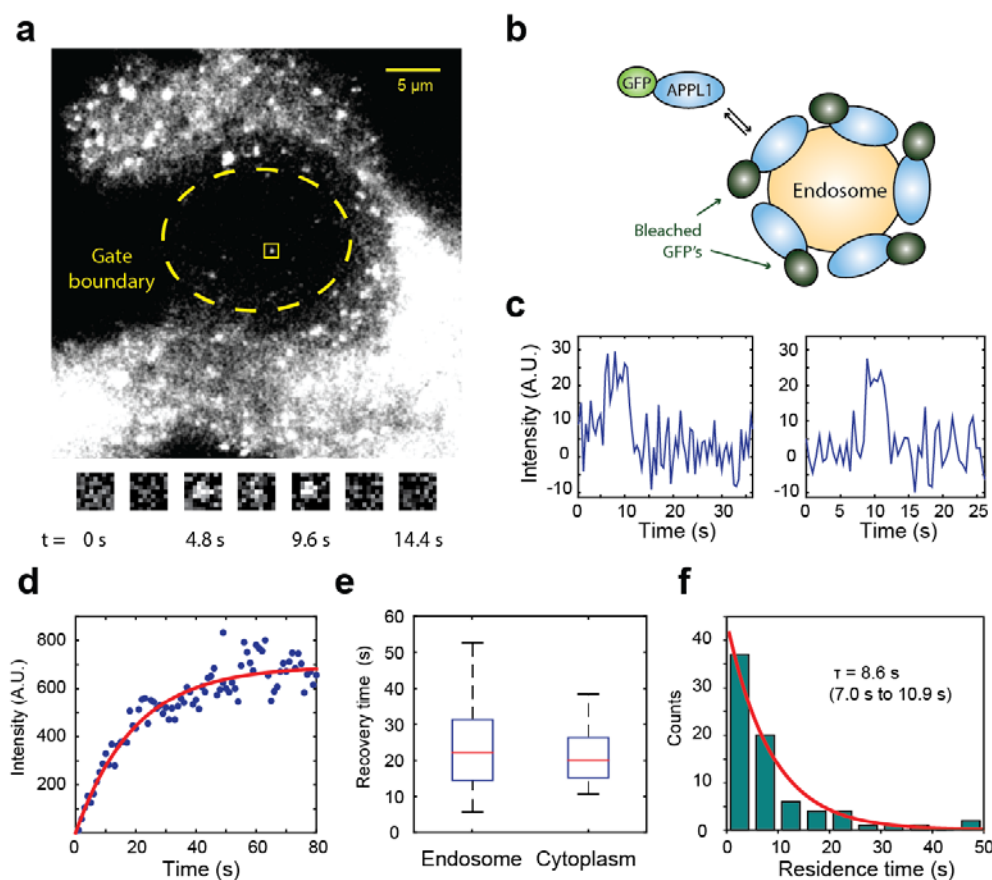
Figure 20. Measuring APPL1 residence times on early endosomes. (a) TIR image of a cell expressing APPL1-GFP in the middle of a PhotoGate experiment. Below: enlarged snap shots at different time points of the fluorescent spot marked with a yellow square. (b) A model for the exchange of fluorescent APPL1-GFP with bleached APPL1 molecules on an endosome. (c) Fluorescence intensity trajectories of single spots inside the ROI reveal the arrivals and departures of single APPL1 molecules. (d) A typical FRAP curve, measured at a single endosome after bleaching a 10 µm diameter region. Fluorescence intensity rapidly becomes too high to detect single molecules. (e) FRAP recovery times, measured at endosomes and endosome-free regions of the cytoplasm. N = 10 cells for each condition. (f) Residence times of single APPL1 molecules are fitted with a single exponential decay model to obtain the off rate.

To rule out the possibility that the observed disappearances of APPL1-GFP spots were a result of photobleaching rather than physical dissociation of APPL1 from endosomes, we repeated the experiment by keeping the exposure time constant at 50 ms and adjusting the dark time to alter the frame time to 150 ms and 1500 ms. Had the observed 'departure' events been caused by photobleaching, the measured residence

times would depend primarily on the number of collected frames under the same TIRF excitation power. In contrast, we observed residence times to remain nearly independent of frame rate (**Figure 21**), demonstrating that they correspond to departures of APPL1-GFP from endosomes. These measurements suggest that the short-lived, dynamic association of single APPL1 proteins with the endosomal surface may enable the rapid and highly coordinated displacement of the entire APPL1 population as the endosome transitions to the PI3P-positive stage.
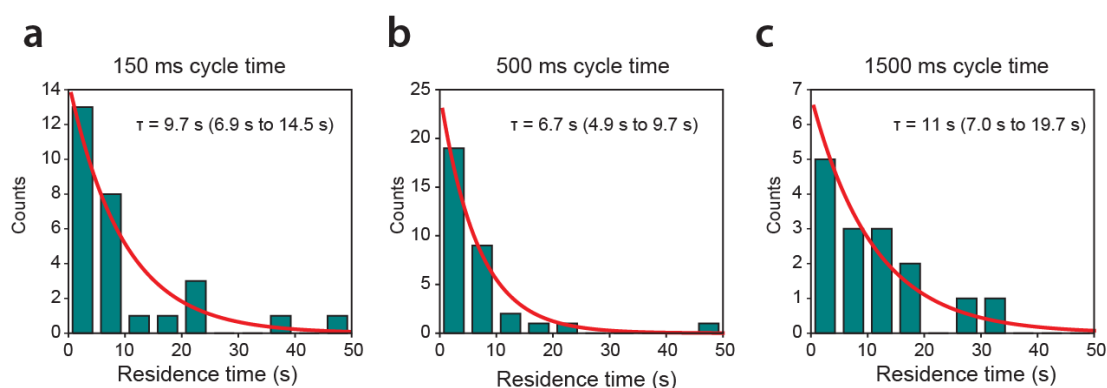

Figure 21. Dissociation time constants of single APPL1 molecules from endosomes measured at different kinetic cycle rates. Identical experiment to that shown in **Figure 20f**, except for a variation in total kinetic cycle time. In each data set, the exposure was fixed at 50 ms per frame, and the 'dark' time was altered to achieve the desired cycle time (100 ms 'dark' time in **a**, 450 ms in **b**, and 1450 in **c**).

Tracking EGFR Diffusion on a Mammalian Cell Membrane

We next applied PhotoGate to reveal the dynamics of single receptor complexes on a live cell membrane. EGFR is a prototype of receptor tyrosine kinases[141], comprising an extracellular ligand-binding domain, a single transmembrane helix and an intracellular tyrosine kinase domain **(Figure 22a)**. Binding of epidermal growth factor (EGF) to the extracellular domains promotes the formation of an asymmetric dimer of intracellular kinase domains, one of which allosterically activates the other[142] and triggers the recruitment of the downstream signaling proteins. In fluorescence microscopy studies, ligand-induced dimerization was inferred indirectly from the differences in the diffusion

constants between ligand-bound[143,144] and ligand-free[141,145] receptors. In these studies, labeling densities were kept several orders of magnitude lower than the actual receptor densities on the cell membrane, which are too crowded for SPT. Therefore, majority of the receptor molecules remained unlabeled and the oligomeric state of EGFR molecules could not be directly determined by subunit counting.

We expressed the mNeonGreen-fusion of EGFR in monkey fibroblast (COS7) cells. Because the cell membrane was densely covered with mNeonGreen-EGFR (400 molecules/µm^2), it was not possible to track individual molecules by conventional TIRF imaging **(Figure 22b),** even during the onset of the fluorescence recovery process in FRAP assays **(Figure 22c)**. Using FRAP, the recovery of the EGFR fluorescence into a 4 µm diameter ROI on a cell membrane was recorded at 100 ms temporal resolution **(Figure 22c)**. The fluorescence recovery analysis revealed that the average diffusion constant of EGFR was 0.22 ± 0.02 µm^2/s in serum-starved conditions **(Figure 22d)**.

Using PhotoGate, we simultaneously determined diffusion constants and stoichiometry of individual EGFR complexes in real time. Initially, a 15-µm diameter ROI was pre-bleached by sweeping the focused gate beam, followed by a 2 s dark waiting period to allow a few fluorescent molecules to diffuse into the ROI. After pre-bleaching, single mNeonGreen spots were tracked at a rate of 20 frames per second with an imaging beam without inducing harmful effects to living cells. Imaging was interspersed by 200 ms-long sweeps of the gate beam around the outer perimeter of the ROI. On average, ~47,000 photons were detected from one mNeonGreen until photobleaching **(Figure 22f)**[146]. The mean tracking lifetime (τ) of single mNeonGreen-EGFR was 10.1 ± 1.2 s. During SPT, fluorescent molecules outside the ROI remain unbleached because they are not subjected to TIRF illumination.
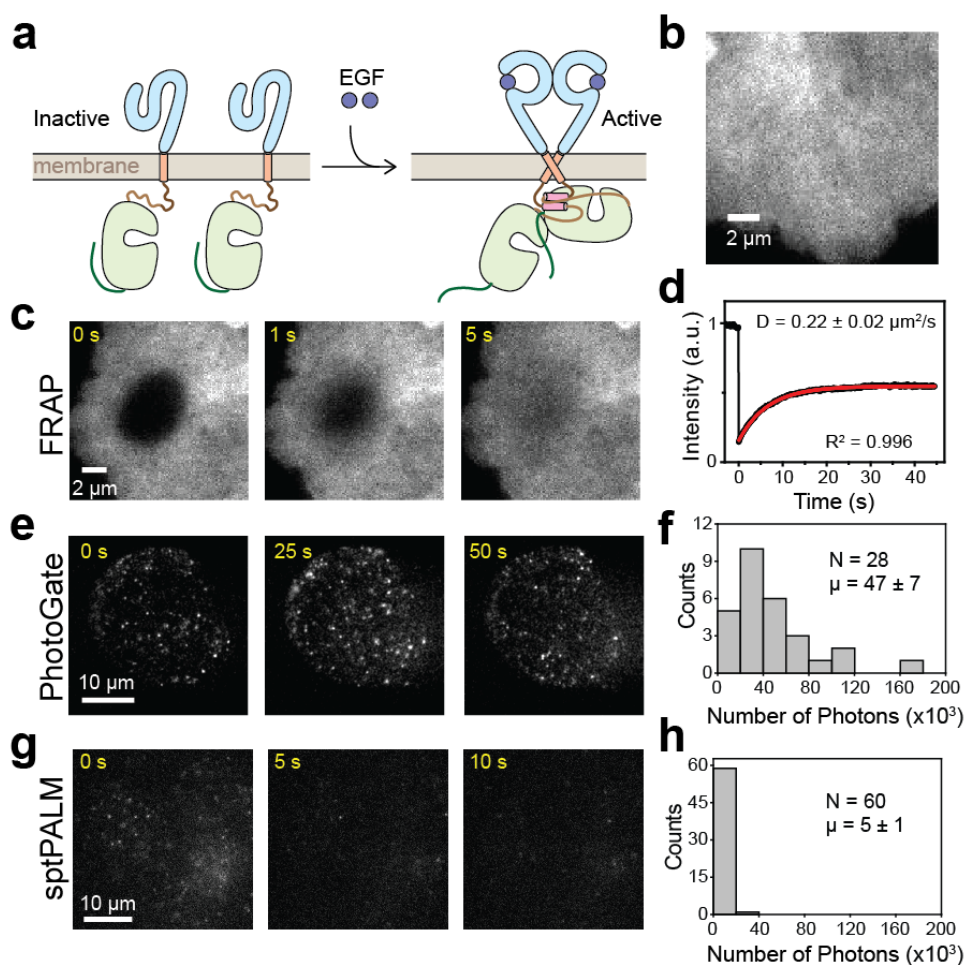
Figure 22. Tracking of single EGFR molecules in a live cell membrane. (a) A model for the ligand-induced dimerization of EGFR. EGFR monomer contains an extracellular ligand-binding region (blue), a single transmembrane helix, an intracellular tyrosine kinase domain (light yellow) and a C-terminal tail. Binding of EGF ligands to the extracellular domain induces an asymmetric dimer formation. (b) mNeonGreen-EGFR molecules densely cover COS7 cell membrane. (c) mNeonGren-EGFR molecules exhibit a continuous recovery of fluorescent intensity in a FRAP assay. (d) The fit of fluorescence recovery signal (red curve) reveals the average diffusion constant of EGFR spots. (e) In PhotoGate, diffusion of single mNeonGreenEGFR molecules was tracked in the ROI over 30 s. (f) On average ~47,000 photons were detected from single mNeonGreen molecules using PhotoGate (mean ± s.e.m.). (g) In the sptPALM experiment, individual mEos2-EGFR molecules were photoactivated with 405 nm excitation at t = 0 s, and fluorescent spots were tracked over 5 s. (h) The number of photons detected from single mEos2 spots before photobleaching (mean ± s.e.m.) was nine times lower than that of mNeonGreen.

The frequency of gating was adjusted depending on the diameter of the ROI, the width of the gate, and the density and diffusion constant of the fluorophores. The probability of particles escaping the gate was calculated based on the time dependent recovery profile in FRAP experiments[147] (see **Methods**) and was kept low (10^{-7}) to prevent crowding of fluorophores in ROI.
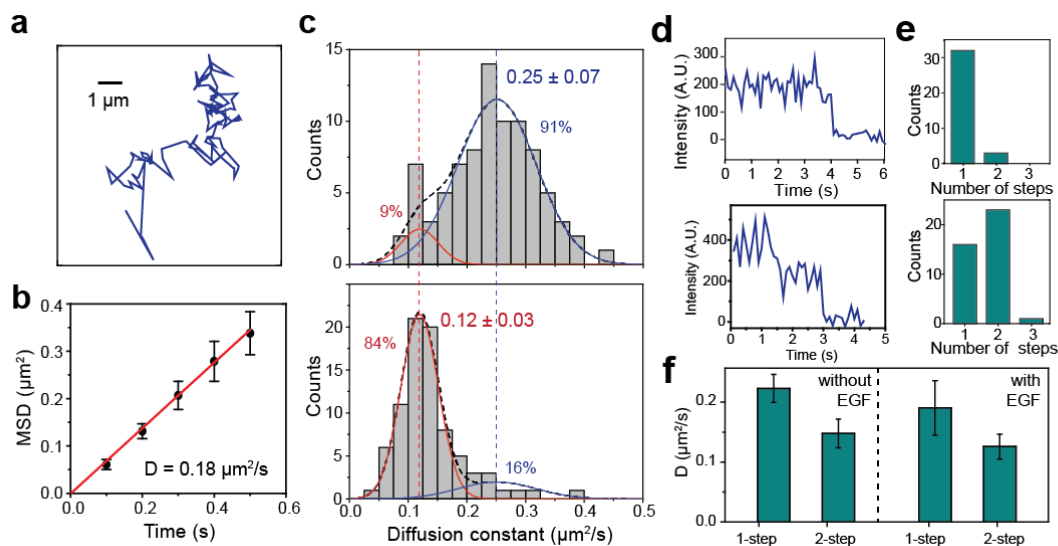

Figure 23. Ligand-induced dimerization of EGFR is determined by diffusion analysis and subunit counting. (a) Sample trajectory of an individual GFP-EGFR spots diffusing on a COS7 cell membrane. (b) MSD plot of an example trajectory. The slope of the linear fit (red line) represents the diffusion constant. (c) Diffusion constant histogram of EGFR spots in the absence (top) and the presence of 16 nM EGF. Multiple Gaussian fit (black dotted curve) reveals two major peaks. Without EGF, 91% of the spots are at the more diffusive state (D = 0.25 ± 0.07 µm²/s, blue curve) and 9% at the less diffusive state (D = 0.12 ± 0.03 µm²/s, red curve). EGF addition results in the 75% of the spots shifting from the more diffusive to the less diffusive state. (d) Example intensity profiles of EGFR spots showing one- (top) and two-step (bottom) photobleaching. (e) Photobleaching step histograms of GFP-EGFR spots in the absence (top) and presence (bottom) of EGF. (f) The average diffusion constant of EGFR spots that photobleached in one- and two-steps with and without EGF.

To compare the tracking ability of PhotoGate to sptPALM, we replaced mNeonGreen with mEos2, one of the brightest photoconvertible fluorescent proteins[135]. We expressed mEos2-EGFR in COS7 cells under the same conditions and tracked individual fluorescent spots using sptPALM at 20 frames per second **(Figure 22g)**[148]. On average, we detected ~5,000 photons from a single mEos2 spot before photobleaching (τ = 1.2 s,

Figure 22h). The results showed that SPT of mNeonGreen spots using PhotoGate provides more than ten-fold higher photon budget and hence better tracking ability than sptPALM of mEos2 spots.

The diffusion constants of individual spots were estimated by linearly fitting their mean-square-displacement (MSD) (**Figure 23a,b**). Spots that display confined diffusion or unidirectional motion were excluded from the analysis (~7%). In addition, 3-7% of EGFR complexes paused in the membrane for a few seconds, which may reflect transient interactions between EGFR and membrane domains[141], as well as cortical actin meshwork[149,150].

The histogram of the diffusion constants of freely-diffusing molecules revealed two distinct populations **(Figure 23c)**. In the absence of the EGF ligand in the serum, the majority (91%) of EGFR stay in a more diffusive state (D = 0.25 µm^2/s) and only 9% were found at a less diffusive state (D = 0.12 µm^2/s, N=85). We observed a large shift (84%, t-test, p-value <0.01, N > 80) in population towards the less diffusive state upon the addition of 16 nM EGF. The results show that the diffusion constant of EGFR molecules decreases nearly two-fold upon addition of EGF.

Photobleaching analysis of GFP-EGFR spots in COS7 cells revealed the stochiometry of EGFR complexes **(Figure 23d)**. In the absence of EGF, 91% of the fluorescent spots (N=35) displayed one-step photobleaching, indicating that they represent monomers of GFP-EGFR. In the presence of EGF, we observed that 57% of the spots (N = 40) bleach in two steps, suggesting that EGFR forms a dimer containing two GFPs per spot **(Figure 23e)**. The average intensities of spots that bleached in two steps were nearly double (2.1 fold higher without EGF and 1.8 fold higher with EGF) those of spots that bleached in a single step. In addition, spots that bleached in two steps diffused slower (D = 0.13 ± 0.04 µm^2/s, SD) compared to spots with only one fluorophore (D = 0.21 ± 0.07 µm^2/s) (t-test, p = 0.0036) **(Figure 23f),** in agreement with the two-state distribution of the diffusion constant histograms (**Figure 23c**). This result further indicates that the more diffusive particles are mostly monomers and the less diffusive particles are mostly dimers. We note that the percentage of molecules that show two-step bleaching (53%) is not as high as the percentage of molecules in the less diffusive state (84%) in 16 nM EGF. The single steps are partly due to premature bleaching as

fluorescent spots pass near the gate; reversible dimerization and membrane dissociation of EGFR[151], and limited time resolution to detect multiple steps. Given that ~20% of GFP molecules remain in a dark state due to misfolding or incomplete maturation[152], we estimated that the probability of observing a two-step bleaching event for a dimer is ~50% under these conditions, consistent with our observation.

Discussion

PhotoGate introduces a concept of a gate beam that allows precise control over the number of fluorescent particles entering ROI and enables tracking of single particles at high spatial and temporal resolution until they photobleach or dissociate from their stationary target. This technical ability opens new possibilities for tracking single molecules in living cells at arbitrarily high concentrations without photoactivation. Using this method, we directly monitored transient binding of rapidly diffusing molecules to a stationary organelle. We also monitored diffusion and ligand-induced oligomerization of single protein complexes on a cell membrane at surface densities two orders of magnitude higher than the diffraction limit. The results demonstrate that PhotoGate is widely applicable to single-molecule dynamics of receptor signaling, membrane protein dynamics, endocytosis and cytoskeleton-associated proteins at high resolution. The method is also extensible to deep-cell imaging by scanning a non-diverging Bessel beam[153] in a circular pattern to gate the boundary of a cylindrical ROI .

PhotoGate offers several unique advantages over existing methods that achieve single-molecule tracking in dense specimens. Using a FRAP-based approach, diffusion of single fluorescent clusters can be tracked on a cell membrane at the onset of the fluorescence recovery process[138]. This method enables multicolor tracking[154] and determines the diffusion constant[138] and brightness[155] of individual fluorophores. However, tracking time is limited by the surface density and diffusion constant of fluorescent particles in the unbleached region, and single particles typically cannot be resolved one second after photobleaching [138]. PhotoGate allows the tracking of individual particles in cellular processes that take longer than a few seconds, such as arrival to and dissociation of APPL1 from an endosome **(Figure 20)**. Unlike FRAP-based SPT methods, the

tracking time of PhotoGate is insensitive to the diffusion constant and surface density of fluorescent particles, and is limited solely by the photon budget of the fluorophore.

When diffusing proteins interact with a stationary structure and pause, such as in the case of APPL1 binding to endosomes, FRAP analysis is further complicated by the fact that multiple processes occurring at different rates (such as diffusion, binding and unbinding) contribute to the recovery signal. Fluorescence Correlation Spectroscopy has been used to specifically measure diffusion and filter out immobilized molecules[140]. PhotoGate is complementary to these methods, because it allows examination of bound molecules only, while the signal from the rapidly diffusing molecules is averaged out and thus excluded from analysis.

The major advantage of sptPALM over PhotoGate is the ability to obtain high density single-molecule trajectories in a single cell by simultaneously activating, imaging and bleaching molecules across the cell[148]. In comparison, PhotoGate provides unique advantages by bypassing the requirement of using photoconvertible probes. First, our method provides higher spatial and temporal resolution and longer tracking times **(Figure 22f,h)**, because the best-performing fluorescent proteins (such as eGFP and mNeon Green[156]) are superior to photoactivated fluorescent proteins in quantum yield, brightness and photostability[135]. We note that for applications demanding even higher brightness or photostability, PhotoGate can be used to image organic dyes such as Cy3 or TMR without further modifications. Second, sptPALM, which relies on stochastic photoactivation of a small subset of fluorophores, is not suitable for counting the total number of fluorophores in a diffusing spot. In comparison, all fluorophores observed via PhotoGate are in the bright state at the start of imaging, which allows the stoichiometry of individual spots to be determined by subunit counting (**Figure 23**) while further improving the SNR of the fluorescent spots for tracking applications. Third, PhotoGate is more suitable for multicolor applications, because it uses the same wavelength for imaging and gating. In comparison, the probes that change their excitation and emission wavelength upon photoinduction (such as Kaede and Eos) require a second excitation beam at a different wavelength[157], often causing crosstalk between the fluorescent channels. Furthermore, PhotoGate is applicable to existing cell lines that express conventional fluorescent probes and eliminates the requirement of

constructing new strains for single molecule imaging. In conclusion, PhotoGate is a superior method for long-term tracking, multicolor imaging and accurate detection of oligomerization states of single molecules in crowded environments.

Methods

Sample Preparation

DNA encoding the full-length human EGFR gene with a C-terminal eGFP[A206K] fusion in pEGFP-N1 (Clontech) mammalian expression vector was stably transfected into COS-7 cells. Briefly, COS-7 cells were transiently transfected using FuGENE (Roche) according to the manufacturer's instructions. Stable clones were isolated by selection in 800 μg/ml G418 for 4 weeks. Stable COS-7 cell lines were maintained in Dulbecco's Modified Eagle's Medium supplemented with 10% fetal bovine serum (FBS), streptomycin/penicillin and 200 μg/ml G418. 48 hours prior to use, cells were split into glass bottom petri dishes (Matek) with Phenol-red free DMEM. 12 hours before the experiment, cells were serum starved by replacing the medium with FBS-free medium. When noted, cells were treated with or without 16 nM EGF for 5 mins, before measurements were performed. The microscopy assays were performed at 37 °C.

U2OS cells were cultured following standard tissue culture protocols in McCoy's 5A media supplemented with 5% Fetal Bovine Serum (FBS). Twenty-four hours prior to imaging, 1.5 million U2OS cells were transfected via Nucleofector-T2 (Lonza) with 350 ng APPL1:GFP plasmid and split into two 35-mm glass-bottom poly-D-lysine-coated imaging dishes (MatTek). Lonza Kit R nucleofection solution and pulse X-001 were used to transfect cells. Prior to imaging, cells were incubated for 40 minutes in imaging buffer supplemented with 5 mM glucose, amino acids, and 5% dialyzed FBS, and containing 16.6 μM nocodazole to dampen endosomal trafficking via microtubules.

Microscope

An objective-type total internal reflection fluorescent (TIRF) microscope was set up, using a Nikon TiE inverted microscope equipped with a perfect focusing unit, bright-field illumination and a 100X 1.49 NA PlanApo oil immersion objective (Nikon). A 488

nm solid state laser (Coherent) was used for GFP excitation. The GFP signal was recorded by an Andor iXon 512 x 512 electron-multiplied charge-coupled device (EM-CCD) camera. 1.5x extra magnification was used to obtain a pixel size of 106 nm. Because the CCD image is saturated under intense laser illumination, shutter timing was synchronized with the camera acquisition by a DAQ card (NI, USB-6221). In a continuous acquisition mode of the camera, frames that were exposed to a high power PhotoGate beam was not used for data analysis. In a time-lapse data acquisition mode, the gate beam was turned on during the times when the camera was not acquiring data.

The PhotoGate Assay

A focused 488 nm laser beam (2 MW/cm^2) was steered with a fast piezo-driven mirror (S-330.8SL, Physik Instrumente). The piezo-driven mirror was mounted at a position conjugate to the back-focal plane of the objective to ensure that the tilting of the mirror results in pure translation of the focused beam in the image plane. The mirror has an angular travel range of approximately 10 mrad (with a slight difference between the two axes) and provides a usable range of 22 µm by 30 µm at the image plane of the microscope. The mirror's angle is updated at 200 Hz via two analog output channels of a USB-6221 DAQ card (National Instruments). The mirror was controlled by software custom-written in LabVIEW to define the dimension and the shape of the ROI. Typically, 50 outward spirals (each 0.2 s in duration) were used to pre-bleach the ROI, followed by a 2 s dark waiting period. The TIRF beam was then switched on and videos were recorded at rates between 0.67 and 20 Hz. The radius of the TIRF beam was dynamically adjusted using a variable-diameter iris at a point conjugate to the image plane in order to illuminate the ROI and prevent bleaching in the rest of the cell. Imaging was interspersed by 200 ms-long sweeps around the outer perimeter of the bleached area, repeated every 2 s. At acquisition rates slower than 5 frames per second, exposure was limited to 50 ms while the dark time between exposures was changed to result in the final desired frame rate.

sptPALM Assays

Cells were split into glass bottom petri dishes (Mattek) and transfected with mEos2-EGFR using Lipofectamine 2000. 24 hours post transfection the cells were serum

starved by replacing the medium with FBS-free medium for 12 hours. Photo-switching of mEos2-EGFR was accomplished using 1.6 W/cm^2 405 nm TIRF excitation beam for 200 ms. The activated molecules were imaged using 561 nm TIRF excitation beam at 100 ms per frame. The power of the excitation beam was adjusted to 160 W/cm^2 to collect photons counts per spot similar to that of PhotoGate assays.

Data Analysis

The probability of particles escaping the gate was calculated based on the time dependent recovery profile in FRAP experiments under the assumptions that all of the molecules undergo pure lateral diffusion with the same diffusion constant and that the gate beam is perfectly collimated and bleaches all of the particles located in the ring. The few molecules that were not bleached during prebleaching of the ROI were not included in data analysis.

The position of fluorescent spots was determined by fitting the PSFs to the 2D Gaussian function. The positions were fitted throughout the movie except at the frames when the photobleaching events happened or the frames in which the tracked particle overlapped with other fluorophores. The intensity of the spots is estimated by the volume of the 2D Gaussian peak. In a typical assay, we adjusted excitation power to achieve 20-nm localization accuracy at 10 Hz image acquisition rate. Under these conditions, individual mNeonGreen molecules were tracked for 5 s on average.

2D diffusion of EGFR spots were analyzed by mean-square displacement (MSD) analysis. MSD plots of diffusing particles were fitted to a polynomial function, $< x^2 > = 4Dt^a$, where D is the diffusion constant. The first ($\alpha = 1$) and second ($\alpha = 2$) order polynomial fits represent Brownian motion and unidirectional transport, respectively. $\alpha < 1$ was interpreted as sub-diffusion due to the confinement of molecules. 93% of the trajectories fit well ($R^2 > 0.95$) to a linear function with a positive y-intercept. Other trajectories were excluded from data analysis to filter out the non-diffusive particles in our dataset. Histograms are fitted by maximum likelihood estimator using original datasets. Pausing in EGFR diffusion is defined as the duration at which the standard deviation of the position is less than 50 nm within >1 s.

APPL1 residence times were analyzed by plotting the intensity vs. time profile for each fluorescent spot that appeared in the ROI while PhotoGate was on. Background intensity traces were collected for each fluorescent spot from a nearby dark region and subtracted from the APPL1 traces to correct for photobleaching of the sample under TIR illumination. Some endosomes were not perfectly immobilized, and any spots that moved by more than five pixels before bleaching were excluded from further analysis. Each remaining intensity profile was inspected, with fluorophore arrival and departure times assigned manually. Traces, in which the arrival and departure times could not be identified due to background fluctuations, were excluded from the analysis. The cumulative probability distribution of dwell times was then fit to a single exponential model, yielding the characteristic off-rate.

For FRAP analysis, a circular ROI (1.5 µm in diameter) was manually drawn over a recovering endosome and an identically sized ROI placed in a bleached area that did not contain any endosomes. Fluorescence intensity trajectories were then obtained for each of the two spots and fitted with a single exponential recovery model. Cells without a large enough endosome-free region throughout the timeline of recovery were excluded from further analysis.

CONCLUDING REMARKS

In the three projects described above, I investigated the unusual force production cycle of yeast dynein, measured the effect of cargo adaptor proteins on human dynein's force output, and contributed to the development of a novel single-molecule imaging technique. In the end, this work raises a number of new questions and opens up potential new research directions.

The dynein field has long suffered from a rift between labs studying recombinant yeast dynein and tissue-purified mammalian dynein. Early attempts at recombinant expression of human dynein[108] further complicated matters, as the recombinant dimer of heavy chains did not appear to be a functional motor protein altogether. Constant disagreements over biophysical properties of these motors led to a suspicion that divergent evolution abolished all but the most superficial similarities between the human and yeast isoforms. However, with the recent discovery of robust dynein activation by dynactin and cargo adaptor proteins[32,33], the rift may be starting to close. It now looks entirely plausible that rather than broadly diverging in structure and function, mammalian dynein merely acquired an autoinhibition mechanism that can be overridden at times and places where minus end-directed pulling along microtubules is required. My work demonstrated that activated human dynein is just as strong as the yeast isoform; it remains to be seen through careful experimentation whether the underlying mechanism of motility and force production also remain conserved across kingdoms.

Given dynein's many distinct roles within a eukaryotic cell, it is not surprising that its activity appears to be tightly regulated. The intracellular signaling responsible for attaching dynein to the correct cargos, activating its motility and force production on a cargo, and determining the overall direction and velocity of a cargo carried by multiple motors, is probably the most interesting emerging topic in dynein research. Tightly controlled *in vitro* motility assays coupling precise numbers of opposing motors, such as my dynein-kinesin competition experiment, will complement *in vivo* biological work and allow researchers to tease apart the individual contributions of motor protein regulators to the overall phenomenon of cargo transport.

Finally, the PhotoGate method will complement existing *in vivo* imaging techniques and allow researchers to make single-molecule observations under previously impractical conditions. The true power of the technique lies specifically in imaging *clusters* of fluorescent molecules. Single diffusing fluorophores can be detected and tracked using

existing methods; however, when multiple molecules dynamically and disassemble into larger macromolecular structures, the indistinguishability of individual fluorophores precludes one from making accurate measurements of the cluster's dynamics. With PhotoGate, arrival and departure events of single fluorophores into a larger macromolecular assembly suddenly become detectable. While an enormous number of biological processes fall under this broad category, I would like to conclude by proposing that the dynamic recruitment of cytoskeletal motor proteins and their regulators onto cellular cargoes could be exceptionally amenable to study with the PhotoGate technique.

REFERENCES

1. Rock, R. S., Rief, M., Mehta, A. D. & Spudich, J. A. In vitro assays of processive myosin motors. *Methods* **22,** 373–81 (2000).

2. Howard, J., Hudspeth, A.J., Vale, R. D. Movement of microtubules by single kinesin molecules. *Nature* **342,** 154–158 (1989).

3. Sakamoto, T., Amitani, I., Yokota, E. & Ando, T. Direct observation of processive movement by individual myosin V molecules. *Biochem. Biophys. Res. Commun.* **272,** 586–90 (2000).

4. Rock, R. S. *et al.* Myosin VI is a processive motor with a large step size. *Proc. Natl. Acad. Sci. U. S. A.* **98,** 13655–9 (2001).

5. Ali, M. Y. *et al.* Myosin V is a left-handed spiral motor on the right-handed actin helix. *Nat. Struct. Biol.* **9,** 464–7 (2002).

6. Yildiz, A. *et al.* Myosin V walks hand-over-hand: single fluorophore imaging with 1.5-nm localization. *Science* **300,** 2061–5 (2003).

7. Yildiz, A., Tomishige, M., Vale, R. D. & Selvin, P. R. Kinesin walks hand-over-hand. *Science* **303,** 676–8 (2004).

8. Yildiz, A. *et al.* Myosin VI steps via a hand-over-hand mechanism with its lever arm undergoing fluctuations when attached to actin. *J. Biol. Chem.* **279,** 37223–6 (2004).

9. Okten, Z., Churchman, L. S., Rock, R. S. & Spudich, J. A. Myosin VI walks hand-over-hand along actin. *Nat. Struct. Mol. Biol.* **11,** 884–7 (2004).

10. Nishikawa, S. *et al.* Switch between Large Hand-Over-Hand and Small Inchworm-like Steps in Myosin VI. *Cell* **142,** 879–88 (2010).

11. Alonso, M. C. *et al.* An ATP gate controls tubulin binding by the tethered head of kinesin-1. *Science* **316,** 120–3 (2007).

12. Block, S. M. Kinesin motor mechanics: binding, stepping, tracking, gating, and limping. *Biophys. J.* **92,** 2986–95 (2007).

13. Yildiz, A., Tomishige, M., Gennerich, A. & Vale, R. D. Supplemental Data Intramolecular Strain Coordinates Kinesin Stepping Behavior along Microtubules. *Cell* **134,** 1030–41 (2008).

14. Guydosh, N. R. & Block, S. M. Direct observation of the binding state of the kinesin head to the microtubule. *Nature* **461,** 125–8 (2009).

15. Andreasson, J. O. L. *et al.* Examining kinesin processivity within a general gating framework. *Elife* **2015,** 1–44 (2015).

16. Dogan, M. Y., Can, S., Cleary, F. B., Purde, V. & Yildiz, A. Kinesin's front head is gated by the backward orientation of its Neck Linker. *Cell Rep.* **10,** 1968–1974 (2015).

17. Reck-Peterson, S. L. *et al.* Single-molecule analysis of dynein processivity and stepping behavior. *Cell* **126,** 335–48 (2006).

18. Churchman, L. S., Okten, Z., Rock, R. S., Dawson, J. F. & Spudich, J. A. Single molecule high-resolution colocalization of Cy3 and Cy5 attached to macromolecules measures intramolecular distances through time. *Proc. Natl. Acad. Sci. U. S. A.* **102,** 1419–23 (2005).

19. DeWitt, M. A., Chang, A. Y., Combs, P. A. & Yildiz, A. Cytoplasmic dynein moves through uncoordinated stepping of the AAA+ ring domains. *Science* **335,** 221–5 (2012).

20. Pertsinidis, A., Zhang, Y. & Chu, S. Subnanometre single-molecule localization, registration and distance measurements. *Nature* **466,** 647–651 (2010).

21. Qiu, W. *et al.* Dynein achieves processive motion using both stochastic and coordinated stepping. *Nat. Struct. Mol. Biol.* **19,** 193–200 (2012).

22. Barlan, K., Rossow, M. J. & Gelfand, V. I. The journey of the organelle: teamwork and regulation in intracellular transport. *Curr. Opin. Cell Biol.* **25,** 483–8 (2013).

23. Friedman, D. S. & Vale, R. D. Single-molecule analysis of kinesin motility reveals regulation by the cargo-binding tail domain. *Nat. Cell Biol.* **1,** 293–7 (1999).

24. Kaan, H. Y. K., Hackney, D. D. & Kozielski, F. The structure of the kinesin-1 motor-tail complex reveals the mechanism of autoinhibition. *Science* **333,** 883–5 (2011).

25. Hammond, J. W., Blasius, T. L., Soppina, V., Cai, D. & Verhey, K. J. Autoinhibition of the kinesin-2 motor KIF17 via dual intramolecular mechanisms. *J. Cell Biol.* **189,** 1013–25 (2010).

26.   Hammond, J. W. *et al.* Mammalian Kinesin-3 motors are dimeric in vivo and move by processive motility upon release of autoinhibition. *PLoS Biol.* **7,** e72 (2009).

27.   Krementsov, D. N., Krementsova, E. B. & Trybus, K. M. Myosin V: regulation by calcium, calmodulin, and the tail domain. *J. Cell Biol.* **164,** 877–86 (2004).

28.   Wang, F. *et al.* Regulated conformation of myosin V. *J. Biol. Chem.* **279,** 2333–6 (2004).

29.   Li, X., Mabuchi, K., Ikebe, R. & Ikebe, M. Ca2+-induced activation of ATPase activity of myosin Va is accompanied with a large conformational change. *Biochem. Biophys. Res. Commun.* **315,** 538–45 (2004).

30.   Huang, J., Roberts, A. J., Leschziner, A. E. & Reck-Peterson, S. L. Lis1 Acts as a 'Clutch' between the ATPase and Microtubule-Binding Domains of the Dynein Motor. *Cell* **150,** 975–86 (2012).

31.   Markus, S. M., Kalutkiewicz, K. a & Lee, W.-L. She1-mediated inhibition of dynein motility along astral microtubules promotes polarized spindle movements. *Curr. Biol.* **22,** 2221–30 (2012).

32.   McKenney, R. J., Huynh, W., Tanenbaum, M. E., Bhabha, G. & Vale, R. D. Activation of cytoplasmic dynein motility by dynactin-cargo adapter complexes. *Science* **345,** 337–341 (2014).

33.   Schlager, M. A., Hoang, H. T., Urnavicius, L., Bullock, S. L. & Carter, A. P. In vitro reconstitution of a highly processive recombinant human dynein complex. *EMBO J.* 1–14 (2014). doi:10.15252/embj.201488792

34.   Kapitein, L. C., Peterman, E. J. G. & Kwok, B. H. The bipolar mitotic kinesin Eg5 moves on both microtubules that it crosslinks. *Nature* **435,** 114–8 (2005).

35.   Kwok, B. H. *et al.* Allosteric inhibition of kinesin-5 modulates its processive directional motility. *Nat. Chem. Biol.* **2,** 480–5 (2006).

36.   Firestone, A. J. *et al.* Small-molecule inhibitors of the AAA+ ATPase motor cytoplasmic dynein. *Nature* **484,** 125–9 (2012).

37.   Bergnes, G., Brejc, K. & Belmont, L. Mitotic Kinesins: Prospects for Antimitotic Drug Discovery. *Curr. Top. Med. Chem.* **5,** 127–45 (2005).

38.   Ligon, L. A. & Steward, O. Movement of mitochondria in the axons and dendrites

of cultured hippocampal neurons. *J. Comp. Neurol.* **427,** 340–50 (2000).

39. Blocker, A. *et al.* Molecular requirements for bi-directional movement of phagosomes along microtubules. *J. Cell Biol.* **137,** 113–29 (1997).

40. Soppina, V., Rai, A. K., Ramaiya, A. J., Barak, P. & Mallik, R. Tug-of-war between dissimilar teams of microtubule motors regulates transport and fission of endosomes. *Proc. Natl. Acad. Sci. U. S. A.* **106,** 19381–6 (2009).

41. Kunwar, A. *et al.* Mechanical stochastic tug-of-war models cannot explain bidirectional lipid-droplet transport. *PNAS* **108,** 18960–18965 (2011).

42. Uchida, A., Alami, N. H. & Brown, A. Tight Functional Coupling of Kinesin-1A and Dynein Motors in the Bidirectional Transport of Neurofilaments. *Mol. Biol. Cell* **20,** 4997–5006 (2009).

43. Engel, B. D. *et al. Total internal reflection fluorescence (TIRF) microscopy of Chlamydomonas flagella. Methods Cell Biol.* **93,** (Elsevier, 2009).

44. Gross, S. P., Vershinin, M. & Shubeita, G. T. Cargo transport: two motors are sometimes better than one. *Curr. Biol.* **17,** R478–86 (2007).

45. Hendricks, A. G. *et al.* Motor coordination via a tug-of-war mechanism drives bidirectional vesicle transport. *Curr. Biol.* **20,** 697–702 (2010).

46. Shubeita, G. T. *et al.* Consequences of motor copy number on the intracellular transport of kinesin-1-driven lipid droplets. *Cell* **135,** 1098–107 (2008).

47. Gross, S. P. Hither and yon: a review of bi-directional microtubule-based transport. *Phys. Biol.* **1,** R1–11 (2004).

48. Sims, P. A. & Xie, X. S. Probing dynein and kinesin stepping with mechanical manipulation in a living cell. *Chemphyschem* **10,** 1511–6 (2009).

49. Shih, S. M. *et al.* Intraflagellar transport drives flagellar surface motility. *Elife* **2,** e00744 (2013).

50. Derr, N. D. *et al.* Tug-of-War in Motor Protein Ensembles Revealed with a Programmable DNA Origami Scaffold. *Science* **338,** 662–665 (2012).

51. Vale, Ronald D., Funatsu, Takashi, Pierce, Daniel W., Romberg, Laura, Harada, Yoshie, Yanagida, T. Direct observation of single kinesin molecules moving along microtubules. *Nature* **380,** 451–453 (1996).

52. Axelrod, D., Thompson, N. L. & Burghardt, T. P. Total internal reflection fluorescent microscopy. *J. Microsc.* **129,** 19–28 (1983).

53. Svoboda, Karel, Schmidt, Christoph F. , Schnapp, Bruce J. , Block, S. M. Direct observation of kinesin stepping by optical trapping interferometry. *Nature* **365,** 721–727 (1993).

54. Tomishige, M., Klopfenstein, D. R. & Vale, R. D. Conversion of Unc104/KIF1A kinesin into a processive motor after dimerization. *Science* **297,** 2263–7 (2002).

55. Park, H. *et al.* Full-length myosin VI dimerizes and moves processively along actin filaments upon monomer clustering. *Mol. Cell* **21,** 331–6 (2006).

56. Kuo, S. C., Gelles, J., Steuer, E. & Sheetz, M. P. A model for kinesin movement from nanometer-level movements of kinesin and cytoplasmic dynein and force measurements. *J. Cell Sci. Suppl.* **14,** 135–8 (1991).

57. Hua, W., Chung, J. & Gelles, J. Distinguishing inchworm and hand-over-hand processive kinesin movement by neck rotation measurements. *Science* **295,** 844–8 (2002).

58. Bobroff, N. Position measurement with a resolution and noise-limited instrument. *Rev. Sci. Instrum.* **57,** 1152 (1986).

59. Thompson, R. Precise Nanometer Localization Analysis for Individual Fluorescent Probes. *Biophys. J.* **82,** 2775–2783 (2002).

60. Levitus, M. & Ranjit, S. Cyanine dyes in biophysical research: the photophysics of polymethine fluorescent dyes in biomolecular environments. *Q. Rev. Biophys.* **44,** 123–51 (2011).

61. Rasnik, I., Mckinney, S. A. & Ha, T. Nonblinking and long- lasting single-molecule fluorescence imaging. *Nat. Methods* **3,** 891–893 (2006).

62. Englander SW, Calhoun DB, E. J. Biochemistry without oxygen. *Anal Biochem.* **161,** 300–6 (1987).

63. Aitken, C. E., Marshall, R. A. & Puglisi, J. D. An oxygen scavenging system for improvement of dye stability in single-molecule fluorescence experiments. *Biophys. J.* **94,** 1826–35 (2008).

64. Chudakov, D. M., Matz, M. V, Lukyanov, S. & Lukyanov, K. A. Fluorescent Proteins and Their Applications in Imaging Living Cells and Tissues. *Physiol Rev*

90, 1103–1163 (2010).

65. Warshaw, D. M. *et al.* Differential labeling of myosin V heads with quantum dots allows direct visualization of hand-over-hand processivity. *Biophys. J.* **88,** L30–2 (2005).

66. Perkins, T. T. Ångström-Precision Optical Traps and Applications. *Annu. Rev. Biophys.* **43,** 279–302 (2014).

67. Neuman, K. C. & Block, S. M. Optical trapping. *Rev. Sci. Instrum.* **75,** 2787–809 (2004).

68. Bustamante, C., Chemla, Y. R. & Moffitt, J. R. High-resolution dual-trap optical tweezers with differential detection: alignment of instrument components. *Cold Spring Harb. Protoc.* **2009,** pdb.ip76 (2009).

69. Moffitt, J. R. Viral DNA packaging at base pair resolution. (2009).

70. Gittes, F. & Schmidt, C. F. Thermal noise limitations on micromechanical experiments. *Eur. Biophys. J.* **27,** 75–81 (1998).

71. Gittes, F. & Schmidt, C. F. Signals and noise in micromechanical measurements. *Methods Cell Biol.* **55,** 129–56 (1998).

72. Carter, A. R. *et al.* Stabilization of an optical microscope to 0.1 nm in three dimensions. *Appl. Opt.* **46,** 421–7 (2007).

73. Brouhard, G. J. G. J., Schek, H. T. H. T. H. T. & Hunt, A. J. a. J. A. J. Advanced optical tweezers for the study of cellular and molecular biomechanics. *IEEE Trans. Biomed. Eng.* **50,** 121–125 (2003).

74. Mallik, R., Carter, B. C., Lex, S. A., King, S. J. & Gross, S. P. Cytoplasmic dynein functions as a gear in response to load. *Nature* **427,** 649–52 (2004).

75. Gennerich, A., Carter, A. P., Reck-Peterson, S. L. & Vale, R. D. Force-induced bidirectional stepping of cytoplasmic dynein. *Cell* **131,** 952–65 (2007).

76. Roberts, A. J., Kon, T., Knight, P. J., Sutoh, K. & Burgess, S. A. Functions and mechanics of dynein motor proteins. *Nat. Rev. Mol. Cell Biol.* **14,** 713–26 (2013).

77. Kardon, J. R. & Vale, R. D. Regulators of the cytoplasmic dynein motor. *Nat. Rev. Mol. Cell Biol.* **10,** 854–65 (2009).

78. Carter, A. P., Cho, C., Jin, L. & Vale, R. D. Crystal Structure of the Dynein

Motor Domain. *Science* **331,** 1159–1165 (2011).

79. Kon, T., Sutoh, K. & Kurisu, G. X-ray structure of a functional full-length dynein motor domain. *Nat. Struct. Mol. Biol.* **18,** 638–642 (2011).

80. Höök, P. & Vallee, R. B. The dynein family at a glance. *J. Cell Sci.* **119,** 4369–71 (2006).

81. Imamula, K., Kon, T., Ohkura, R. & Sutoh, K. The coordination of cyclic microtubule association/dissociation and tail swing of cytoplasmic dynein. *Proc. Natl. Acad. Sci. U. S. A.* **104,** 16134–9 (2007).

82. Roberts, A. J. *et al.* AAA+ Ring and linker swing mechanism in the dynein motor. *Cell* **136,** 485–95 (2009).

83. Kon, T. *et al.* The 2.8 Å crystal structure *Nature* **484,** 345–50 (2012).

84. Schmidt, H., Gleave, E. S. & Carter, A. P. Insights into dynein motor domain function from a 3.3-Å crystal structure. *Nat. Struct. Mol. Biol.* **19,** 492–7 (2012).

85. Kon, T., Mogami, T., Ohkura, R., Nishiura, M. & Sutoh, K. ATP hydrolysis cycle-dependent tail motions in cytoplasmic dynein. *Nat. Struct. Mol. Biol.* **12,** 513–9 (2005).

86. Roberts, A. J. *et al.* ATP-Driven Remodeling of the Linker Domain in the Dynein Motor. *Structure* **20,** 1670–1680 (2012).

87. Lu, Y., Weers, B. & Stellwagen, N. C. DNA persistence length revisited. *Biopolymers* **61,** 261–75 (2002).

88. Coy, D., Wagenbach, M. & Howard, J. Kinesin takes one 8-nm step for each ATP that it hydrolyzes. *J. Biol. Chem.* **274,** 3667–3671 (1999).

89. Kon, T., Nishiura, M., Ohkura, R., Toyoshima, Y. Y. & Sutoh, K. Distinct functions of nucleotide-binding/hydrolysis sites in the four AAA modules of cytoplasmic dynein. *Biochemistry* **43,** 11266–74 (2004).

90. Cleary, F. B. *et al.* Tension on the linker gates the ATP-dependent release of dynein from microtubules. *Nat. Commun.* **5,** 4587 (2014).

91. Cho, C., Reck-Peterson, S. L. & Vale, R. D. Regulatory ATPase sites of cytoplasmic dynein affect processivity and force generation. *J. Biol. Chem.* **283,**

25839–45 (2008).

92. Visscher, K., Schnitzer, M. J. & Block, S. M. Single kinesin molecules studied with a molecular force clamp. *Nature* **400,** 184–9 (1999).

93. Gibbons, I. R. *et al.* The affinity of the dynein microtubule-binding domain is modulated by the conformation of its coiled-coil stalk. *J. Biol. Chem.* **280,** 23960–5 (2005).

94. Thomas, N., Imafuku, Y. & Tawada, K. Molecular motors: thermodynamics and the random walk. *Proc. R. Soc. B* **268,** 2113–22 (2001).

95. Burgess, S. A., Walker, M. L., Sakakibara, H., Knight, P. J. & Oiwa, K. Dynein structure and power stroke. *Nature* **421,** 715–8 (2003).

96. Hendricks, A. G., Holzbaur, E. L. F. & Goldman, Y. E. Force measurements on cargoes in living cells reveal collective dynamics of microtubule motors. *Proc. Natl. Acad. Sci. U. S. A.* **2012,** 1–6 (2012).

97. Rai, A. K. A., Rai, A. K. A., Ramaiya, A. J., Jha, R. & Mallik, R. Molecular adaptations allow dynein to generate large collective forces inside cells. *Cell* **152,** 172–82 (2013).

98. Kunwar, A. & Mogilner, A. Robust transport by multiple motors with nonlinear force-velocity relations and stochastic load sharing. *Phys. Biol.* **7,** 16012 (2010).

99. Tanenbaum, M. E., Vale, R. D. & McKenney, R. J. Cytoplasmic dynein crosslinks and slides anti-parallel microtubules using its two motor domains. *Elife* **2,** e00943 (2013).

100. Hirakawa, E., Higuchi, H. & Toyoshima, Y. Y. Processive movement of single 22S dynein molecules occurs only at low ATP concentrations. *Proc. Natl. Acad. Sci. U. S. A.* **97,** 2533–7 (2000).

101. Svoboda, K. & Block, S. M. Force and velocity measured for single kinesin molecules. *Cell* **77,** 773–84 (1994).

102. Kalafut, B. & Visscher, K. An objective, model-independent method for detection of non-uniform steps in noisy signals. *Comput. Phys. Commun.* **179,** 716–723 (2008).

103. Ori-McKenney, K. M., Xu, J., Gross, S. P. & Vallee, R. B. A cytoplasmic dynein tail mutation impairs motor processivity. *Nat. Cell Biol.* **12,** 1228–1234 (2010).

104. Moughamian, A. J., Osborn, G. E., Lazarus, J. E., Maday, S. & Holzbaur, E. L. F. Ordered recruitment of dynactin to the microtubule plus-end is required for efficient initiation of retrograde axonal transport. *J. Neurosci.* **33,** 13190–203 (2013).

105. van Spronsen, M. *et al.* TRAK/Milton Motor-Adaptor Proteins Steer Mitochondrial Trafficking to Axons and Dendrites. *Neuron* **77,** 485–502 (2013).

106. Torisawa, T. *et al.* Autoinhibition and cooperative activation mechanisms of cytoplasmic dynein. *Nat. Cell Biol.* **16,** 1118–1124 (2014).

107. Wang, Z. & Sheetz, M. P. One-dimensional diffusion on microtubules of particles coated with cytoplasmic dynein and immunoglobulins. *Cell Struct. Funct.* **24,** 373–383 (1999).

108. Trokter, M., Mücke, N. & Surrey, T. Reconstitution of the human cytoplasmic dynein complex. *Proc. Natl. Acad. Sci. U. S. A.* **109,** 20895–900 (2012).

109. Ayloo, S. *et al.* Dynactin functions as both a dynamic tether and brake during dynein-driven motility. *Nat. Commun.* **5,** 4807 (2014).

110. McKenney, R. J., Vershinin, M., Kunwar, A., Vallee, R. B. & Gross, S. P. LIS1 and NudE induce a persistent dynein force-producing state. *Cell* **141,** 304–314 (2010).

111. Tripathy, S. K. *et al.* Autoregulatory mechanism for dynactin control of processive and diffusive dynein transport. *Nat. Cell Biol.* **16,** 1192–1201 (2014).

112. Rai, A. *et al.* Dynein Clusters into Lipid Microdomains on Phagosomes to Drive Rapid Transport toward Lysosomes. *Cell* 722–734 (2016). doi:10.1016/j.cell.2015.12.054

113. Hancock, W. O. Bidirectional cargo transport: moving beyond tug of war. *Nat. Rev. Mol. Cell Biol.* **15,** 615–628 (2014).

114. Urnavicius, L. *et al.* The structure of the dynactin complex and its interaction with dynein. *Science* (2015). doi:10.1126/science.aaa4080

115. Splinter, D. *et al.* BICD2, dynactin, and LIS1 cooperate in regulating dynein recruitment to cellular structures. *Mol. Biol. Cell* **23,** 4226–4241 (2012).

116. Thirumurugan, K., Sakamoto, T., Hammer, J. A., Sellers, J. R. & Knight, P. J. The cargo-binding domain regulates structure and activity of myosin 5. *Nature*

442, 212–5 (2006).

117. King, S. J. & Schroer, T. Dynactin increases the processivity of the cytoplasmic dynein motor. *Nat. Cell Biol.* **2,** 20–4 (2000).

118. Chowdhury, S., Ketcham, S. a, Schroer, T. a & Lander, G. C. Structural organization of the dynein–dynactin complex bound to microtubules. *Nat. Struct. Mol. Biol.* **advance on,** 1–6 (2015).

119. Nicholas, M. P. *et al.* Control of cytoplasmic dynein force production and processivity by its C-terminal domain. *Nat. Commun.* **6,** 6206 (2015).

120. Belyy, V., Hendel, N. L., Chien, A. & Yildiz, A. Cytoplasmic dynein transports cargos via load-sharing between the heads. *Nat. Commun.* **5,** 5544 (2014).

121. Diehl, M. R., Zhang, K., Lee, H. J. & Tirrell, D. A. Engineering Cooperativity in Biomotor-Protein Assemblies. *Science* **311,** 1468–1471 (2006).

122. Fu, M. M. & Holzbaur, E. L. F. JIP1 regulates the directionality of APP axonal transport by coordinating kinesin and dynein motors. *J. Cell Biol.* **202,** 495–508 (2013).

123. Leidel, C., Longoria, R. a., Gutierrez, F. M. & Shubeita, G. T. Measuring molecular motor forces in vivo: Implications for tug-of-war models of bidirectional transport. *Biophys. J.* **103,** 492–500 (2012).

124. Fu, M. & Holzbaur, E. L. F. Integrated regulation of motor-driven organelle transport by scaffolding proteins. *Trends Cell Biol.* **24,** 564–574 (2014).

125. Klumpp, S. & Lipowsky, R. Cooperative Cargo Transport by Several Molecular Motors. *PNAS* **102,** (2005).

126. Vijayachandran, L. S. *et al.* Robots, pipelines, polyproteins: Enabling multiprotein expression in prokaryotic and eukaryotic cells. *J. Struct. Biol.* **175,** 198–208 (2011).

127. Gibbons, I. R. & Fronk, E. Latent adenosine-triphosphatase form of dynein-1 from sea urchin sperm flagella . *J. Biol. Chem.* **254 ,** 187–196 (1979).

128. Castoldi, M. & Popov, A. V. Purification of brain tubulin through two cycles of polymerization- depolymerization in a high-molarity buffer. *Protein Expr. Purif.* **32,** 83–88 (2003).

129. Rust, M. J., Bates, M. & Zhuang, X. Sub-diffraction-limit imaging by stochastic optical reconstruction microscopy (STORM). *Nat Methods* **3,** 793–795 (2006).

130. Betzig, E. *et al.* Imaging intracellular fluorescent proteins at nanometer resolution. *Science* **313,** 1642–1645 (2006).

131. Kner, P., Chhun, B. B., Griffis, E. R., Winoto, L. & Gustafsson, M. G. Super-resolution video microscopy of live cells by structured illumination. *Nat Methods* **6,** 339–342 (2009).

132. Klar, T. A., Jakobs, S., Dyba, M., Egner, A. & Hell, S. W. Fluorescence microscopy with diffraction resolution barrier broken by stimulated emission. *Proc Natl Acad Sci U S A* **97,** 8206–8210 (2000).

133. Kuzmenko, A. *et al.* Single molecule tracking fluorescence microscopy in mitochondria reveals highly dynamic but confined movement of Tom40. *Sci Rep* **1,** 195 (2011).

134. Persson, F., Linden, M., Unoson, C. & Elf, J. Extracting intracellular diffusive states and transition rates from single-molecule tracking data. *Nat Methods* **10,** 265–269 (2013).

135. McKinney, S. A., Murphy, C. S., Hazelwood, K. L., Davidson, M. W. & Looger, L. L. A bright and photostable photoconvertible fluorescent protein. *Nat Methods* **6,** 131–133 (2009).

136. English, B. P. *et al.* Ever-fluctuating single enzyme molecules: Michaelis-Menten equation revisited. *Nat. Chem. Biol.* **2,** 87–94 (2006).

137. Reits, E. A. & Neefjes, J. J. From fixed to FRAP: measuring protein mobility and activity in living cells. *Nat Cell Biol* **3,** E145–7 (2001).

138. Moertelmaier, M., Brameshuber, M., Linimeier, M., Schütz, G. J. & Stockinger, H. Thinning out clusters while conserving stoichiometry of labeling. *Appl. Phys. Lett.* **87,** 1–3 (2005).

139. Zoncu, R. *et al.* A Phosphoinositide Switch Controls the Maturation and Signaling Properties of APPL Endosomes. *Cell* **136,** 1110–1121 (2009).

140. Wachsmuth, M. Molecular diffusion and binding analyzed with FRAP. *Protoplasma* **251,** 373–382 (2014).

141. Low-Nam, S. T. *et al.* ErbB1 dimerization is promoted by domain co-confinement

and stabilized by ligand binding. *Nat Struct Mol Biol* **18,** 1244–1249 (2011).

142. Zhang, X., Gureasko, J., Shen, K., Cole, P. A. & Kuriyan, J. An allosteric mechanism for activation of the kinase domain of epidermal growth factor receptor. *Cell* **125,** 1137–1149 (2006).

143. Sako, Y., Minoghchi, S. & Yanagida, T. Single-molecule imaging of EGFR signalling on the surface of living cells. *Nat. Cell Biol.* **2,** 168–172 (2000).

144. Lidke, D. S., Lidke, K. A., Rieger, B., Jovin, T. M. & Arndt-Jovin, D. J. Reaching out for signals: filopodia sense EGF and respond by directed retrograde transport of activated receptors. *J Cell Biol* **170,** 619–626 (2005).

145. Chung, I. *et al.* Spatial control of EGF receptor activation by reversible dimerization on living cells. *Nature* **464,** 783–787 (2010).

146. Kubitscheck, U., Kuckmann, O., Kues, T. & Peters, R. Imaging and tracking of single GFP molecules in solution. *Biophys J* **78,** 2170–9. (2000).

147. Axelrod, D., Koppel, D. E., Schlessinger, J., Elson, E. & Webb, W. W. Mobility measurement by analysis of fluorescence photobleaching recovery kinetics. *Biophys. J.* **16,** 1055–1069 (1976).

148. Manley, S. *et al.* High-density mapping of single-molecule trajectories with photoactivated localization microscopy. *Nat Methods* **5,** 155–157 (2008).

149. den Hartigh, J. C., van Bergen en Henegouwen, P. M., Verkleij, A. J. & Boonstra, J. The EGF receptor is an actin-binding protein. *J Cell Biol* **119,** 349–355 (1992).

150. Morone, N. *et al.* Three-dimensional reconstruction of the membrane skeleton at the plasma membrane interface by electron tomography. *J Cell Biol* **174,** 851–862 (2006).

151. Haglund, K. & Dikic, I. The role of ubiquitylation in receptor endocytosis and endosomal sorting. *J. Cell Sci.* **125,** 265–275 (2012).

152. Ulbrich, M. H. & Isacoff, E. Y. Subunit counting in membrane-bound proteins. *Nat. Methods* **4,** 319–21 (2007).

153. Chen, B.-C. *et al.* Lattice light-sheet microscopy: Imaging molecules to embryos at high spatiotemporal resolution. *Science* **346,** (2014).

154. Ruprecht, V., Brameshuber, M. & Schütz, G. J. Two-color single molecule

tracking combined with photobleaching for the detection of rare molecular interactions in fluid biomembranes. *Soft Matter* **6,** 568 (2010).

155. Madl, J. *et al.* Resting state Orai1 diffuses as homotetramer in the plasma membrane of live mammalian cells. *J. Biol. Chem.* **285,** 41135–41142 (2010).

156. Shaner, N. C. *et al.* A bright monomeric green fluorescent protein derived from Branchiostoma lanceolatum. *Nat Methods* **10,** 407–409 (2013).

157. Fernandez-Suarez, M. & Ting, A. Y. Fluorescent probes for super-resolution imaging in living cells. *Nat Rev Mol Cell Biol* **9,** 929–943 (2008).

APPENDIX

Force-velocity relation of a one-state motor

Here, I present the derivation of the force-velocity (F-V) relation for a one-state motor model allowing for force dependence in both the forward and backward stepping rates.

We start with the basic equation relating the forward and backward stepping rates of a one-state motor[94]:

$$\frac{k_+(f)}{k_-(f)} = e^{-(\Delta G + Lf)/kT}, \quad (1)$$

where f is the external load on the motor, $k_+(f)$ is the force-dependent forward stepping rate, $k_-(f)$ is the force-dependent backward stepping rate, ΔG is the free energy from ATP hydrolysis biasing the motor to step forward, L is the step size, k is the Boltzmann constant, and T is the temperature.

We now assign variable force dependence to $k_+(f)$ and $k_-(f)$, introducing the dimensionless parameters a and b:

$$k_+(f) = k_+ e^{-aLf/kT} \quad (2)$$

$$k_-(f) = k_- e^{bLf/kT} \quad (3)$$

Where k_+ and k_- are the constant forward and backward stepping rates in unloaded conditions.

Substituting equations (2) and (3) into (1), we obtain

$$\frac{k_+}{k_-} e^{-(a+b)Lf/kT} = e^{-(\Delta G + Lf)/kT}. \quad (4)$$

Because both the exponents and preexponents must be equal for all f for the equality above to hold, it follows that

$$\frac{k_+}{k_-} = e^{-\Delta G/kT} \quad (5) \quad \text{and}$$

$$a + b = 1. \quad (6)$$

Now, to obtain an expression for the velocity of the motor as a function of force, we note that the velocity is just the difference between the forward and backward stepping rates multiplied by the step size:

$$V(f) = L(k_+(f) - k_-(f)). \quad (7)$$

Substituting (2), (3), (5), and (6) and rearranging, we get the following expression for the F-V relation:

$$V(f) = Lk_+e^{-aLf/kT}(1 - e^{(\Delta G+Lf)/kT}). \quad (8)$$